Erasmus+

CoMEM

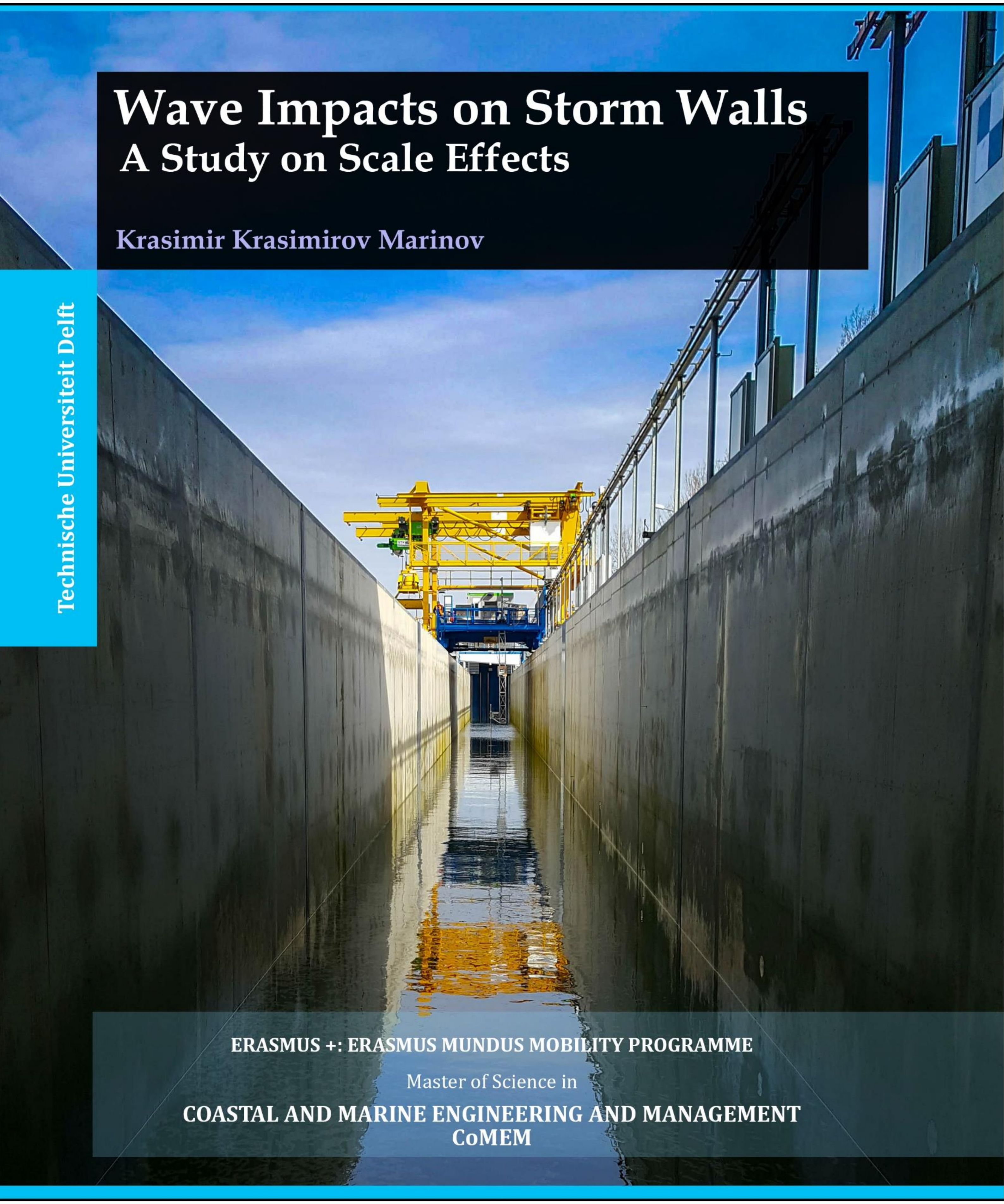

Wave Impacts on Storm Walls
A Study on Scale Effects

Krasimir Krasimirov Marinov

Technische Universiteit Delft

ERASMUS +: ERASMUS MUNDUS MOBILITY PROGRAMME

Master of Science in

COASTAL AND MARINE ENGINEERING AND MANAGEMENT
CoMEM

NTNU Norwegian University of Science and Technology

TU Delft Delft University of Technology

University of Southampton

Universitat Politècnica de Catalunya BarcelonaTech

City University of London EST 1894

Wave Impacts on Storm Walls
A Study on Scale Effects

As a requirement to attend the degree of

Erasmus+: Erasmus Mundus Master in Coastal and Marine Engineering and Management (CoMEM)

taught at the following educational institutions:

Norges Teknisk- Naturvitenskapelige Universitet (NTNU)
Trondheim, Norway

Technische Universiteit (TU) Delft
Delft, The Netherlands

University of Southampton,
Southampton, Great Britain

At which the student has studied from August 2015 to July 2017.

Krasimir Krasimirov Marinov
Student number: 4535715
11 July 2017

Thesis committee:	Prof. dr. ir. W.S.J. Uijttewaal,	TU Delft
	Dr. ir. Bas Hofland,	TU Delft
	Dr. ir. Xuexue Chen,	TU Delft
	Ir. Maximilian Streicher,	Ghent University

Faculty of Civil Engineering and Geosciences (CiTG)

Delft University of Technology

In collaboration with:

Keywords: Physical modelling, wave impacts, scale effects, Froude scaling, overtopping, storm wall, impact force, post-overtopping flow, terrestrial lease scanner, measurement techniques, bore impacts, pre-impact flow evolution.

Front covert: A look towards the wave generating board from inside Deltares' Delta flume, where the WALOWA physical modelling tests were conducted. The picture was taken after finishing a successful day of testing around the end of the WALOWA test campaign.

Acknowledgement: The work described in this publication was supported by the European Community's Horizon 2020 Research and Innovation Programme through the grant to HYDRALA-PLUS, Contract no. 654110.

The Erasmus+: Erasmus Mundus MSc in Coastal and Marine Engineering and Management is an integrated programme including mobility organized by five European partner institutions, coordinated by Norwegian University of Science and Technology (NTNU).

The joint study programme of 120 ECTS credits (two years full-time) has been obtained at two or three of the five CoMEM partner institutions:

- Norges Teknisk- Naturvitenskapelige Universitet (NTNU) Trondheim, Norway
- Technische Universiteit (TU) Delft, The Netherlands
- Universitat Politècnica de Catalunya (UPC). BarcelonaTech. Barcelona, Spain
- University of Southampton, Southampton, Great Britain
- City, University London, London, Great Britain

During the first three semesters of the programme, students study at two or three different universities depending on their track of study. In the fourth and final semester an MSc project and thesis has to be completed. The two-year CoMEM programme leads to a multiple set of officially recognized MSc diploma certificates. These will be issued by the universities that have been attended by the student. The transcripts issued with the MSc Diploma Certificate of each university include grades/marks and credits for each subject.

Information regarding the CoMEM programme can be obtained from the programme coordinator:

Øivind A. Arntsen, Dr.ing.
Associate professor in Marine Civil Engineering
Department of Civil and Transport Engineering
NTNU Norway
Telephone: +4773594625 Cell: +4792650455 Fax: + 4773597021
Email: oivind.arntsen@ntnu.no

CoMEM URL: https://www.ntnu.edu/studies/mscomem

Abstract

Low-lying countries such as Belgium and the Netherlands are naturally susceptible to overtopping wave attacks. Coastal regions are therefore facing the threat of such events causing damage to dike-positioned structures and buildings. Research in this filed is often conducted using scaled-down 2D hydraulic physical models, which introduces so called *scale effects* that can bias the results with regard to measured wave-structure impact forces. This thesis therefore attempts to determine the effects of scaling for post-overtopping wave impacts. To achieve this, large scale physical modelling tests were conducted at Deltares' *Delta flume* and compared with a small scale model of similar configuration. A second thesis aim stems from the application of measurement devices in an innovative manner while conducting the large scale tests, and their applicability is assessed here.

The model comparison shows that in general the small scale test performs very similarly to its large scale counterpart, and scaling effects did not appear to bias the impact events considerably. This was also observed for the pre-impact flow evolution, where the wave interference mechanisms and resulting bore characteristics were also largely similar. The force-time signal for the largest impact also is related to the pre-impact mechanisms observed. Classification of the extreme bore impacts according to their impact peak ratio did outline a discrepancy between the two models, which was also linked to the difference in entrapped air pocket impacts.

The four measurement instruments assessed are a Terrestrial Laser Scanner (TLS), waterproof action camera(s), optical phase detection probe (OPDP) and a high speed camera mounted behind an opening in the impacted wall. Data from the former two was also used in this analysis and their performance was determined to be good.

Acknowledgements

The completion of this thesis marks the final step of a journey towards obtaining the Erasmus Mundus MSc in Coastal and Marine Engineering and Management (CoMEM) degree. This research was conducted over the last 5 months in part at Deltares thanks to the Hydralab+ funded Wave Loads on Walls (WALOWA) collaborative project.

I would first like to express my gratitude towards my committee. This work would not have been possible without your support and valuable feedback. I consider myself immensely lucky to have been under the supervision of such talented, experienced, and knowledgeable researchers. I especially want to thank Bas Hofland for his contributions as a daily supervisor, and for being the main reason why I got the opportunity to participate in the WALOWA project. Most of all, however, I valued your approachable nature and positive, problem-solving attitude. To Wim Uijttewaal, for heading the committee, and for your advice, critical thinking, and insightful questions. Thank you to Maximilian Streicher for his support throughout this thesis. From construction of the physical model to providing the test data that facilitated this research, and all the emails in between. Thank you to Xuexue Chen for your valuable feedback, and for sharing your vast knowledge on wave impacts with me.

Deltares was the home of the large scale physical hydraulic tests conducted under the WALOWA project. I would like to thank the employees and technicians there for their contribution, assistance, and patience, and for always making me feel welcomed. I also want to express my gratitude towards all the members of the WALOWA project. Following a compact test schedule was made easier by being part of such a great team. I wish to you all success with your research.

I especially want to thank my family for their seemingly endless support throughout my endeavours. Mom, dad, you are the people I owe the most to. Thank you for your love and support. To my dear sister, thank you for setting such a good example for me, and for being my link to home. I also thank my Bulgarian friends for being there for me in those moments when a quick call and a bit of encouragement was all I needed.

Two years filled with challenges, emotions, dedication, and hard work flew by in what feels like a moment. Looking back, it is hard to deny the value of undertaking a master's course in such a challenging, but endlessly captivating field. I would like to express my gratitude towards the CoMEM board for making this study opportunity a reality. I am also grateful to all the professors and staff at the institutions that are part of the CoMEM programme. Your supportive and friendly attitude made us feel welcomed each semester.

Last but not least, this experience would not have been the same without all my CoMEM friends. Between Delft, Trondheim and Southampton, you were the one constant throughout this journey. From the classrooms to the road trips, I am forever grateful for our time together. We may part ways soon, but you will always remain in my heart.

Krasimir Krasimirov Marinov
Delft, July 2017

Table of Contents

Abbreviations

ARC	Active Reflection Compensation
CSV	Comma Separated Value
DVR	Digital Video Recorder
ELP	Elementary Loading Process
eSATA	External Serial Advanced Technology Attachment
FoV	Field of View
FPS	Frames Per Second
GCS	Global Coordinate System
GP	GoPro
HS	High-speed (camera)
ISO	International Standards Organisation (camera sensor sensitivity)
JONSWAP	Joint North Sea Wave Project
JPEG	Joint Photographic Experts Group
LCS	Local Coordinate System
LED	Light Emitting Diode
LS	Laser Scanner
OPDP	Optical Phase Detection Probe
RSSI	Received Signal Strength Indicator
SLR	Sea Level Rise
SWL	Still Water Level
ToF	Time of Flight
USB	Universal Serial Bus
VFM	Void Fraction Meter
WALOWA	Wave Loads on Walls

Nomenclature

Symbol	**Units**	**Description**
B	m	Promenade length
C_5	-	Empirical coefficient
C_{err}	deg	Vertical axis rotation correction factor
d_0	m	Overtopping flow depth measured at the start of the dike crest (promenade)
D_{50}	µm	Median grain diameter
d_{crest}	m	Overtopping flow depth measured at the start of the dike crest (promenade)
f	Hz	Frequency
F_1	kN/m	Dynamic force peak
F_2	kN/m	Quasi-static force peak
$F_{1/250}$	kN/m	Arithmetic mean of the 1/250th largest forces for a number of waves in a test
$F_{10\%}$	kN/m	Arithmetic mean of the largest 10% of forces
F_e	kN/m	Characteristic elastic compression force
F_g	kN/m	Characteristic gravitational force
F_i	kN/m	Characteristic inertial force
F_{max}	kN/m	Maximum impact force
$F_{m,10}$	kN/m	Arithmetic mean of largest 10 forces
$F_{m,50}$	jN/m	Arithmetic mean of largest 50 forces
$F_{m,100}$	kN/m	Arithmetic mean of largest 100 forces
F_{mean}	kN/m	Arithmetic mean of all impact forces
F_p	kN/m	Characteristic pressure force
F_s	kN/m	Characteristic surface tension force
F_t	kN/m	Maximum total impact force
$F_{theoretical}$	kN/m	Theoretical hydrostatic force per m
F_μ	kN/m	Characteristic fluid friction force
$f(\beta)$	-	Empirical coefficient expressing the dike slope
g	m/s^2	Gravitational acceleration
h	m	Overtopping flow depth
h_w	m	Flow layer thickness at the impacted wall
H_{m0}	m	Incoming spectral wave height
h_{paddle}	m	Water depth at the wave board
h_{toe}	m	Water depth at the dike foot
H_s	m	Significant wave height
h_s	m	Vertical offset of laser scanner
L	m	Local wavelength
$_m$	-	Model scale
N	-	Number of waves
n	-	Ranking of impact sorted by magnitude
N_{imp}	-	Total number of wave impacts discernible from a given force-time signal
N_s	-	Number of samples
$_p$	-	Prototype scale
p	kN/m^2	Pressure
P_i	-	Probability of impact *i*
t	s	Time
$T_{m-1,0}$	s	Spectral mean wave period
T_p	s	Peak wave period
t_{sync}	ms	Time between initiation of laser scanner recording and sync pulse (test start)
t_{test}	ms	Start of test marked by sync pulse
q_{inst}	$m^3/s/m$	Instantaneous overtopping discharge at the dike crest
R	m	Distance in polar coordinates
R_0	m	Dike crest freeboard
R_{cw}	m	Freeboard measured from SWL to top of the dike wall

U	m/s	Peak bore velocity
$U_{b,avg}$	m/s	Bore front velocity averaged over the promenade
x_s	m	Horizontal offset of laser scanner
γ	-	Peak enhancement factor used for the JONSWAP irregular waves spectrum
η	m	Instantaneous water surface elevation
φ	deg	Slant angle
λ	-	Scaling factor
λ_1	-	Empirical coefficient
ϑ	deg	Angle value of polar coordinates
ϑ_{cor}	deg	Corrected angle value of polar coordinates
ρ	kg/m^3	Density of water

1. Introduction

The coasts of low-lying countries such as Belgium and the Netherlands have been under threat of storm-induced wave attacks for centuries. The current trends of climate change and coastal squeeze, combined with the natural appeal of the coastal region leave structures such as buildings exposed to impacts from overtopping waves. Contemporary design measures do not take these loads into account, which has resulted in a recent effort for their quantification and prediction. However, research in this field often relies on data acquired from small scale physical hydraulic models which are susceptible to scaling bias. This study investigates the applicability of upscaling small scale impact loads by applying Froude similitude and the ability of a scaled down model to accurately replicate large scale impact conditions in general. This is accomplished through a comparison between data from two physical hydraulic flume models with a difference in scale. The installation, operation and data processing of several instruments that facilitate the measurement of relevant parameters is also covered in this work.

1.1. Background

Coastal flooding poses a threat to communities worldwide. Low-lying countries such as the Netherlands and Belgium are especially susceptible to attacks from the sea, and this trend is only expected to be exacerbated by the ongoing global climate change (Nicholls, 2004). However, coastal regions still remain naturally appealing. The construction of protective measures such as sea dikes competes with the need for efficient use of space, which is why some structures, especially those positioned on top of a dike crest, are being exposed to the threat of impinging sea waves (Figure 1).

Figure 1: A typical Belgian coast configuration with shallow foreshores and buildings in close proximity to the sea.

Images source: Masterplan Coastal Safety Belgium – Flemish Government – Coastal Division
From: Van Doorslaer et al. (2017), p.2

Overtopping wave loads present a problem both for residents and engineers (Chen, 2016). It is currently not a common practice to include the resulting hydrodynamic forces from such impacts in the design phase, nor is there a widespread method to do so (Chen et al, 2014). Furthermore, most contemporary studies on wave impacts have mainly focused on replicating settings that are qualitatively different in comparison to a dike-overtopping flow impact.

The long shallow foreshores of the Belgian coast result in high storm surge levels and cause impinging storm waves to break seaward of the shoreline (Derondea et al., 2006; Haerensa et al., 2012). When overtopping of the protective dike occurs, the resulting flow resembles a bore, propagating along a dike's crest until an impact occurs with a nearby structure (Chen, 2016). Notable research specifically related to the bore-like post-overtopping flow impacts for the Belgian setting includes the works of Chen (2016), Streicher et al. (2016) and Van Doorslaer et al. (2017), amongst other. In their research one inevitably finds the inclusion of hydraulic physical models serving as basis for (impact load) data acquisition. More often than not these models are conducted at relatively small scales through the application of Froude similitude. The issue with Froude scaling law (or any scaling law, for that matter) is that it is an imperfect representation of the actual, real-world physical phenomena (Heller, 2011). This leads to the introduction of *scaling bias* – discrepancies between the model and the prototype conditions, which is inversely proportionate to the model scale (Heller, 2011). These discrepancies (also often termed *scale effects*) have been shown to affect the impact forces and impact mechanism in general for wave-structure collisions (e.g. Bullock et al., 2001; Lafeber et al., 2012a, 2012b). It stands to reason then that before extrapolating conclusions for post-overtopping flow impacts drawn on small scale impact data, the ability of such Froude-scaled models to replicate prototype-scale impacts should be assessed.

1.2. Scope and research objectives

The first aim of this thesis is to determine the effects of scaling bias in post-overtopping wave impacts by means of comparing a large scale 1:4.3 physical hydraulic model to its similar, Froude-downscaled 1:25 counterpart.

The second aim is to assess the applicability of innovative and experimental measurement approaches in large scale hydraulic physical modelling tests.

With regard to these two aims, the following objectives are set:

- Understanding the underlying physical principles of Froude scaling, the scaling bias it introduces with regard to wave impacts in the setting of a post-overtopping bore-like wave impact with a rigid structure;
- Obtaining force and post-overtopping wave measurements from a large scale hydraulic physical model to compare to existing data from a small scale model;
- Quantifying differences in the force-time evolution of the maximum wave-induced forces between the two hydraulic models and assessing how these relate to scaling bias;
- Assessing the effectiveness of the small scale model to reproduce the conditions observed at large scale for the pre-impact flow evolution of the largest impact events;
- Investigating the applicability of a Terrestrial Laser Scanner (TLS) for overtopping flow measurements over a complex compound profile;
- Assessment of the feasibility and practicality of implementing waterproof action cameras as measuring devices in a large scale hydraulic flume environmentl;
- Assessment of the implementation of a see-through opening in the impacted wall in combination with video recording equipment, and an optical phase detection probe (OPDP) for void fraction measurements.

1.3. Approach

In order to obtain data for the present investigation of scale effects, measurements from two physical models at two different scales needed to be compared. A 1:4.3 scale physical model was carried out in the Delta flume of Deltares under the collaborative Wave Loads on Walls (WALOWA) project in early 2017. This project was financed by a grant by Hydralab+ in the framework of the EC Horizon 2020 program. Conducting the small scale model experiments was previously done at Ghent University by the authors of Streicher et al. (2016), who kindly provided data for comparison purposes. Relevant parameters relating to the post-overtopping flow and resulting impact forces were compared at both scales to assess whether the influence of scaling bias is present and quantifiable. The model performance in replicating the conditions observed at large scale was also evaluated. Assessment of the applicability of the aforementioned measuring devices stems from their use during the large scale tests campaign. Subsequently, data processing was performed for several of these instruments for obtaining parameters relevant to this research.

1.4. Thesis outline

This work is structured as follows. A theoretical background is given in Chapter 2. This chapter consist of a review of the Belgian coastline and a study of previous literature regarding overtopping wave impacts for a typical Belgian setting. This is followed by a review of Froude scaling and publications related to the scaling bias it introduces in the context of wave impacts. Chapter 3 introduces the model setup for both the large and small scale tests, with expanded elaboration on the innovative measurement devices used in the former. The methods for obtaining and processing data constitute the later part of that chapter. Chapter 4 contains the results and discussion portion of this thesis, where the comparison between the two models is elaborated on. Focus is kepts on the impact forces, pre-impact flow evolution, and comparative performance of the two models. Lastly, Chapter 5 outlines the conclusions related to the present study and recommendations for improvement. Here, recommendations relating to the second aim of the thesis are also presented.

2. Theoretical Background

The aims introduced in Section 1.2 cover a broad spectrum of theoretical background, from loads induced by dike-overtopping waves to scaling effects in physical modelling. In general, this chapter can be understood as introducing three key points. The first one involves understanding the setting of the Belgian coastline and its inherent vulnerability to wave overtopping, followed by a review of contemporary research on post-overtopping flow-induced loads on a dike-positioned structure. A second key point is the study of modelling effects, which are biases brought by the fact that it is impossible, or at the very least not feasible, to accurately scale the balance of the governing forces from *model* to *prototype* scale. The final step is a deeper understanding of the scaling biases with regard to wave impacts, including aeration of the water body, and what effects these result in.

Section 2.1. briefly introduces the Belgian coastline and the importance of understanding impact forces due to overtopping waves. Next, description of, and prediction methods for impact loads due to post-overtopping flow impacting a dike crest positioned structure are outlined in Section 2.2. Section 2.3. briefly outlines Froude similitude and how it introduces scaling effects, followed by a distinction of entrainment and entrapment of air in Section 2.4. A qualitative understanding of the scaling biases in Froude scaling is introduced in Section 2.5. following previous published research, and specifically introducing the concept of *elementary loading processes*. Lastly, a concise summary of key points is provided in Section 2.6.

2.1. The Belgian coastline

2.1.1. A brief overview

The Belgian coastline borders the North Sea and is around 67 km long (Cantersa, et al., 2014), aligned along a southwest-northeast axis. It is part of the southern sandy North Sea coastline system and is generally uniform, with wide, gently sloping sandy beaches classified as dissipative (Haerensa, et al., 2012). The beach gradient starts at 1.3% to the southwest and increases to 2.4% to the northeast (Derondea, et al., 2006), or an approximate slope of 1:77 and 1:42, respectively. The naturally occurring beach grade sediment is well sorted fine to medium-grained sand (Lebbe, et al., 2008). Dunes back the beaches, behind which one finds vast low-lying flat hinterland. Cantersa et al. (2014) noted that over the entire Belgian coastline, 85 % of the hinterland is below 5 m elevation, reach up to 20 km inland.

The entirety of the Belgian coast is classified as macro-tidal, with a semi-diurnal tide and a typical range between 3.5 m (neap tide) to 5 m (spring tide) (Haerensa, et al., 2012). Wind waves are typically short-crested, generated by westerly winds (Haerensa, et al., 2012). An important aspect are the notable storm surge events that can occur for winds within the southwest-northwest spectrum and especially for north-northwest-oriented winds (Haerensa, et al., 2012) (Bosboom & Stive, 2015). With regard to anthropogenic factors, (Lebbe, et al., 2008) point out that about 60% of the coast is protected by engineering interventions – groynes, dikes or soft engineering measures. The Belgian coastal region is also densely populated (Cantersa, et al., 2014) and of national economic importance (Lebbe, et al., 2008).

2.1.2. Flood risk and climate change

Flood risk is generally defined as the *probability* of a flood event *times* the *consequences* of that event (Jonkman & Schweckendiek, 2015). Regarding Belgium, four main factors constitute the country's vulnerability to coastal floods and flood risk:

- Low-lying hinterland (e.g. Cantersa, et al., 2014)
- Macro-tidal setting (e.g. Haerensa, et al., 2012)
- Significant storm surges (e.g. Haerensa, et al., 2012)
- Overall dense anthropogenic use and economic significance of the coastline (Lebbe, et al., 2008)

Additional factors should be considered. For example, Lebbe et al. (2008) mention that the natural development of the country's inherent protective barrier – its sand dunes, is being inhibited by urbanisation. Another factor is global climate change and the resulting sea level rise (SLR) and increased extreem weather phenomenon (e.g. severe storm surge events). Within the context of flood risk management, these both increase the *probability* side of the basic flood risk formula.

2.1.3. Consequences to urbanized areas

Both SLR and increased frequency and severity of storm surges will lead to increased overtopping. In this context, the definition of wave overtopping is a flow of water running up a dike slope, then reaching and surpassing the dike's crest. This is caused by incoming (wind-generated) waves, whereas the still water level (SWL) does not exceed the dike crest elevation (Jonkman & Schweckendiek, 2015). Narrowing the spectrum to urban areas, Van Doorslaer, et al. (2017) point out the threat this poses to Belgian coastal cities and the need for more research on the consequences to planned and existing structures (see also: Chen, 2016). Hydrodynamic loading on structures such as buildings due to a dike-overtopping flow is a field that currently lacks standardized design procedures and assessment mechanisms (Chen, et al., 2012). In view of the increasing probability and frequency of such events ocurring (e.g. Nicholls, 2004; Jonkman, 2005), the impact forces they cause should be a prime consideration for engineers and residents (Chen, 2016).

2.2. Overtopping wave loads on a structure

Having outlined the characteristics of the Belgian coastline and the contemporary issue of overtopping wave impacts on structures, here relevant research on the latter is presented. Wave run-up and overtopping is a phenomenon extensively covered in research literature (see e.g. Van Gent, 2001; Schüttrumpf & Oumeraci, 2005; Van der Meer, et al., 2010) and design manuals (e.g. EurOtop, 2016). This is also the case for wave-induced forces exerted by waves breaking on structures, usually (but not necessarily) in deep water conditions (e.g. Oumeraci et al., 1993; Bullock et al., 2001, 2007). However, less researchers have focused on the specifics of an incoming waves overtopping a dike, and the resulting overtopping flow impacting a structure positioned on the flat part of the dike crest (termed promenade), as is the case for the Belgian coast (Figure 2).

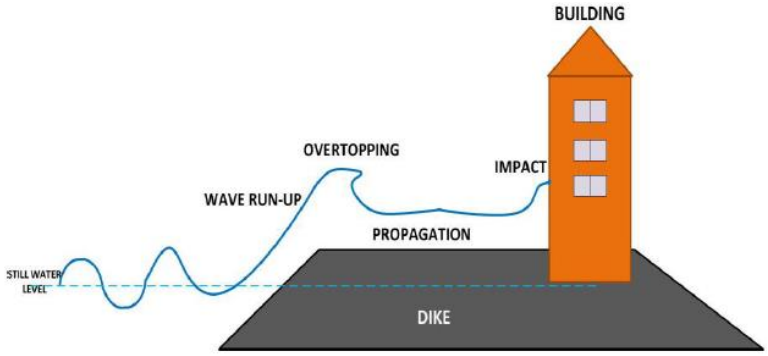

Figure 2: Schematic representation of an overtopping flow impacting a structure.
Source: Chen et al. (2012), p. 1

For a setting as the one shown in Figure 2, Chen (2016) noted based on Cox & Machemehl (1986) and Battjes (1974) that the resultant flow over the dike when an overtopping event occurs qualitatively resembles a bore-like wave (see also: Chen et al., 2014; Streicher et al., 2016). Furthermore, the flow has been observed to be highly turbulent and highly aerated (Streicher, et al., 2016) (Chen, 2016). This has been proposed as a source of variation in the measured forces between identical tests (De Rouck et al., 2012; Ramachandran et al., 2012; Streicher et al., 2016). An additional contribution to the stochastic nature of the process has also been attributed to wave-to-wave interaction and residual water layers occurring on the promenade (Chen, 2016; Streicher et al., 2016). Flow interactions usually stem from the occurring reflection of an impinging overtopping flow at the wall interface. For a setup qualitatively similar to Figure 2, Chen et al. (2014) identified and classified two overtopping flow interference patterns, termed ***interaction***, and ***wet bed***.

Interaction occurs when there is a collision between an incoming and an already reflected flow occurring over the flat surface of the dike (the promenade). Streicher et al. (2016) also observed how this mechanism can cause air pockets to be trapped between the wave body and the impacted structure. On the other hand, *wet bed* means that the reflected flow following a previous overtopping event has had enough time to mostly drain after reflection, but still leaves a residual water layer on the promenade. For regular wave conditions, the occurrence of either can reasonably be attributed to the wave period of the incoming waves (Chen, et al., 2012). Naturally, this interference affects the impinging overtopping flow characteristics, and therefore the loads on the wall, and is further elaborated on in Sections 2.2.1.

2.2.1. Force-time signal evolution

The force-time signal for a post-overtopping wave impact with a structure has been shown to typically consist of two peaks (Figure 3): a *dynamic force peak* and a *quasi-static force peak* (e.g. Chen et al., 2012; De Rouck et al., 2012; Chen, 2016). Chen et al. (2014) noted how this resembles the double-peaked or 'church-roof' shape observed by Oumeraci et al. (1993) for breaking wave impacts on a structure, however, the classifications of impact mechanisms of the latter are not suitable for the present case. Instead, the classification by Chen et al. (2014) is introduced here, which was derived for post-overtopping flow impacts on a flat wall.

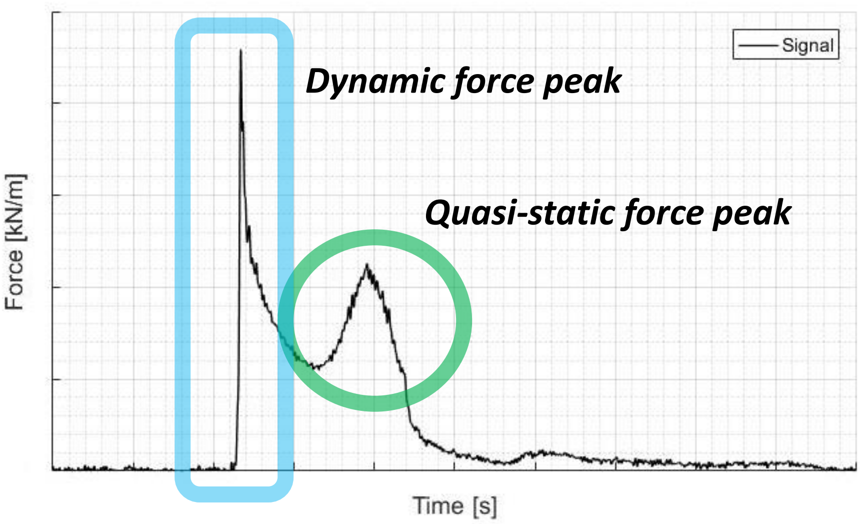

Figure 3: A typical force-time signal for an overtopping flow impact event. Note the two force peaks in the signal – dynamic and quasi-static.

Impact mechanism

For regular waves and for a *wet bed* interference pattern between incoming and reflected waves, Chen et al. (2014) identified 4 stages: *pre-impact, initial impact, deflection, and reflection*, occurring in consecutive order. Furthermore, these were linked to the pressures measured at the wall. All stages and their corresponding position in the pressure-time signal are summarized in Figure 4.

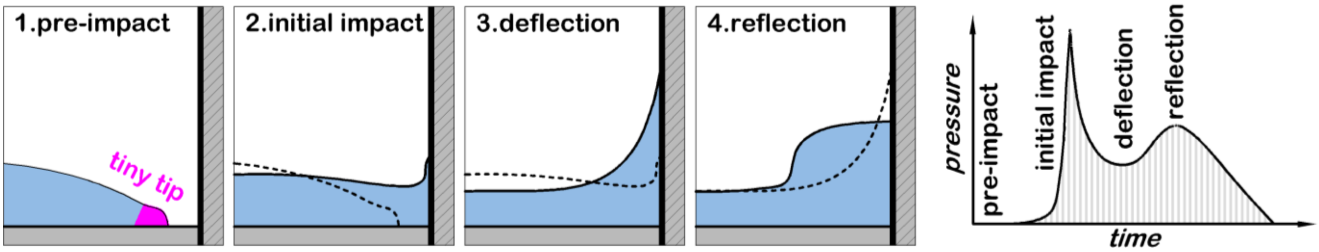

Figure 4: Schematic representation of the four stages of a bore impact and their corresponding position in the pressure-time signal as defined by Chen et al. (2014).

The ***pre-impact*** stage, as the name suggests, covers the timeframe after the dike crest has been overtopped, but before an impact with the structure occurs. At this stage, the flow is propagating and transforming along the dike top, and is turbulent and highly aerated (Chen, et al., 2014). The authors also observed the formation of a so-called 'tiny tip' – a leading water wedge at the very front of the overtopping flow.

The ***initial impact*** stage follows, where the 'tiny tip' impacts the wall first (termed *tiny jet impact*), followed by the rest of the bore front (termed *initial main impact*). Chen et al. (2014) proposed that the tiny jet impact first striking, and afterwards deflecting upwards along the wall surface reduces the impact load exerted by the following bore front, a mechanism corresponding to the restricted trough observations of Lafeber et al. (2012b) - see Section 2.5.1. Once the bore front impacts the structure, a sharp increase in pressure is observed, which corresponds to the *dynamic force peak* shown in Figure 3 (Chen, et al., 2014). The authors suggest that due to the short duration of this initial impact, only structural elements with a high natural frequency will be affected by it (see also: Chen, 2016).

Next, the ***deflection*** stage includes the rising of the water body along the wall until maximum run-up height is reached. Chen et al. (2014) observed a heightwise linear distribution of the pressure on the wall, however, the values were lower than the computed hydrostatic pressure. Finally, after reaching maximum run-up, the flow starts falling on the remaining water body below it and to return backwards, forming a reflected bore. This is termed as the ***reflection*** stage, and is when the second peak in the force-time signal is observed i.e. the *quasi-*

static force peak in Figure 3. Furthermore, Chen et al. (2014) observed an almost linear distribution of the instant pressure vertically along the wall with values close to calculated hydrostatic pressure.

Impact types

In reality however, the classic 'church-roof' shape of the force-time signal as shown in Figure 3 is not observed for every impact. For example, Streicher et al. (2016) distinguished 3 types of impacts based on physical tests in a flume for irregular waves and a setup very similar to the one later presented in Section 3.1. These can be seen in Figure 5 and were referred to as:

- Dynamic bore impact;
- Quasi-static/down-rush bore impact;
- Pulsating bore impact.

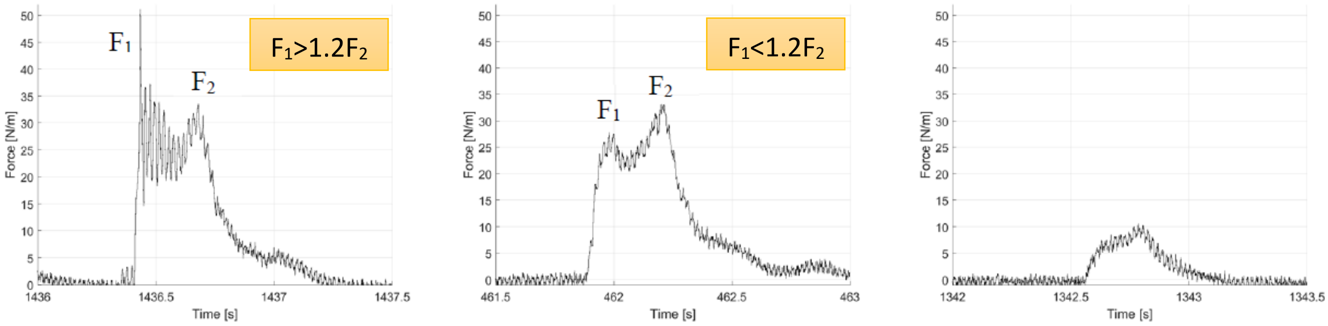

Figure 5: Three impact types distinguished on the basis of their force-time signal evolution, as identified by Streicher et al. (2016).

Adapted from: Streicher et al. (2016), p. 5

The distinctions between the 3 types of impacts were made based on the signal evolution and bore characteristics (Streicher, et al., 2016). ***Dynamic bore impacts*** (Figure 5, left) were defined by the authors as having a dominant dynamic force peak. *Interaction* interference between incoming and reflected bores occurring just before the wall were observed in almost three-quarters of these impacts, often trapping an air pocket between the crest and the wall (Streicher, et al., 2016). The remaining quarter showed no interference with a reflected bore, however, a steep bore front, high layer thickness and flow velocity were all observed (Streicher, et al., 2016).

For ***Quasi-static/down-rush bore impacts*** (Figure 5, centre), Streicher et al. (2016) observed an impact sequence very similar to the one proposed by Chen et al. (2014), presented previously in this section. The third type, ***pulsating bore impact***, were described by Streicher et al. (2016) as smoothly running-up on the wall and reflecting back, without interacting with other bores. The authors also observed a very gentle bore front slope and shallow overtopping flow layer thickness. A summary of the three impact types and their characteristics is presented in Table 1.

Table 1: Summary of impact types and characteristics as defined by Streicher et al. (2016).

Impact type	**Interaction interference**	**Force ratio F1/F2**	**Notable characteristics**
Dynamic bore impact	Yes (3/4 of cases)	> 1.2	Bore-to-bore interaction, air pocket
	No (1/4 of cases)		Steep front, large layer thickness, high incoming velocity
Quasi-static/ down-rush bore impact	No	< 1.2	As for impact mechanism in Chen et al. (2014)
Pulsating bore impact	No	-	Gentle slope, small layer thickness, smooth run-up

2.2.2. Predicting impact forces

Several researchers have attempted to formulate an expression predicting the maximum impacts on the wall for an overtopping flow impact in a setting similar to Figure 2. The governing parameters are usually related to model geometry, incident waves, and the post-overtopping flow.

In their test programme, Streicher et al. (2016) measured the incoming bore front velocity on the promenade as it passed over two wave gauges. This provides a partially-averaged value, since the wave gauges covered only a portion of the whole crest length. They observed poor correlation between the measured velocity and recorded impact forces (Figure 6- right). Streicher et al. (2016) also used the wave gauge closest to the wall (about 5 cm) to measure the maximum layer thickness of the bore. In reality, this measurement should be regarded as a partial run-up value for an overtopping event due to the proximity of the wave gauge to the wall. Regardless, the author reported a much stronger correlation with the forces observed at the wall (Figure 6- left). This makes sense for the *quasi-static/down-rush bore* and *pulsating bore* impacts where there is a dominant second peak (or no distinguishable leak in the latter case), and these types of impacts tend to correlate well with the layer thickness, this trend being less obvious for the highest impact events.

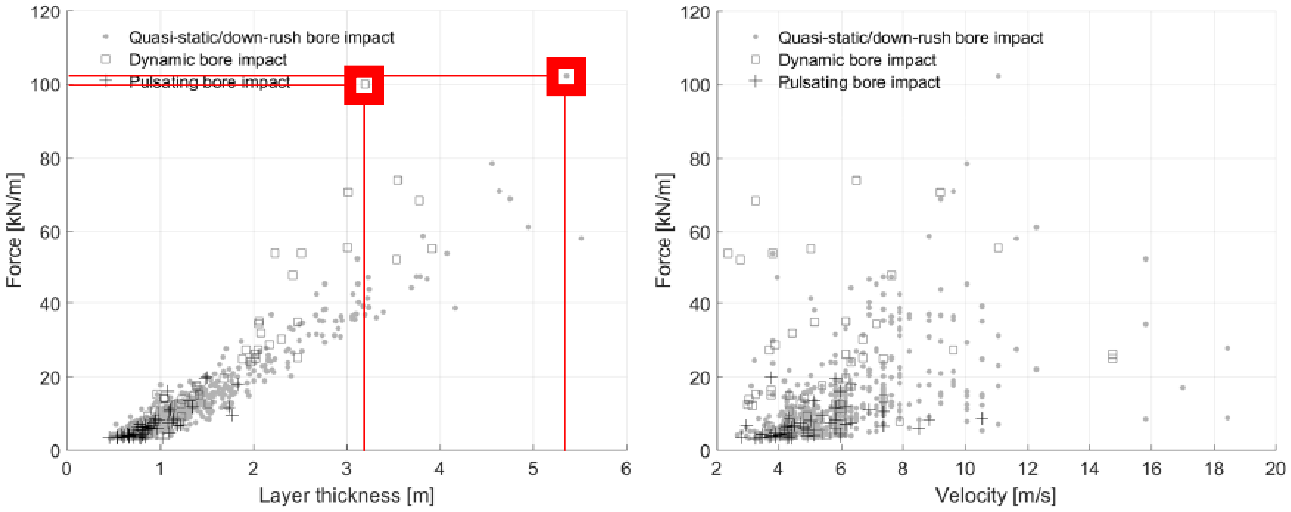

Figure 6: Correlation between the impact force of an event and the layer thickness at the wall (left) and bore front velocity (right). Note the distinction between the impact types after Streicher et al. (2016). The red squares mark the two highest impact events. All values in prototype scale.

Adapted from: Streicher et al. (2016), p. 8

Dynamic bore impacts on the other hand tend to produce large impact pressures for a relatively low flow layer thickness (Streicher, et al., 2016). The red squares in Figure 6- left, indicate the two highest impact events in the tests of Streicher et al. (2016). An interesting observation is that the second highest recorded event, a *dynamic bore impact*, produced 97% of the maximum recorded force (which was a *quasi-static/down-rush bore*) for a 40% lower layer thickness, meaning there is a further, important mechanism that is missing. As discussed, this is largely attributed to bore-to-bore interferences before an impact. Chen (2016) also remarked that high impact pressures occur when a ‘collision’ (corresponding to the *interaction* classification of Chen et al., 2014) is present close to the wall. In their physical modelling tests (Van Doorslaer, et al., 2017) observed that typically the largest loads on the wall can be attributed to force-time signals with a sharp, dominating first peak (Figure 3), corresponding to *dynamic bore impact* type as defined by Streicher et al. (2016).

As a first approximation, Streicher et al. (2016) used a theoretical hydrostatic pressure formula (Eq. 2.1.) – see Figure 7, and found an overall good fit for the lower impacts (up to 25 kN/m in prototype scale). This formula generally overestimated *dynamic bore* impacts, and *quasi-static/down-rush bore* impacts tended to be underestimated above a certain threshold, possibly due to the imprecise run-up measurement (Streicher, et al., 2016).

$$F_{theoretical} = \frac{1}{2}\rho g h^2 \tag{2.1.}$$

where $F_{theoretical}$ is the theoretical hydrostatic force per m, ρ is the density of water, g the gravitational acceleration constant, and h the flow layer thickness at the wall.

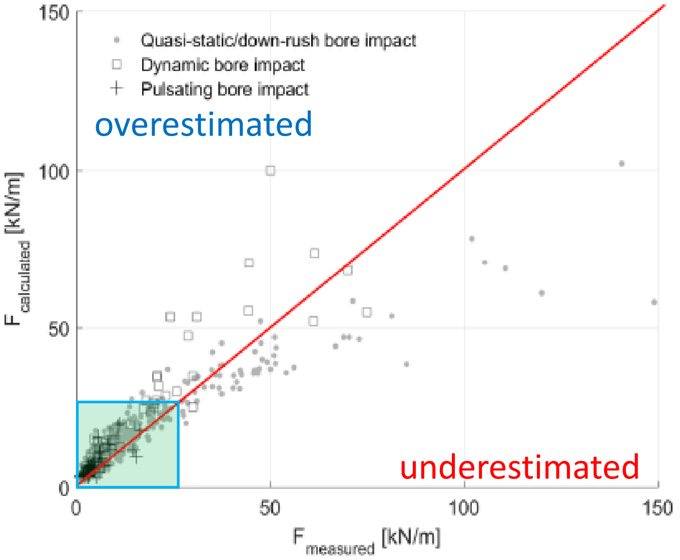

Figure 7: Measured impacts compared to the calculated theoretical hydrostatic pressure. Values in prototype scale. The y-axis corresponds to $F_{theoretical}$ calculated using Eq. 2.1.

Adapted from: Streicher et al. (2016), p. 9

Another formulation for estimating the force on the wall for a single overtopping event was proposed by Chen (2016) – Eq. 2.2. This is based on the maximum depth-integrated momentum flux, which is proportional to the mass of the water that constitutes the overtopping wedge (Chen, 2016). This formula includes several coefficients that have to be determined experimentally and is based on regular waves. Furthermore, Chen's model setup, although similar, varied from the experimental setup of the WALOWA tests (see Section 3.2.), which means the latter is outside the formula's applicable range as defined by Chen (2016). Nevertheless, Eq. 2.2. gives and insight into the relevant parameters for estimating the forces, as noted by Van Doorslaer et al. (2017).

$$\frac{F_t}{C_5 f(\beta)\rho g d_0^2} = \exp\left(-\lambda_1 \frac{B}{L}\right) \tag{2.2.}$$

where F_t is the maximum total impact force, d_0 the overtopping flow depth at the start point of the dike crest, B the promenade length, L the local wave length, and C_5, $f(\beta)$ and λ are empirical coefficients determined experimentally. As Van Doorslaer et al. (2017) remarked, notable is the involvement of the overtopping flow layer depth squared, the promenade length and the slope of the dike (contained in $f(\beta)$) with regard to predicting the forces on the wall.

Van Doorslaer et al. (2017) themselves proposed 3 equations (two of which are presented here) based on data acquired from three sets of physical modelling tests. Moreover, the former were derived for irregular wave conditions. For Eq. 2.3. the authors' goal was to link the incident wave parameters to the forces on the wall, noting the **freeboard** (R_{cw}) (here defined as the height difference between the still water level (SWL) and top of the wall) and **wave height** (H_{m0}) as the most important parameters (Van Doorslaer, et al., 2017).

$$\frac{F_{1/250}}{\rho g R_{cw}^2} = 7.8\exp\left(-2.02\frac{R_{cw}}{H_{m0}}\right) \tag{2.3.}$$

where $F_{1/250}$ is the average force of the top 1/250 waves (4 force measurements in the case of a 1000 wave test), R_{cw} is the freeboard of the wall (SWL to top of wall), H_{m0} is the incoming spectral wave height, and 7.8 and 2.02 are the empirical coefficients *a* and *b*, respectively, as derived by Van Doorslaer et al. (2017).

On the other hand, Eq. 2.4. explores only the relation between overtopping flow characteristics and force, negating the incoming wave parameters. The governing parameters were defined by Van Doorslaer et al. (2017) to be the **overtopping flow depth** (*h*) and **bore front velocity** (*U*). Furthermore, they noted that both values are necessary for force estimation, as no single value showed good correlation to the measured forces at the wall. However, there is a decay observed in both parameters during the propagation stage of the bore along the promenade (Van Doorslaer, et al., 2017). Therefore, the authors remarked, the location where these parameters are measured is paramount to the correct determination of the forces. In their 1:6 scale tests, Van Doorslaer et al. (2017) measured the flow depth 2.1 m before the wall (promenade length is 10 m, both distances in prototype scale) and the bore front velocity propagating from the same point until the wall. Eq. 2.4. is corrected for measurements taken at (or very near) the dike crest (seaward extent of the promenade).

$$\frac{F}{\rho g R_{cw}^{2}} = 0.40\exp\left(\frac{Uh}{\sqrt{gR_{cw}^{3}}}\right)^{1.313} \tag{2.4.}$$

where *F* is the force on the wall, *U* is the bore front velocity, *h* is the flow depth, and the values 0.576 and 1.313 are empirically derived for the particular tests. One remark is that this equation, at least in the conditions tested by the authors, did not show erroneous results when *interaction* and *wet bed* interference patterns were compared to individual bore impacts.

Van Doorslaer et al. (2017) recommend the use of Eq. 2.3. as a simple method to estimate the highest impacts on the wall. It also showed the highest prediction accuracy for their experiments. Eq. 2.4. on the other hand is recommended for its versitility, being possibly applicable for varying model geometry (Van Doorslaer, et al., 2017), although no robust testing of this claim has been shown by the authors themselves. Furthermore, it is possible to obtain the complete force distribution over the entire test length by linking it to the distribution of the instantenious discharges ($q_{inst}=Uh$), although the decay of both *U* and *h* as the bore propagates along the promenade is then difficult to determine (Van Doorslaer, et al., 2017). An important remark is that the empirical parameters in Eq. 2.3. and 2.4. were obtained for tests that do not match the WALOWA model setup (Section 3.1.) completely, which means that applying these will likely introduce at least some bias in the results. Nevertheless, the authors' claim for the large applicability of Eq. 2.4. can be tested.

2.3. Scaling in physical modelling

Before exploring the issue of scaling bias, it is important to understand why and how scaling is applied to hydraulic physical models. The principles of scaling, and of Froude scaling in particular, are briefly outlined in this section, and enable a further in-depth look at scaling bias outlined in Section 2.5.

Physical modelling is a commonly used tool for reproducing real world scenarios in a scaled down, model 'universe', to benefit in understanding and solving issues in the fields of hydraulic engineering and fluid mechanics (Frostick, et al., 2011). *Full* or *prototype scale* models are often not possible due to e.g. time constraints, limited access to large testing facilities, or are simply not economically-feasible (Heller, 2011; Frostick et al., 2011). A scaled-down (also termed *model scale*) model can be considered as representative of the prototype, real world conditions only if the appropriate scaling laws are applied (Frostick, et al., 2011) This is also often termed maintaining similarity or *similitude* between the two systems. The scaling factor is hereafter denoted λ and should be understood as:

$$\frac{Model\,scale}{Prototype\,scale} = \frac{1}{\lambda} \tag{2.5.}$$

Maintaining a complete similarity between two model scales requires that the two meet the following conditions (Heller, 2011):

- Geometric similarity – similarity in shape;
- Kinematic similarity – similarity in motion; also implies geometric similarity;
- Dynamic similarity – maintaining all force ratios; also implies geometric and kinematic similarity.

Assuming that the conditions for both geometric and kinematic similitude are met, dynamic similitude will require that the following forces are balanced in both scales (Frostick, et al., 2011, p. 12):

$$\frac{(F_i)_p}{(F_i)_m}=\frac{(F_g)_p}{(F_g)_m}=\frac{(F_\mu)_p}{(F_\mu)_m}=\frac{(F_e)_p}{(F_e)_m}=\frac{(F_p)_p}{(F_p)_m}=\frac{(F_s)_p}{(F_s)_m}=\lambda \qquad (2.6.)$$

where *F* – characteristic force; and indices represent: *i* – inertial force; *g* – gravitational force; *μ* - fluid friction force; *e* – elastic compression force; *p* – pressure force; *s* – surface tension force; and *p* – prototype scale; *m* – model scale.

However, maintaining constant ratios between all forces in Eq. 2.6. at both scales cannot be achieved (Frostick, et al., 2011). Therefore, *scaling bias* or *scale effects* will always exist when model scale tests are conducted (Heller, 2011). Furthermore, the scaling bias will generally increase as the scaling factor *λ* between the *model* and *prototype* increases (Heller, 2011). Hence, it is important to consider the dominant forces and apply the appropriate scaling law (Frostick, et al., 2011).

2.3.1. Froude scaling

Also termed *Froude law* or *Froude similitude*, this is a scaling principle usually applied when modelling scenarios where the dominant restoring force is gravity (Bullock, et al., 2001). The principles of geometric and kinematic similarity still hold true. For achieving dynamic similarity however, maintaining the balance between the *inertial* and *gravitational* forces is paramount (Bullock, et al., 2001), whereas balancing all other forces is neglected (Frostick, et al., 2011). Froude similitude requires (Bullock et al., 2001; Heller, 2011):

$$\frac{u_p}{\sqrt{L_p g}}=\frac{u_m}{\sqrt{L_m g}} \qquad (2.7.)$$

where *u* is a characteristic velocity, *L* is a characteristic length, *g* is the gravitational acceleration, and indices *p* and *m* denote *prototype* and *model* scale, respectively. Scaling pressure forces and time between the two systems is therefore achieved by:

$$p_p=\frac{\rho_p L_p}{\rho_m L_m}p_m=\frac{\rho_p}{\rho_m}\lambda p_m \qquad (2.8.)$$

$$t_p=\sqrt{\frac{L_p}{L_m}}t_m=\sqrt{\lambda}t_m \qquad (2.9.)$$

where *p* is pressure, *t* is time, *ρ* is the water density and *λ* is the scaling factor. Including the water density ρ is important since it is common to use fresh water for physical modelling tests that simulate prototypes exposed to salt water. This in itself can introduce bias in the obtained results (Scott, 1975), but is outside the scope of this thesis.

As mentioned, since Froude scaling considers dynamic similarity only between two forces - inertial and gravitational (see Eq. 2.7.), the balance of all other forces in Eq. 2.6. is not met. In particular cases this can be a source of significant scaling effects (Heller, 2011), such as e.g. when modelling air-water flow (Blenkinsopp & Chaplin, 2011). Further elaboration on scaling effects is presented in Section 2.4.

2.4. Air void fraction, entrainment and entrapment

Section 2.2. presented research into the overtopping wave impacts for a typical Belgian coastline setup. It was noted that the overtopping bore-like wave is highly turbulent and highly aerated. Here, elaboration on the latter is presented, describing how this is generated and measured.

The (air) *void fraction* or *void ratio* (also termed *aeration* for simplicity) is a measurement of the volume of air over the total volume of the air-water mixture measured in percentages [%] (Bullock, et al., 2001). Typically, both *entrained* and *entrapped* air counts towards the total void ratio. It is important to distinguish between the two since they differ in their generation mechanisms and effects on impact pressures. This section is based on the distinctions made by Bullock et al. (2001).

When a wave approaches a structure (vertical or inclined), the surrounding air can be:

- Entrained (entrainment);
- Entrapped (entrapment);
- Expelled.

Entrainment is attributed to the presence of air bubbles within the water body (Figure 8 - right). ***Entrapment*** typically occurs when the crest of an impinging wave encloses ('traps') a pocket of air between it and the surface of the impacted structure (Figure 8 - left). If the impact pressures are sufficiently high, parts of the entrapped air pocket can also enter the water body, becoming entrained. The other mechanism for air entrainment is the turbulence of the flow. For example, a highly-turbulent flow such as in the case of the post-overtopping bore-like wave on top of the promenade (Chen, 2016), will have a high air void ratio attributed to entrainment of surrounding air. Air is *expelled* when it is displaced by a wave crest without losing contact with the surrounding atmosphere.

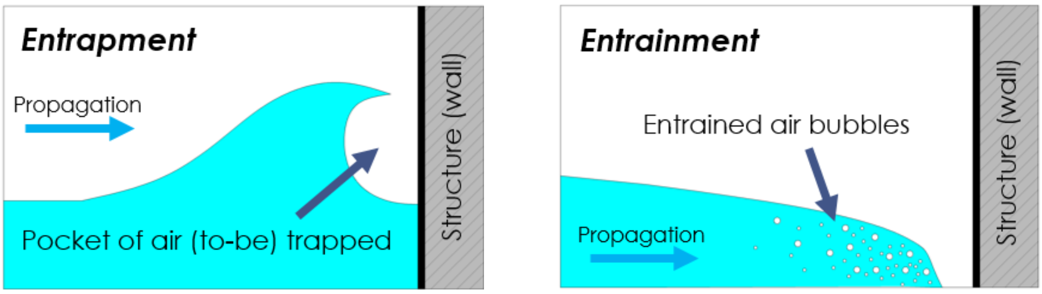

Figure 8: Schematic representation of the differences between entrapment (left) and entrainment (right) of air.

It should also be noted that entrainment and entrapment can occur at the same time, therefore, Figure 8 – left is somewhat misleading, since there will likely be air bubbles within the water body of the impinging wave as well.

2.4.1. Air void fraction effects on the pressure-time signal

As noted by Bullock et al. (2001, 2007) and Blenkinsopp & Chaplin (2011), research involving entrapped or entrained air measurements does not always agree on the effects the air-water mixture has on the resulting impacts on a structure and related forces. There is general consensus that in both cases, the increased presence of air lowers the compressibility of the air-water mixture, which in turn usually leads to a so called 'cushioning effect' – reduced maximum (peak) pressures and an increase in pressure rise times (Bullock, et al., 2007). However, multiple researchers (see e.g. Bullock et al., 2001, 2007; Lafeber, et al., 2012a) have pointed out that the total impulse or total global force on the structure is preserved, or might even increase. Therefore, these aerated impacts should not be neglected just on the basis of the reduced peak pressures.

The 'cushioning effect' is illustrated in Figure 9 taken from Bullock et al. (2001), p. 299, who conducted laboratory drop tests of a plate over a body of water at varying controlled void ratios, and recorded the impact pressures. A trend is visible where there is a notable drop in peak pressures from 0 to around 5% aeration, followed by a more gradual effect above these values. In addition, Bullock et al. (2001) note that the intensity of the ‘cushioning effect’ decreases with increasing pressures, as was also observed by Bagnold (1939) for entrapped air impacts.

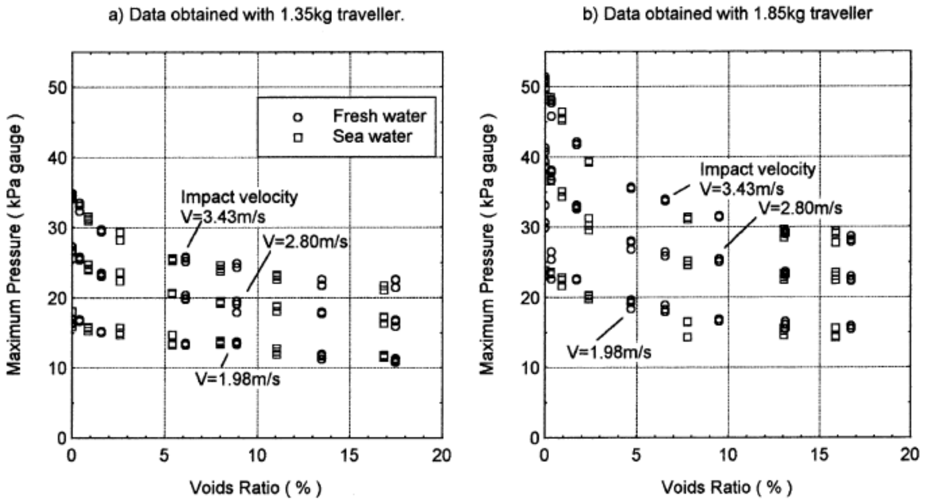

Figure 9: The effects of air content on impact pressures. With increasing void ratios (x-axis) one observes a decrease in the maximum recorded pressures (y-axis).

Source: Bullock, et al. (2001), p. 299

It should also be noted that the effects described above are in no way a hard rule and are dependent on multiple factors, which can also be linked to the varying findings by different researchers (Bullock et al., 2001; see also: Lafeber, et al., 2012b). Impact pressure data is notoriously varied even for repeat tests with identical conditions and regular waves (Bullock et al., 2007; Lafeber et al., 2012a; see also: Chen et al., 2014).

Nevertheless, the aforementioned ‘cushioning effect’ of an increasing air void fraction can generally be summarized as leading to:

- (Significant) reduction in peak pressures;
- Increase in pressure rise time;
- Conserved/increased total impulse/global impact pressure on the structure.

Instead of artificially altering the aeration of the water and comparing tests at identical scales (as shown in Figure 9), a scale-induced variation in flow aeration is also observed when using scaled down models compared to prototype scale. This phenomenon is attributed to the inaccurate representation of the flow aeration in Froude scaling, and is further elaborated in Section 2.5.4.

2.5. Scaling bias in Froude scaling

The principles of Froude scaling were presented in Section 2.3. which outlined the theoretical background behind scaling effects. This section focuses on further elaboration of scaling bias found in literature. Lafeber et al. (2012b) provide a useful breakdown of the loading processes involved in a breaking wave impact on a wall, which allows for a deeper understanding of the mechanisms at play, the governing physical processes involved, and thus the expected scaling effects when applying Froude similitude. A subsequent paper by the same authors sets an explicit goal of comparing results at two different (Froude) scales and quantifying the scaling bias. This is followed by additional scaling effects caused by air entrainment largely based on the research of Bullock, et al. (2001) and Blenkinsopp & Chaplin (2011).

2.5.1. Elementary Loading Processes (ELPs)

Conceptually, Lafeber et al. (2012b) hypothesize that the complicated process of a wave impacting a wall can be broken down into a combination of individual elementary events, called *Elementary Loading Processes*, or ELPs for short. These then can help put into context the temporal and spatial pressure signal evolution recorded during an impact event, and can explain different features observed in the signal itself. Lafeber et al. (2012b) also pinpoint the governing physics behind each individual ELP and relate those to the omissions in Froude scaling (Section 2.3.1.) to qualitatively describe expected scaling effects.

The authors obtained data from physical modelling tests at two scales:

- 1:6 scale (deemed *large scale tests* in the paper);
    - Tested both a smooth and a corrugated wall surface to-be impacted;
- Full scale/prototype scale tests at 1:1;
    - Tested only a corrugated wall surface to-be impacted.

Later, the same data set was used for the quantitative analysis of scaling effects by Lafeber et al. (2012a) – see Section 2.5.2. ELPs related only to the *large scale* tests (scale 1:6) with a smooth wall installed are considered here, since these match the scope of this thesis. These were conducted at Deltares' Scheldt flume facility, where a (smooth) rigid test wall was impacted by a single breaking wave generated using a wave-focusing technique (Lafeber et al., 2012b). Impact pressures were recorded by 8 vertically-positioned pressure sensors, and the impacts themselves via side-mounted high-speed cameras.

Changing the focus of the generated wave packs enabled Lafeber et al. (2012b) to selectively vary the characteristics of the wave at the point of impact with the wall. Thus, three wave impact types were identified (see Figure 10) and related to the following 3 ELPs (see also: Table 2):

- **Direct impact ELP** (ELP1) – caused by a wave crest directly impacting the wall;
- **Building jet ELP** (ELP2) – caused by (restricted) wave trough or deflection of the impacting flow after a direct impact on the wall;
- **Pulsating gas pocket ELP** (ELP3) – caused by an entrapped air pocket enclosed either between the impinging wave crest and the wall, or within the crest contact area itself.

Table 2: Three Elementary Loading Processes (ELPs) identified in Lafeber et al. (2012) and the impact types they are assosiated with.

Impact type	ELP1 - Direct impact		ELP2 - Building jet		ELP3 - Pulsating gas pocket	
Slosh impact*	No	Jet prevents direct contact of incoming crest with the wall	Yes	For sharp slosh impacts	No	All
Flip-through	Yes	For small air pocket impacts only	Yes	All	Yes	For cases of small air pockets
Air pocket impact	Yes	All	Yes	For small air pocket impacts	Yes	All

** Restricted trough case*

ELP1 – Direct impact ELP

ELP1 is involved when a direct impact of the water body on the wall is observed e.g. a wave crest impacting the wall directly. The velocity vector of the impinging flow is normal to the wall just before impact, and is quickly reduced to almost nothing in a very short time, dependent on liquid compressibility and the impacted structure elasticity. Therefore, the governing physical phenomenon is the **compressibility of the liquid** (Lafeber, et al., 2012b)**.**

ELP1 appears in close vicinity to the impact point. Once the impact occurs, hemispherical shock waves propagate at the respective speed of sound within the liquid and hemispherical strain waves within the structure, both decreasing quickly with increasing distance away from the source of the impact due to wave energy dissipation (Lafeber, et al., 2012b). The authors also note that ELP1 is always strongly associated with ELP2. This is the case since after the initial contact with the wall, the flow is deflected and the formation of jets in upward/downward direction along the impacted structure are observed.

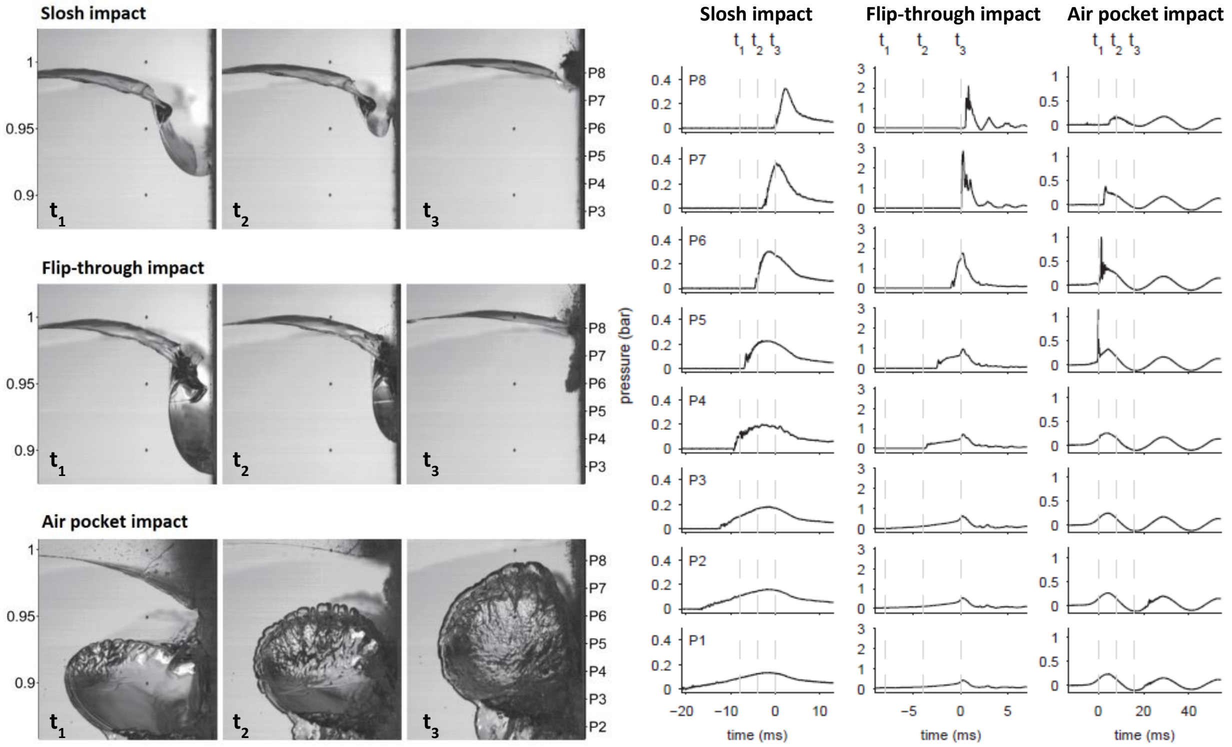

Figure 10: The three impact types identified in Lafeber et al. (2012b) (left) and corresponding pressure signals for the three impact types from all vertically positioned pressure sensors (right).
Adapted from: Lafeber, et al. (2012b), pp. 3-4.

The following parameters govern the impulse loads (Lafeber, et al., 2012b) on the structure:

- Initial impact velocity;
- Incidence of impacting particle with regard to the wall;
- Shape of liquid around the contact point.

The authors observed that the approach phase of the impinging wave, before an impact occurs, also has an effect on the pressure record. This is due to the displacement of the surrounding air by the wave crest, which Lafeber et al. (2012b) suggest causes Kelvin-Helmholtz free surface instability – effectively turning the free surface into spray. This changes the parameters of the impacting water body (impact velocity, incidence of particle, shape of liquid) between test and is theorized to be the main reason for discrepancies for pressure records for repeated tests with identical waves and test conditions (Lafeber, et al., 2012b).

ELP2 – Building jet ELP

ELP2 is present for any impact that causes the building of a jet along the wall. Lafeber et al. (2012b) outlined two main cases when this happens:

- (Restricted) wave trough running up the wall during the wave approach stage;
- Any impact that causes (upward and downward) jets along the wall e.g. after a crest impact (ELP1).

The governing physical phenomenon is the local **change in liquid momentum**, as there is (partial) transfer of the horizontal impinging wave momentum to a vertical momentum along the wall (Lafeber, et al., 2012b). The sharper the (local) change of velocity of the liquid, the higher the pressures exerted on the wall. The authors also note that the building jet can be discerned in the pressure-time signal of individual sensors as it propagates along the wall.

ELP3 – Pulsating gas pocket ELP

ELP3 is observed when an air pocket is caught between the overturning wave crest and the wall, corresponding to entrapment (see Section 2.4.). Furthermore, it appears that this loading mechanism could also be related to any form of gas pocket involved in the impact, namely, entrained air bubbles. The governing physical phenomenon is the **compressibility of gas** (or air) (Lafeber, et al., 2012b). The entrapped air pocket acts like a spring, and the pocket volume oscillates in inverse relation to the internal air pocket pressure (pressure increases for decreasing volume and vice versa).

Lafeber et al. (2012b) observed that the maximum pressure of the air within the pocket and frequency of oscillations both increase for a decrease in total entrapped air volume. In addition, for smaller air pockets higher frequency of oscillations (from the pulsating air pocket) was observed.

This ELP can be identified from the recorded pressure signal, since all pressure sensors positioned within an air pocket are loaded by the entrapped pulsating air volume and show an identical pressure record corresponding to damped oscillations (Lafeber, et al., 2012b). ELP3 is encountered only in combination with other ELPs. Lafeber et al. (2012b) noted that most of the time (but not always) the loads caused by ELP3 itself were smaller when compared to ELP1 and ELP2 (involved in the same impact), however, not insignificant. This is due to the cumulative effect on the wall when one considers the total extent of the affected area, which can be large, hence the global force induced by ELP3 on the wall can be one of the largest.

Later, Section 2.5.3. presents the scaling bias within the context of the three ELPs outlined above (also see: Table 3).

2.5.2. Comparison of ELPs at two scales

Continuing their previous research, Lafeber et al. (2012a) aimed to outline the differences between the three ELPs when observed at two scales. Since these are the building components for every wave-structure impact, the authors argue, it is anticipated that changes in the behaviour of ELPs will cause discrepancies between model and prototype scale tests, thus in the recorded pressure-time signal. Furthermore, if the model scale results are then upscaled by maintaining the Froude number, these will show a scaling bias. Once again, within the context of ELPs, this scaling bias can be predicted quantitatively.

For the purpose, Lafeber et al. (2012a) compared individual impact events based on the same test data outlined in Lafeber et al. (2012b), see Section 2.5.1. Two sets of impacts were selected for the comparison based on their global flow similarity, meaning the propagation of the wave up until the impact occurs. Both of these fall within the *Air pocket*-type impact classification (see Figure 10) since those types of impacts include all three ELPs. Froude similitude was maintained between the two scales at a geometrical length scale $\lambda = 6.14$.

Indeed, the authors found a mismatch in measured pressures between the two scales. They outlined three differences between the small and large scale tests applicable to wave impacting a flat wall. These expand on the findings from Lafeber et al. (2012b) outlined in Section 2.5.1. Furthermore, use of the Bagnold model (Bagnold, 1939) and its applicability to compensate for pressure estimate accuracy at small scale is included.

Spray around the tip of the crest

The flow of displaced gas (air) just before an impact caused a thin film of liquid to form in the 1:6 scale tests, but clouds of water droplets in the 1:1 scale tests. This difference is caused by the lack of scaling of the **surface tension** of the liquid. The balance of inertial and surface tension forces remains the same at all scales, meaning the former remains relatively higher at smaller test scales. This affects the formation of Kelvin-Helmholtz instabilities on the free surface, which in term changes the characteristics of the initial impact with the wall.

Compression of entrapped air (ELP3)

With regard to the pressure inside an entrapped air pocket once an impact has occurred, scaling bias is derived from the lack of compressibility scaling in Froude similitude. The entrapped air pocket acts like a (non-linear) mass-spring system, where the "pushing liquid" is the mass, and the "restoring gas" the spring (Lafeber et al., 2012a). The balance between the two is not equal at model and prototype scales – the mass remains the same at both scales (provided the global flow, hence the initial flow velocity is properly scaled), however, the spring stiffness is not the same (no compressibility of gas scaling included). In other words, the spring is "stiffer" at smaller scales. As a consequence, the frequency of the oscillations is higher. This requires higher forces to accelerate and decelerate the surrounding flow (mass), which leads to the comparatively higher pressures recorded within the bubble at small scales.

The non-linearity of the system is derived from the link between damping and pressure. At smaller scales the (unscaled) pressure is comparatively lower than full scale, affecting the behaviour of the spring. Lafeber et al. (2012a) observed a sinusoidal air bubble pressure signal time trace for model scale tests (Froude upscaled), but sharper crests and flatter troughs of the same trace for prototype scale tests (see Figure 11).

Furthermore, the Bagnold model (Bagnold, 1939) was shown to predict the scaling factor for the peak pressure within the air pocket more accurately (Figure 11). However, the model does not include damping, leading to discrepancies in the time trace of the signal after the initial half period of the oscillation (Lafeber et al., 2012a).

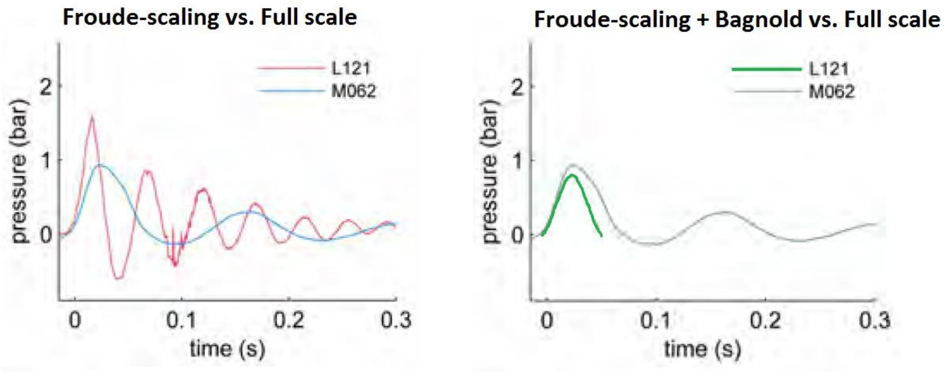

Figure 11: Results from the comparison by Lafeber et al. (2012a) of pressures inside the air pocket at model and full scale. Left: model scale data (test L121; red) is Froude-scaled and compared to full scale results (test M062; blue). Right: model scale data (green) is upscaled and the pressure corrected using Bagnold's model (Bagnold, 1939) and compared to full scale (grey).

Adapted from: Lafeber, et al. (2012a), pp. 11, 13.

It is important to point out that the differences in pressure outlined above are for the pressure **inside** the air pocket, and not the maximum local pressure exerted on the wall, in which the authors noticed a much less significant change. However, Lafeber et al. (2012a) point out that, due to ELP3's significant area of influence, these differences will be important when it comes to the maximum global force exerted on the wall.

Development of building jets (ELP2)

Lafeber et al. (2012a) noted that jets running down from the initial crest impact point were observed only for full scale tests. This was attributed to the internal pressure within the entrapped air pocket, which in smaller scales is relatively higher, influencing the downward jet development and ultimately, the momentum of the liquid (ELP2). High changes in the local pressure signal at the wall were attributed to the ELP2 mechanism, which would lead to differences in the pressure record between scales.

In addition, the Bagnold model does not solve this issue, so a scaling bias will still exist (Lafeber et al., 2012a). As was suggested by Lafeber et al. (2012b), the interaction between ELPs will cause scaling effects even in those loading processes that should otherwise be accurately scaled, such as ELP2 (change of momentum of the liquid). Indeed, this effect was confirmed in the further detailed analysis of individual impacts in Lafeber et al. (2012a).

2.5.3. Froude scaling within the context of ELPs

Outlining the governing physical processes involved in each ELP enabled Lafeber et al. (2012b) to predict where Froude scaling will be unable to accurately replicate ELPs at prototype scale, thus introducing scaling effects. A summary of their conclusions is presented in Table 3.

Table 3: Breakdown of Froude scaling issues for the three ELPs after Lafeber et al. (2012b).

Elementary Loading Process (ELP)	Governing physical mechanism	Included in Froude scaling	Source of a scaling bias
ELP1 **Direct impact**	Compressibility of liquid	No	Yes
ELP2 **Building jet**	Change in momentum (liquid)	Yes	Yes*
ELP3 **Pulsating gas pocket**	Compressibility of gas	No	Yes

** Due to interaction with other ELPs*

This was supplemented in Lafeber et al. (2012a), where direct comparisons of impacts at two scales was conducted. It was observed that the Kelvin-Helmholtz instabilities introduces large variability in the local flow (flow during impact), so Lafeber et al. (2012a) concluded that a quantitative comparison was not possible between the two groups of impact events analysed, however, scaling effects are expected. They instead suggest a statistical approach involving a larger number of tests. Quantitative assessment was performed only for the pressures inside the entrapped air pocket (ELP3), where the authors noted up to 2 times higher upscaled pressures when compared to full scale. However, the total global pressure exerted on the wall showed a much smaller deviation (Lafeber et al., 2012a) and falls more in line with the results of other researchers (e.g. Bullock et al., 2001, 2007). Moreover, while applying the Bagnold model (Bagnold, 1939) allows for more accurate scaling of the maximum pressure inside the air pocket, other features such as the non-linearity of the oscillations could not be replicated.

An important observation in Lafeber et al. (2012a) was how the theoretically Froude-scalable ELP2 (Building jet) also showed scaling bias due to the influence of the entrained gas pocket – a non-scalable ELP. The mechanism of complex ELP interactions amplifying the scaling bias was suggested in Lafeber et al. (2012b), and indeed observed in their further research.

Lastly, Lafeber et al. (2012a, 2012b) outlined additional physical phenomenon that are not expected to Froude-scale, but are also not part of the three ELPs. These are the phase transition of the displaced air by the impinging wave crest, and the elasticity of the impacted structure. The authors later concluded based on the research of Brosset et al. (2011) that structure elasticity does not show evidence of introducing a significant scaling bias (Lafeber et al. ,2012a).

2.5.4. Scaling and air entrainment

Scaling bias directly related to entrained air within the water body was not explicitly investigated by Lafeber et al. (2012a, 2012b). Therefore, this is supplemented in the current section. With regard to air entrainment, Blenkinsopp & Chaplin (2011) noted that compared to an unaerated water flow, an air-water mixture will have increased compressibility and a slightly lower density. Since Froude scaling does not consider compressibility of the fluids, and changes in the water density cannot be reliably accounted for (Bullock, et al., 2001), scaling effects are expected. A further contribution would stem from the observations found in literature of differences in air entrainment at small and large scales.

Blenkinsopp & Chaplin (2007) stated that the total volume of air entrained (air void fraction) scales geometrically between different scales. However, Blenkinsopp & Chaplin (2011) showed that the bubble plume evolution and size distribution remain identical regardles of the model scale. The bubble rise time is dependent on the bubble size, which means that identically sized bubbles at both model and prototype scale will rise at identical rates. Since the model scale is smaller, the bubbles have to travel a shorter distance, which leads to the conclusion that entrained air bubbles will reach the water-air interface quicker. The scaling issue arises from the fact that Froude similitude scales time at $\sqrt{\lambda}$ (see Eq. 2.9.), but the timescale of the bubble rise time should follow (Blenkinsopp & Chaplin, 2007; 2011):

$$t_p = \lambda t_m \tag{2.10.}$$

Bullock et al. (2001) noticed this phenomenon in their comparison of void fractions at different scales. The authors observed that at prototype scale, the ambient void ratio for breaking waves remained higher when compared to scaled laboratory experiments of a similar setup. This was attributed to the bubbles being unable to reach the surface at full scale before the following incoming wave broke (Bullock, et al., 2001), which is often observed in ocean waves as a persistent surface foam (Blenkinsopp & Chaplin, 2011).

Considering that several authors have noted the high aeration (due to air entrainment) of the post-overtopping bore-like flow (e.g. Chen, 2016; Streicher et al., 2016, Van Doorslaer et al., 2017; see Section 2.2.), entrained air induced scale effects regarding the impact forces can reasonably be expected. Comparing between prototype and model Froude-scaled tests, the latter are expected to include less entrained air. As was shown in Section 2.4.1., the so called ‘cushioning effect’ is dependent on the air void ratio. Thus, lower aeration will usually (but not necessarily) lead to less cushioning of the impact pressures at smaller scales (Bullock, et al., 2001), and therefore higher impact force peak pressures, shorter pressure rise times and possibly a reduction in total impulse force.

2.6. Summary

This chapter introduced a number of key concepts based on research covering a broad range of topics. Figure 12 combines the basics key findings in a simplified and concise manner. Further elaboration is also provided below. For more details, please refer to the corresponding sections in this chapter.

The stages of a post-overtopping wave impact with a vertical structure situated on a dike were defined by Chen et al. (2014). Two of these, the *initial impact* and *reflection* stages, correspond to the *dynamic force peak* and *quasi-static force peak* (respectively) for a typical double-peaked force-time signal. The latter of these is usually hydrostatic in nature and linearly distributed vertically along the wall (Chen et al., 2014). If for comparison purposes the flow depth value *h* and force distribution vertically along the wall are assumed constant, any variations in the force exerted on the wall between a small and a large scale test can be attributed to the water density *ρ*. If entrained air is present in the water body, as is often the case for the highly-turbulent post-overtopping flow (Chen, 2016; Streicher et al., 2016), then *ρ* relates to the density of the water-air mixture. Since the processes of air entrainment and detrainment do not scale according to Froude similitude, a difference in total air void fraction, and therefore *ρ*, can be expected, although it is difficult to say whether this will be of significant magnitude (Blenkinsopp & Chaplin, 2011).

On the other hand, the *dynamic force peak*, corresponding to the initial wave-structure impact, can be related to the definitions of elementary loading processes (ELPs) outlined by Lafeber et al. (2012b). Although the model setup for which the three ELPs were defined differs from the post-overtopping flow impacts regarded here, there are notable similarities. Most of all, the *Direct impact* (ELP1) and *Building jet* (ELP2) can be related to the moments of initial impact and subsequent change in momentum of the impinging flow, respectively. The former is again affected by the air void ratio and governed by the compressibility of the aerated flow (Lafeber et al., 2012; Bullock et al., 2007). The *Pulsating gas pocket* (ELP3) can also be observed in cases where interference between the reflected and impinging flow results in wave breaking at the wall and consequently air entrapment. Lafeber et al. (2012a) noted that interactions between ELPs can result in changes in the impact mechanism between models of different scale, so scaling bias affecting the *dynamic force peak* is likely.

The classification of bore impacts proposed by Streicher et al. (2016) can prove useful for distinguishing between cases where scaling bias is related to one of the above phenomena. For *dynamic bore impacts* (dominant *dynamic force peak*) the elementary loading processes and related scaling effects should be considered, whereas for *quasi-static/down-rush bore impacts* (dominant *quasi-static force* peak) scaling effects on the impact forces would likely be limited to the aforementioned possible variance in fluid density.

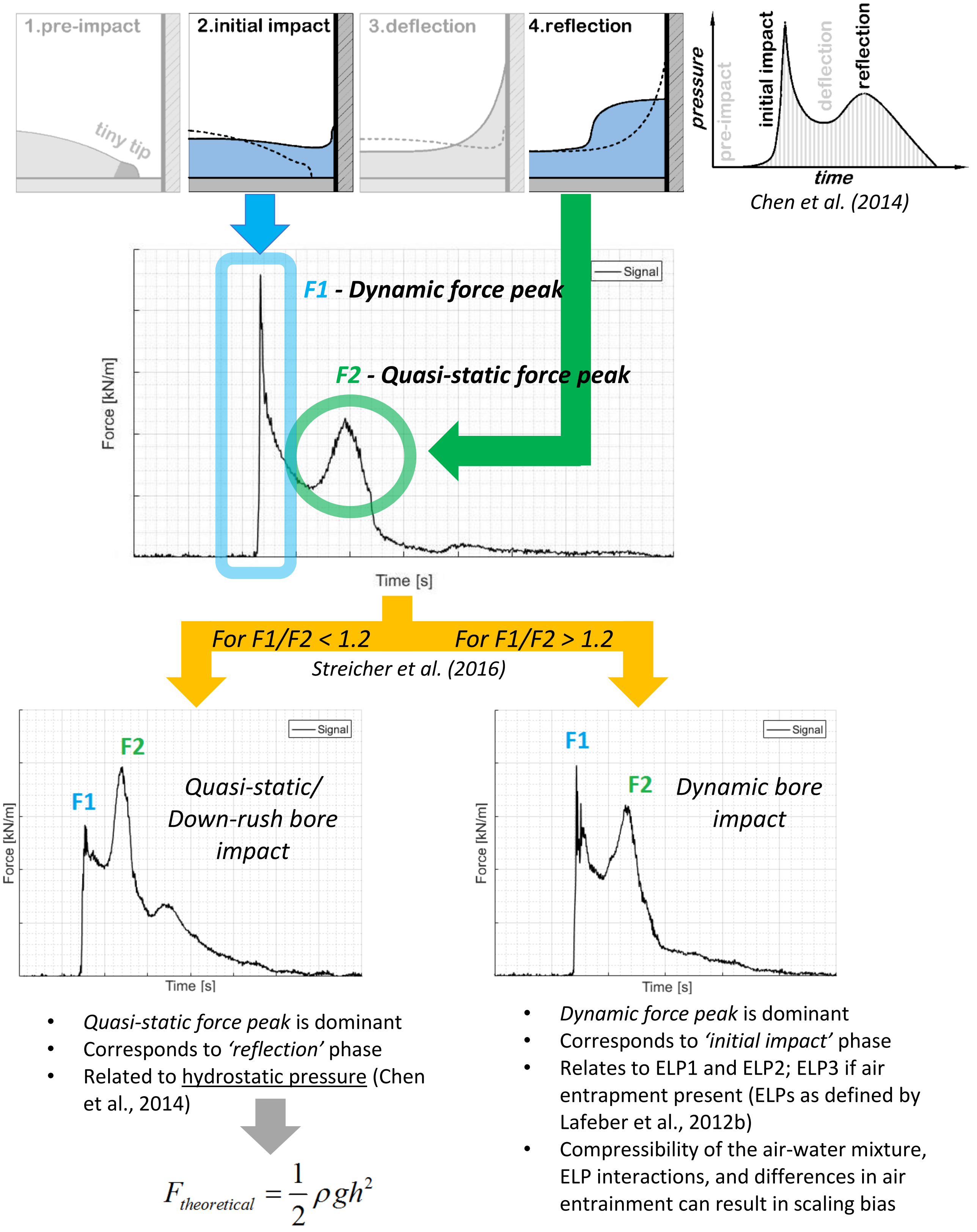

- *Quasi-static force peak* is dominant
- Corresponds to *'reflection'* phase
- Related to hydrostatic pressure (Chen et al., 2014)

$$F_{theoretical} = \frac{1}{2}\rho g h^2$$

- *Dynamic force peak* is dominant
- Corresponds to *'initial impact'* phase
- Relates to ELP1 and ELP2; ELP3 if air entrapment present (ELPs as defined by Lafeber et al., 2012b)
- Compressibility of the air-water mixture, ELP interactions, and differences in air entrainment can result in scaling bias

Figure 12: A summarizing flowchart of key literature review findings with regard to possible scaling effects related to a post-overtopping flow impact with a structure. Dynamic force peak is shown in blue and the quasi-static force peak in green.

3. Methodology

A study of scale effects in hydraulic physical modelling naturally implies a comparison of (at least) two models of similar setup, but in different scale. This chapter aims to introduce the two models for which data was obtained, and how this data was analysed. Focus is kept on the large scale tests conducted in early 2017 at Deltares, Delft, the Netherlands, as part of the WALOWA initiative. These tests also included several measurement approaches that could be considered innovative, at least in the context of the test facility where they were applied. On the other hand, the small scale tests were conducted in 2015 at Ghent University, and are used for comparison purposes due to their similarity to the WALOWA tests. The small scale tests are therefore introduced so as to facilitate the comparison, with emphasis on the similarities (or lack thereof) with the large scale tests.

First, the model (Section 3.1.) and measurement (Section 3.2.) setups for the large scale WALOWA tests are introduced. Similarly, this is briefly outlined for the small scale tests in Section 3.3, followed by a comparison of the two model parameters (Section 3.4.). Lastly, the methodology section (Section 3.5.) covers the approach adopted for data processing and analysis.

3.1. Large scale model setup

Physical modelling tests were conducted in the Delta flume at Deltares (Delft, the Netherlands) in early 2017 as part of the WALOWA project. The test facility provides a maximum available modelling length of 258 m, depth of 9.5 m and a constant 5 m width (Hofland, et al., 2013). The flume is equipped with a hydraulic piston-type wave board (also termed *wave paddle*) capable of generating irregular waves with a maximum significant wave height of H_{m0} = 2.2 m at 6.9 m water depth and an Active Reflection Compensation (ARC) system (Hofland, et al., 2013). The operational still water level (SWL) range is between 2.5 and 8 m.

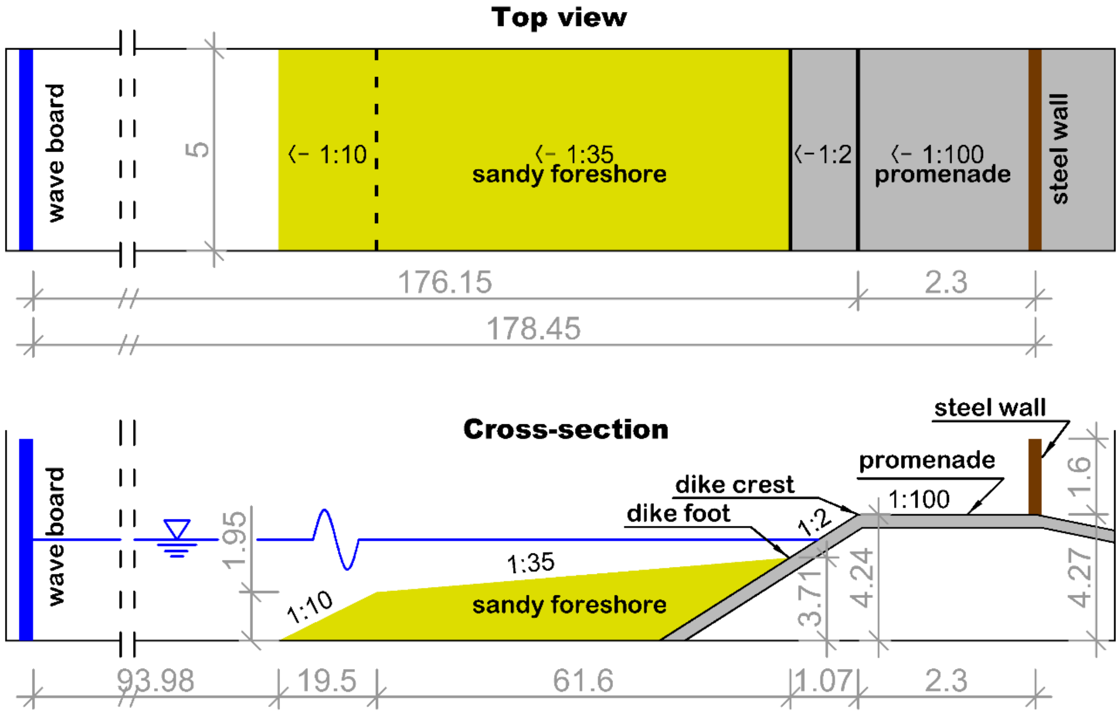

Figure 13: Schematic representation of the physical model setup, dimensions not to scale. The model mimics a typical Belgian coastal profile in scale 1:4.3.

The physical model setup (Figure 13) aimed to represent a typical configuration of the Belgian coastline as described in Section 2.1. The model scale was 1:4.3. (note that Figure 13 is a schematic representation only, and is not to scale.; for a detailed drawing of the model setup, please refer to Appendix 1). The sandy foreshore was replicated with a 1:35 slope, increasing to 1:10 at the offshore extent (closer to the wave board). The top 40 cm of the sand body consisted of sand with a D_{50} = 230 µm. Underneath, a coarser grained sand was used. This imposed a maximum local profile erosion limit of 40 cm, meaning below this threshold sand parameters between tests will remain consistent. The slope profile was flattened manually with a +/- 1 cm threshold for accuracy before the start of the tests. No further reprofiling was needed as the change in profile never exceeded the aforementioned localized erosion depth threshold. The impermeable promenade was constructed out of concrete with a thickness of 8 to 12 cm. The slope of the dike front was 1:2, whereas the top part had a slight offshore incline of 1:100. Care was taken to ensure the concrete was laid consistently flat and that the top surface was smooth and sufficiently uniform.

A 12 mm thick steel wall standing 1.60 m tall at the onshore extent of the promenade replicated the first-line buildings (equally, a storm wall) that an overtopping wave flow would strike. Steel beams were welded to the back of the steel wall to ensure the structure's stiffness and achieve a high natural frequency. The steel wall was mounted vertically and secured to the flume walls. It spanned the whole width of the flume, measuring 4.97 m, with the remaining 1.5 cm gaps on both sides sealed with tape. Several predetermined cut-outs facilitated the implementation of wall-mounted measuring devices, namely pressure sensors, load cells, void fraction meter (VFM), and cameras (see Section 3.2.). A front view schematic representation of the wall is presented in Figure 14 (not to scale).

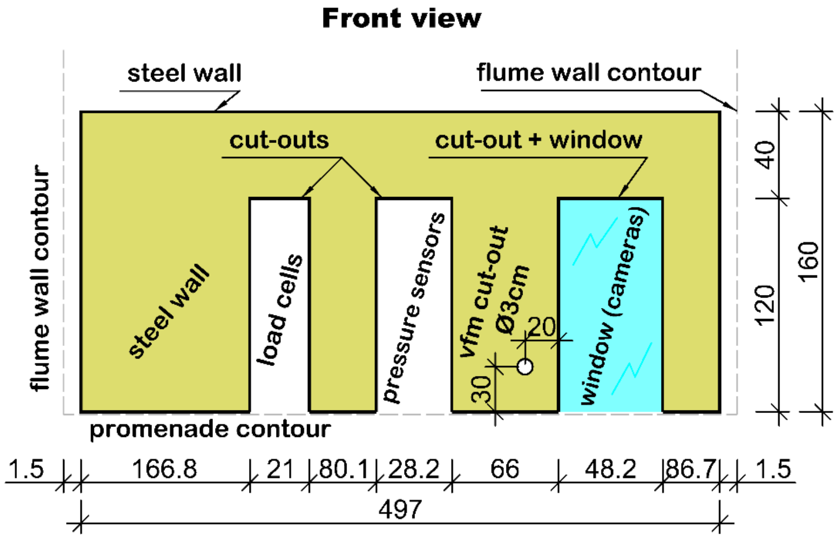

Figure 14: Schematic of the face of the steel wall as viewed from the promenade (viewer's back towards wave the board). Dimensions in cm, figure not to scale. Note the intended purpose of the cut-outs and their position.

3.1.1. Wave conditions

Based on the wave conditions, tests can be subdivided in two categories. Irregular wave tests (denoted 'Irr', see Table 4) were generally longer, with number of waves either 1000 or 3000. A JONSWAP spectrum with a peak enhancement factor γ = 3.3 was used as input for the wave generation. The significant wave height and peak wave period at the wave board varied in the range H_s = 0.49 to 1.06 m and T_p = 4.1 to 6.21 s, respectively (values at model scale). Water depth at the wave paddle covered a range h_{paddle} = 3.77 to 4.13 m, and h_{toe} = 0.06 to 0.42 m at the dike toe (denoted 'dike foot' in Figure 13). For several tests the generated waves matched exactly the wave parameters used in the small scale tests (see also: Streicher et al., 2016) upscaled using Froude similitude with a scaling factor λ = 25/4.3 = 5.81 (Table 4). Apart from test WLW_Irr_2_S, first order wave generation was used.

The second test category used bichromatic waves (denoted 'Bi', see Table 4) and were of much shorter duration, with roughly 18 waves each. Water depths were similar to the Irregular wave tests, ranging from h_{paddle} = 3.76 to 4.14 m and h_{toe} = 0.05 to 0.43 m at the wave paddle and dike toe, respectively.

In total, 22 tests were conducted, of which 11 with irregular waves (9 original tests and two repeats) and 11 with Bichromatic waves (9 original tests and two repeats). A summary of all test names and respective parameters is presented in Table 4.

Table 4: Summary of the 22 tests conducted under the WALOWA initiative. All parameters are in model scale (1:4.3).

Test name	**Date**	**Nr. of waves**	**Depth at wave paddle**	**Depth at dike toe**	**Dike crest freeboard**	**Significant wave height**	**Peak period/ frequency**	**Test length****
		N [-]	h_{paddle} [m]	h_{toe} [m]	R_0 [m]	H_s [m]	T_p [m] f [Hz]	[s]
Bi_01_4	20-Mar	~18	3.99	0.28	0.25	a_1 = 0.5; a_2 = 0.4	f_1 = 0.174; f_2 = 0.142	270
Bi_01_5	20-Mar	~18	4.00	0.29	0.24	a_1 = 0.5; a_2 = 0.45	f_1 = 0.174; f_2 = 0.142	199
Bi_01_6	21-Mar	~18	4.01	0.30	0.23	a_1 = 0.5; a_2 = 0.5	f_1 = 0.174; f_2 = 0.142	222

Bi_02_4	21-Mar	~18	4.13	0.42	0.11	a_1 = 0.45; a_2 = 0.36	f_1 = 0.19; f_2 = 0.155	216
WLW_Irr_1_F*	22-Mar	1000	3.99	0.28	0.25	1.05	6.21	6569
WLW_Irr_2_F*	23-Mar	3000	4.00	0.29	0.24	0.92	5.85	16069
WLW_Irr_2_S	27-Mar	3000	3.99	0.28	0.25	0.92	5.85	16083
WLW_Irr_3_F	28-Mar	3000	4.12	0.41	0.12	0.92	5.85	16062
Bi_02_5	29-Mar	~18	4.14	0.43	0.10	a_1 = 0.5; a_2 = 0.4	f_1 = 0.19; f_2 = 0.155	207
Bi_02_6	29-Mar	~18	4.14	0.43	0.10	a_1 = 0.5; a_2 = 0.4	f_1 = 0.19; f_2 = 0.155	209
Bi_02_6_r	29-Mar	~18	4.14	0.43	0.10	a_1 = 0.5; a_2 = 0.4	f_1 = 0.19; f_2 = 0.155	206
WLW_Irr_8_F	29-Mar	1000	4.13	0.42	0.11	0.49	4.10	3961
WLW_Irr_4_F*	30-Mar	1000	3.79	0.08	0.45	0.87	5.69	5998
WLW_Irr_5_F*	30-Mar	1000	3.78	0.07	0.46	1.05	6.21	6520
WLW_Irr_1_F_r	31-Mar	1000	4.01	0.30	0.23	1.06	6.21	6415
WLW_Irr_7_F*	31-Mar	1000	4.00	0.29	0.24	0.65	5.00	5379
WLW_Irr_2_F_r	03-Apr	3000	4.01	0.30	0.23	0.92	5.85	16098
Bi_01_6_r	03-Apr	~18	4.01	0.30	0.23	a_1 = 0.5; a_2 = 0.4	f_1 = 0.174; f_2 = 0.142	198
Bi_03_6	04-Apr	~18	3.77	0.06	0.47	a_1 = 0.5; a_2 = 0.4	f_1 = 0.174; f_2 = 0.142	337
Bi_03_6_1	04-Apr	~18	3.77	0.06	0.47	a_1 = 0.5; a_2 = 0.4	f_1 = 0.174; f_2 = 0.142	351
Bi_03_6_2	04-Apr	~18	3.76	0.05	0.48	a_1 = 0.5; a_2 = 0.4	f_1 = 0.158; f_2 = 0.129	331
WLW_Irr_6_F*	04-Apr	1000	3.77	0.06	0.47	0.65	5.12	5124

** Tests matching wave conditions in Streicher et al. (2016)*

*** Test duration here defined by the length of the recording of the main data acquisition system*

Key:

Irr - Irregular waves
Bi - bichromatic waves
F - first order waves
S - second order waves
r - repeated test

3.1.2. Reference systems

Due to the large size of the Delta flume, two Cartesian reference systems were defined. The *Global Coordinate System* (GCS) matched the one typically used in the flume facility, beginning at the lower right (northern) corner of the wave paddle when looking towards the model (see Figure 15). Coordinates in the GCS reference system were denoted with capital letters (X, Y, Z). The orientation of the arrows in Figure 15 represent the positive direction of each coordinate.

The *Local Coordinate System* (LCS) originates at the dike crest on the northern wall (Figure 15). The GCS coordinates of the origin point are X = 176.15 m, Y = 0 m, Z = 4.24 m (Streicher, 2017). LCS coordinates are denoted with lowercase letters (x, y, z). The arrows in Figure 15 denote positive direction.

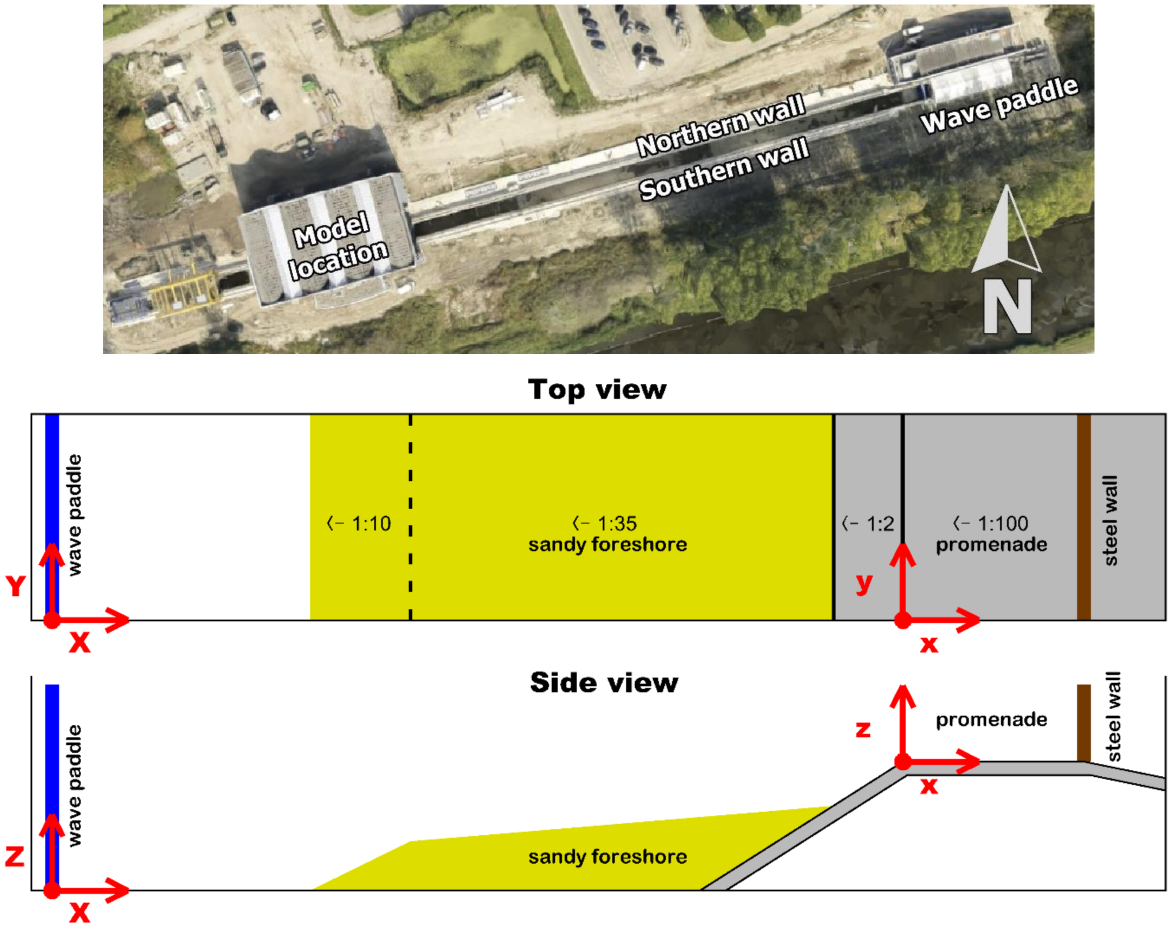

Figure 15: Origin of GCS and LCS. Direction of arrows indicates positive direction. Top: Top view image of the Deltares Delta flume with northing (image source: Google Maps). Middle: Schematic representation of the fume and model – top view (not to scale). Bottom: Schematic representation of the flume and model – side view (not to scale).

Image source (top): Google Maps; Map data ©2017 Google
https://www.google.com/maps/@51.984017,4.3824558,179m/data=!3m1!1e3

3.2. Measurement setup – large scale tests

A wide range of measurement sensors and devices were used in the WALOWA tests. For the purpose of this thesis, emphasis will be kept on the measuring equipment which was either put under the author's control (laser scanner, optical phase detection probe, high-speed and supplementary cameras), or was integral for the research topic explored (load cells and pressure sensors). An extensive list of all measurement equipment used in the WALOWA tests can be found in Appendix 3.

3.2.1. Laser scanner

For non-intrusive measurements of the instantaneous water surface during the tests, a 2D Terrestrial Laser Scanner (TLS) was used. Decisions on the mounting position and operational settings were trusted to the author, so these are covered in detail in this section. Following the recommendations of Streicher (2013) and Streicher et al. (2013), the SICK LMS511 PRO HR was implemented (see Figure 16). For brevity, this device will also simply be termed *laser scanner*, or *LS* hereafter. The SICK LMS5xx family implements the Time of Flight (ToF) principle, using the time between emitting and receiving a reflected pulsed laser beam to estimate distance to the target object (SICK, 2011) (Streicher, 2013). Each reflected pulse picked up by the device possesses a Reflected Signal Strength Indicator (RSSI) value, a measure of the power received by the sensor, and falls within the range 0-255 (SICK, 2011) – see Table 5.

Figure 16: Laser scanner used in the physical modelling tests. Manufacturer: SICK. Model family: LMS5xx. Image source: SICK (2011, p. 1)

Table 5: Description of RSSI values recorded by SICK LMS5xx laser scanner devices. Adapted from: SICK (2011, p. 37)

RSSI value	Description	Further notes
0	No signal	0 value assigned to measurements where distance could not be measured (target out of range or very low remission; signal power too low)
1 to 254	Valid measurement	1 - weakest possible signal; 254 - strongest possible signal (e.g. white paper scanned at close range)
255	Dazzled	-

The device was mounted via a wooden frame directly on the left wall of the flume (when looking towards the steel wall) with GCS coordinates X = 175.64 m, Y = 4.78 m and Z = 8.99 m (see Figure 17). The laser scanner was tilted with a slant angle $\phi = 23.21^o$. This prevents the dazzling of the device by direct reflection at nadir (Streicher, 2013; Hofland et al., 2015), which has been previously observed to yield erroneous measurements (Blenkinsopp, et al., 2012). Furthermore, the slant angle falls between the minimum recommendations of 5^o to 15^o (Allis et al., 2011; Streicher et al., 2013; Valentini et al., 2014), and the 26^o that Hofland et al. (2015) used in their setup. The slant angle also enabled the device to have a clean view of the profile to-be scanned, negating any obstructions presented by e.g. other equipment mounted on the promenade.

In choosing the mounting height, several aspects had to be considered:

- The scanned profile had to fall within a suitable crosswise position with regard to the width of the promenade, avoiding e.g. scanning too close to the wall (avoiding wall-induced flow effects) or part of the beam falling on the window on the steel wall (could yield inaccurate measurements (SICK, 2011));
- Had to enable the implementation of a sufficient slant angle (Streicher, et al., 2013);
- Had to negate obstructions such as wooden frame with gauges on promenade;
- Should not be too high as to yield unreliable measurements due to low received signal strength indicator (RSSI) values;
- Had to avoid high incidence angles of the laser beam with the scanned surface (see Figure 18). Also a function of the lengthwise position (x-axis).

Streicher, et al. (2013), Streicher (2013), Valentini et al. (2014), Diamantidou (2014) and Hofland, et al. (2015) provided guidance with regard to the mounting height and expected maximum field of view (FoV) relation. However, the unique setup of the present tests, namely the complicated profile being scanned - combination of various surface types (water, concrete, steel) at changing inclines with regard to the laser beam (see Figure 18), meant that no single previous publication provided robust enough guidelines. Furthermore, several studies also include controlled turbidity of the water through seeding techniques (e.g. Diamantidou, 2014; Valentini et al., 2014), which was not the case in the present tests. Blenkinsopp (2012) suggests 40 NTU as the lower limit for water turbidity for obtaining good reflections, and it was anticipated that this would be met due to the high turbulence of the flow on both the foreshore and the promenade, and resultant sediment entrainment by breaking waves on the foreshore. The turbulent nature of the flow also produces surface foam, which affects the surface roughness and increases RSSI values (Streicher et al., 2013; Valentini et al., 2014).

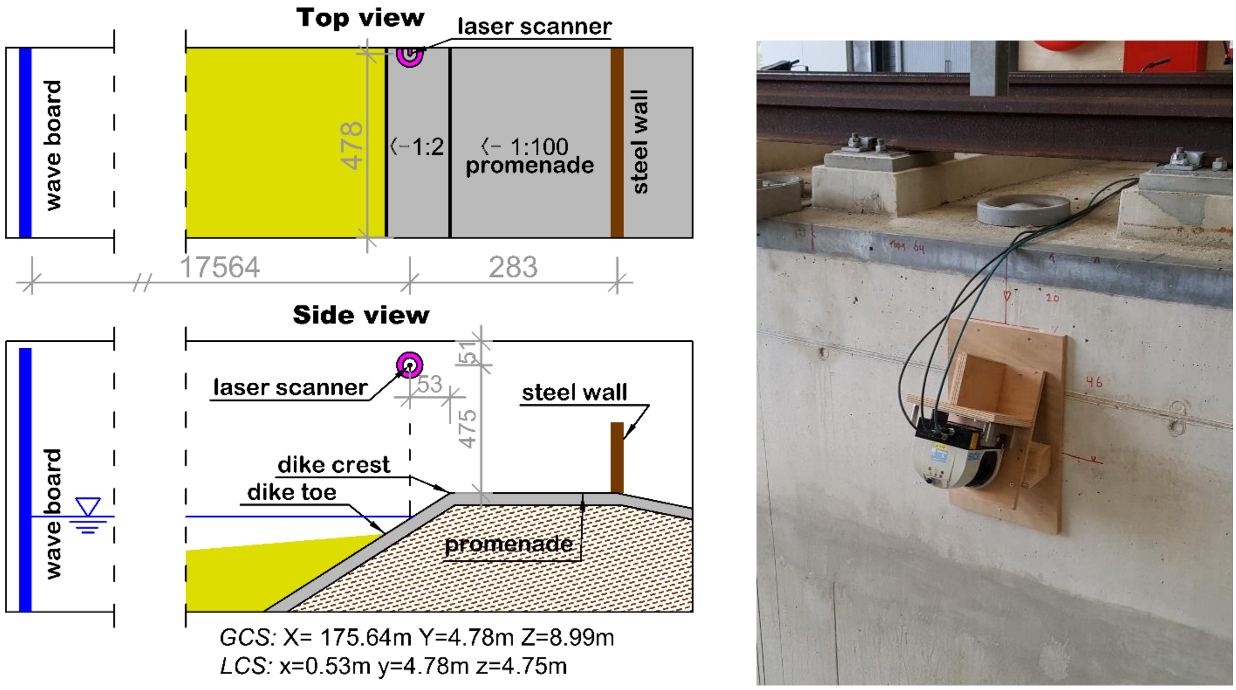

Figure 17: Left: position of laser scanner (magenta) as installed. Dimensions in cm, figure not to scale. Right: picture of the laser scanner as installed on the flume wall. Note how the wooden mount provides an inclined scanning plane (slant angle φ=23.21°).

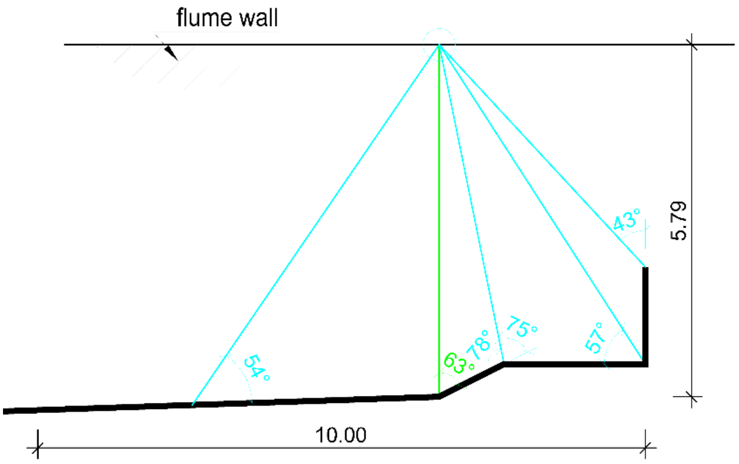

Figure 18: Schematic representation of changes in the incidence angle of the laser beam due to the relatively complex profile being scanned. Black line schematically represents the profile of the foreshore, promenade and steel wall. Note that this is for a dry profile case (no water present). Laser scanner position approximated (not as mounted).

Further details regarding the mounting position of the laser scanner can be found in Appendix 4, where detailed drawings of the mounting position, position of scanned profile and wooden mount dimensions can be found.

Scan data was recorded using the SOPAS ET software (version 2.38) available from the manufacturer. The software saves the recording as binary data files (.*data* file extension), but also provides the option to export a recording as comma separated value (CSV) files. The latter were used for data analysis purposes (see Section 3.5.). Synchronisation with the other instruments was achieved by wiring the laser scanner to receive the same electrical synchronisation pulse at the start of every test. The sync pulse is found in a separate column in the exported CSV file.

The Pro model of the laser scanner allows a variety of sampling frequency and resolution options (see Table 6). For all tests, these were set to 35 Hz and 0.25°, respectively, which allowed for a reasonable trade-off between sampling rate and resolution. Furthermore, the angular resolution, or distance between individual scanned points, is a function of the distance the laser beam has to travel. Averaged over the entire promenade with no water present, this was estimated to be 2.55 cm.

Table 6: Possible scanning frequency and angular resolution combinations for SICK LMS511 PRO laser scanner. Blue rectangle identifies the values used in the tests.

Adapted from: SICK (2011, p. 32)

Scanning frequency	25 Hz	25 Hz	35 Hz	35 Hz	50 Hz	50 Hz	75 Hz	75 Hz	100 Hz	100 Hz
Angular resolution	0.1667 °	0.25 °	0.25 °	0.50 °	0.33 °	0.50 °	0.50 °	1 °	0.667 °	1 °

The maximum field of view of the laser scanner is 190° (SICK, 2011). However, this exceeds the range of points that were of interest. Although it is possible to discard these in the post-processing stage, the unnecessary recorded data affects the size of the recorded files. Considering the significant length of some of the tests, a decision was made to limit the recorded FoV through the SOPAS software to 114°, starting at 18° (offshore extent) and stopping at 132° (just beyond steel wall) – see Figure 19. This FoV equates to a theoretical maximum scan distance of about 21.3 m excluding the presence of water. In theory, if the surface reflectivity is sufficient this setup allows for capturing part of the wave transformation process over the foreshore, the wave overtopping over the promenade, and the run-up characteristics at the wall. A test recording with no water present was initiated once the device was mounted on the wall and showed overall encouraging results with regard to RSSI values.

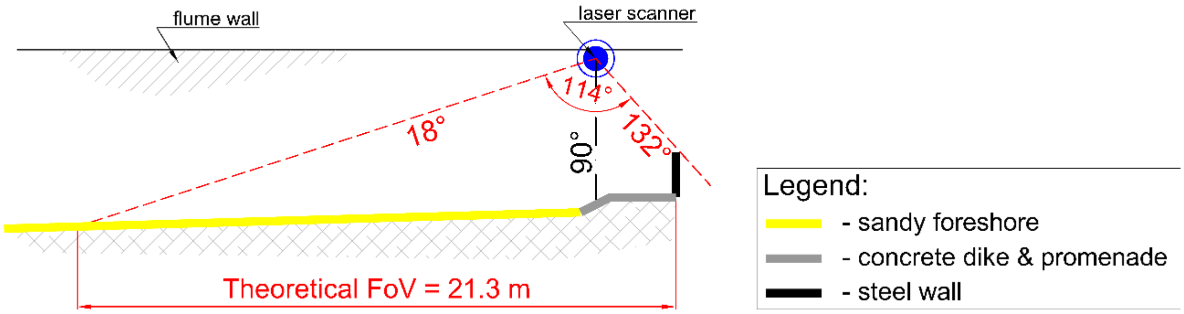

Figure 19: Field of view chosen for laser scanner recordings. Offshore extent at 18°. Steel wall at 132°. The blue dot represents the laser scanner position. The theoretical FoV excludes the presence of water.

SOPAS enables the user to select various filtering, recording and sensitivity options (SICK, 2011). As suggested by Streicher (2013), the *fog filter* was not implemented. The same was true for the *particle filter*. Furthermore, the Pro version of the device allows for up to 5 reflected pulses (echoes) to be recorded. *First echo* was used throughout all tests. A test recording with *all* echoes did not appear to provide any benefit to the quality of the recorded data, and would have further increased the recorded file sizes.

A summary of the device specifications and settings applied for the laser scanner recordings throughout all tests is presented in Table 7. The device specification sheet can be found in Appendix 5.

Table 7: SICK LMS511-Pro HR specifications and setup during recordings for all tests.

Specifications adapted from: SICK (2011, pp. 101-102)

Sampling frequency				**35 Hz**
Angular resolution				0.25°
Field of view (FoV)				114°
Average distance between individual scan points on the promenade (no water)				2.5 cm
Theoretical maximum scan distance (along x-axis, no water)				23.1 m
Device position				
	GCS		**LCS**	
	X	175.64 m	**x**	0.53 m
	Y	4.78 m	**y**	4.78 m
	Z	8.99 m	**z**	4.75 m
Slant angle ϕ				23.21°
Beam diameter at front screen				13.6 mm
Beam divergence				4.7 mrad
Beam diameter at 18m scanning range				99 mm
Systematic error (at 10% object remission)				
1 to 10 m				+/- 25 mm
10 to 20 m				+/- 35 mm
Statistical error (1σ; at 10% object remission)				
1 to 10 m				+/- 7 mm
10 to 20 m				+/- 9 mm

3.2.2. High speed camera

The clear Plexiglas window flush mounted with the steel wall (see Section 3.1. Figure 14) facilitated the implementation of cameras to record the impinging overtopping and run-up flow from behind the wall. An IO Industries Flare 2M280CCX high-speed camera (also termed simply *camera*, *high-speed* or *HS camera*, for brevity) was mounted on a tripod behind the window (Figure 20) and served as the primary recording unit. A secondary camera was also used in several tests, see Section 3.2.6. (*window* camera).

Figure 20: The high-speed camera as mounted behind the promenade wall (left) and approximate view of the camera (right). Camera in protective case.

Source (image - right): Streicher (2017, p. 11)

The HS camera was coupled with a 12.5mm Fujinon HF12.5SA-1 fixed focal length lens with a maximum aperture of f/1.4. Both were placed in a protective enclosure to prevent damage to the equipment. Data was sent from the camera to an external recorder (IO Industries DVR Express Core CORECXP3IO) controlled by a standalone computer, and the recordings were done using the manufacturer's CoreView software.

The high-speed camera was positioned at X = 179.339 m, Y = 1.115 m, Z = 4.628 m (GCS), measured from the camera sensor. The distance from the camera sensor to the outer surface of the window was 85.05 cm. The recording framerate for all tests was set at 100 frames per second (fps) at a resolution of 1248 px horizontally by 1088 px vertically. It should be noted that the position of the recorded frame was slightly offset from the sensor's central axis as shown in Figure 21. Exposure was controlled by varying the shutter speed. The aperture of the lens was set to f/1.4 for all but three tests, when it was reduced to f/2.8 (see Table 8 for summary of specifications and applied settings).

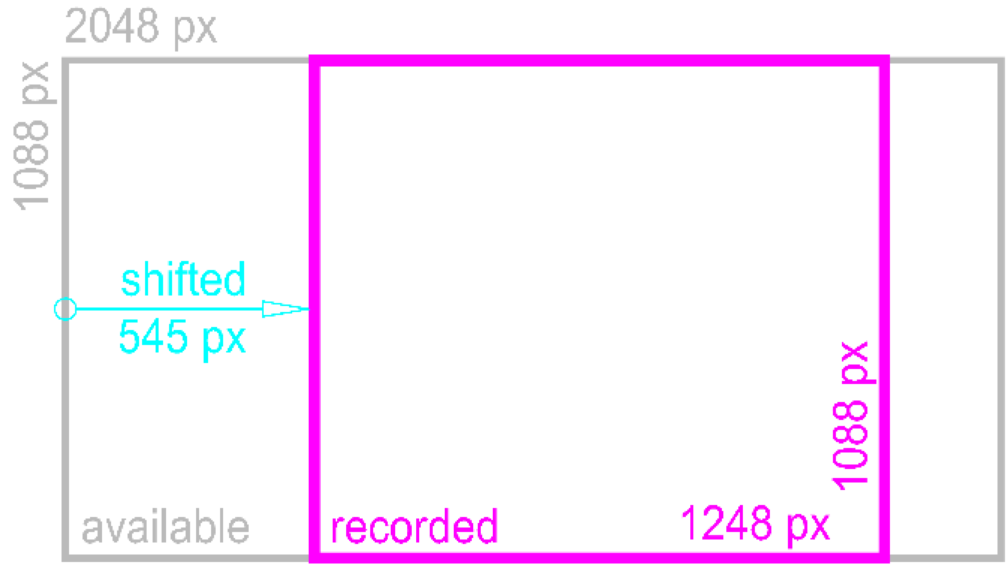

Figure 21: Available frame size (grey), recorded frame size (magenta) and offset (cyan).

Synchronization was achieved using a red LED light positioned within the FoV of the camera. The LED was wired to light up when it receives the same synchronization pulse used by all other devices. The lighting setup involved a LED light positioned vertically behind the window (visible in Figure 20 – left). To avoid glare, the light was offset by approximately 45 cm to the side of the camera, and a makeshift diffuser was implemented. A second LED light source was tested, positioned on top of the steel wall right above the window and aiming downwards. However, the amount of light penetrating the run-up flow varied significantly within a single impact event, which meant that correct exposure could not be reliably acquired. Therefore, this light source was only used for the tests during day 1 (see Appendix 2).

The high data output of the high-speed camera necessitated a reduction in total recording time due to storage constraints. For each test, the camera was started just before the synchronization LED, thus on average only the first 20 minutes of each test were recorded. An exception were the considerably shorter bichromatic wave tests, where the camera was recording for the complete length of each test. The recorded data was exported as JPEG files (.jpg), meaning each file represents a single video frame.

For the installation setup outlined above, the resolution obtained was estimated to be 0.33 mm per pixel.

A summary of the high-speed camera specifications, setup and settings is presented in Table 8. Specification sheets for the camera body and lens can be found in Appendices 6 and 7.

Table 8: High speed camera, lens and DVR specifications and setup during recordings for all tests.
Specifications adapted from: IO Industries (2011, p. 7); IO Industries (2016, p. 5); Fujifilm Corporation (2016, p. 10)

Sensor size	2048 x 1088 px; 12.7 mm diagonal
Sensor type	CMOS, colour
Shutter	Global electronic shutter
Pixel size	5.5 x 5.5 µm
Resolution set for recordings	
Horizontal	1248 px
Vertical	1088 px
Frames per second	100 fps
Shutter speed	varied
Aperture	f/1.4*
Focal length	12.5 mm
Minimum focus distance	10 cm
Back focal distance in air	16.07 mm
Focus	Manual
White balance	Auto
Exposure	Manual; Controlling shutter speed
Connection DVR to computer	eSATA, 3 Gbps

** f/2.8 used for tests: Bi_02_5; Bi_02_6; Bi_02_6_r*

3.2.3. Pressure sensors

To measure the pressures on the wall caused by the impinging overtopping flow, 15 Kulite HKM-379 (M) pressure sensors were installed, capable of recording a maximum pressure of 1 bar. The pressure sensors were installed vertically in 13 rows, with 3 sensors at row 5, see Figure 22. The coordinates of all sensors can be seen in Table 9. The first sensor was positioned 2 cm vertically from the promenade surface. Data was recorded by the main recording system and sampled at 1000 Hz. Synchronization was done by recording a synchronization pulse received by all devices at the start of each test. The pressure sensors were linearly calibrated, with the range 0-10 Volts corresponding to 0-1 bar (Streicher, 2017). A specification sheet can be found in Appendix 8.

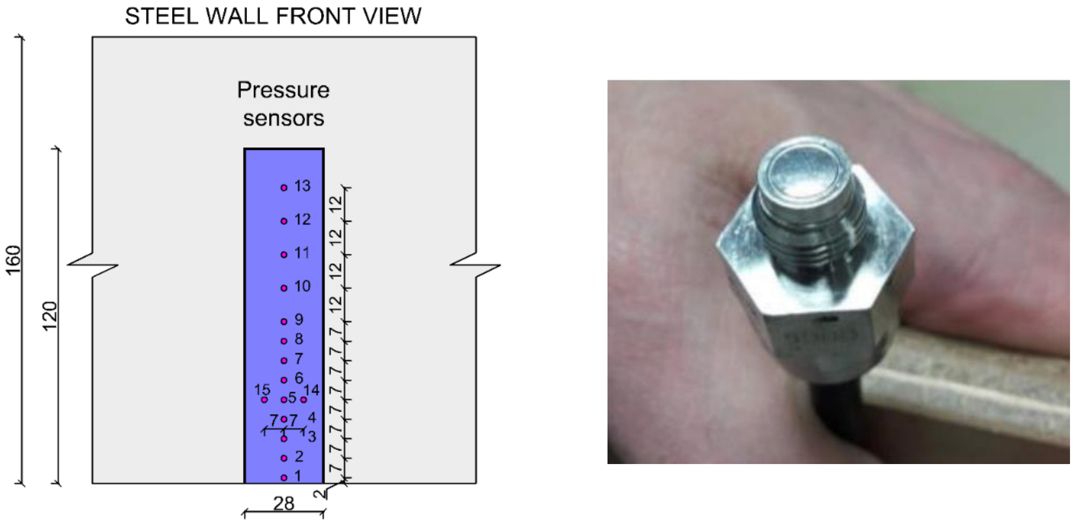

Figure 22: Left: Front view of a section of the steel wall showing the numbering and position of the pressure sensors (magenta). Right: A single Kulite HKM-379 (M) pressure sensors unit.
Source (image - right): Streicher (2017, p. 8)

Table 9: Location of the 15 pressure sensors in global (GCS) and local (LCS) coordinates.

Pressure sensor	GCS [m]			LCS [m]		
	X	Y	Z	x	y	z
1	178.488	2.165	4.287	2.325	2.165	0.043
2	178.488	2.165	4.357	2.325	2.165	0.113
3	178.488	2.165	4.427	2.325	2.165	0.183
4	178.488	2.165	4.497	2.325	2.165	0.253
5	178.488	2.165	4.567	2.325	2.165	0.323
6	178.488	2.165	4.637	2.325	2.165	0.393
7	178.488	2.165	4.707	2.325	2.165	0.463
8	178.488	2.165	4.777	2.325	2.165	0.533
9	178.488	2.165	4.847	2.325	2.165	0.603
10	178.488	2.165	4.967	2.325	2.165	0.723
11	178.488	2.165	5.087	2.325	2.165	0.843
12	178.488	2.165	5.207	2.325	2.165	0.963
13	178.488	2.165	5.327	2.325	2.165	1.083
14	178.488	2.095	4.567	2.325	2.095	0.323
15	178.488	2.236	4.567	2.325	2.236	0.323

3.2.4. Load cells

Another measurement of the loads on the wall was conducted using two HBM U9 compression load cells (Figure 23). These sensors were installed between a hollow steel profile and the rigid support structure at the back of the wall. The hollow steel profile was hung in a manner which provided free movement, but restricted rotation (Streicher, 2017). Furthermore, it was flush mounted with the front of the wall, leaving small gaps on all sides sealed with tape. The load cells had an applicable range of up to 20 kN. The data was recorded by the main recording system and the sampling frequency was 1000 Hz. Synchronization was achieved using the same synchronization pulse that is received by all devices at the start of each test. The load cell coordinates are given in Table 10, and a specification sheet can be found in Appendix 9.

Calibration was performed, with reported total error < 10 N and noise levels around 50 N (Streicher, 2017).

Figure 23: Left: HBM U9 compression load cell. Centre: hollow steel profile and gap in steel wall to accommodate it. Bottom: hollow profile installed, as viewed from behind the steel wall.

Adapted from: Streicher (2017, p. 8)

Table 10: Location of the two load cells in global (GCS) and local (LCS) coordinates.

	GCS [m]			LCS [m]		
	X	**Y**	**Z**	**x**	**y**	**z**
Lower load cell	178.50	3.21	4.45	2.325	3.21	0.18
Upper load cell	178.50	3.21	5.42	2.325	3.21	1.15

3.2.5. Optical phase detection probe

The original WALOWA measurement setup included an optical phase detection probe (OPDP; also termed *void fraction meter* or *VFM* for brevity) to be installed through a predetermined circular opening in the steel wall (as shown in Figure 14). However, close to the start of the test campaign it was determined that the OPDP intended for this purpose was not operational. A replacement OPDP had to be sourced, which mean that this device was operational for tests conducted only after day 7 (see Appendix 2). This was also the main reasoning behind installing the high-speed camera behind the window (Section 3.2.2.).

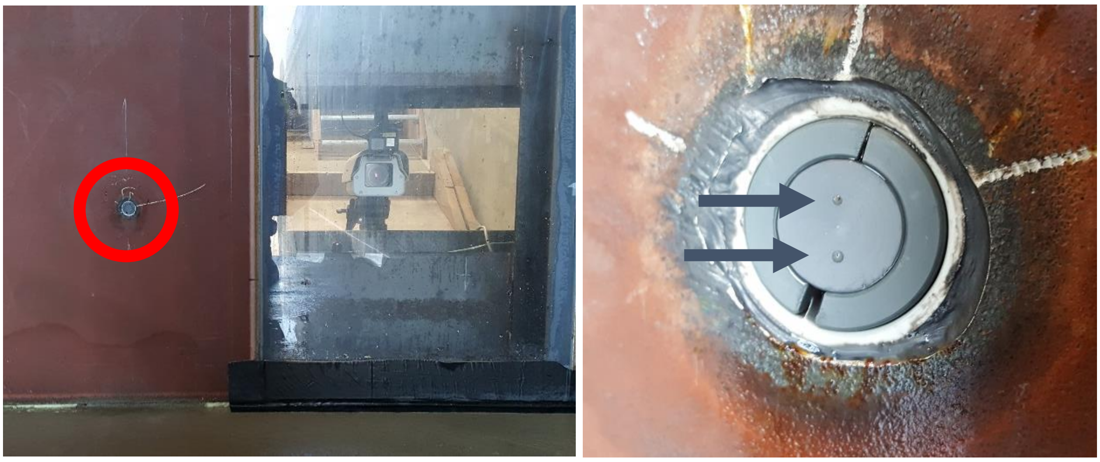

Figure 24: Void fraction meter (circled in red) as seen from the promenade (left). Optical fibres (grey arrows) mounted vertically above each other.

The new OPDP (Figure 24) was positioned in the predrilled opening in the steel wall at the following GCS coordinates: X=178.50 m; Y=1.57 m; Z=4.58 m. It consisted of two optical fibres mounted vertically above each other at a distance of 5 mm (Figure 25). Each fibre had a diameter of 0.25 mm and protruded 1 mm from the mount. Although technically an intrusive measurement technique, the obstruction to the flow presented by the small optical fibres is insignificant, and can be disregarded with a high degree of confidence (Ryu & Chang, 2008).

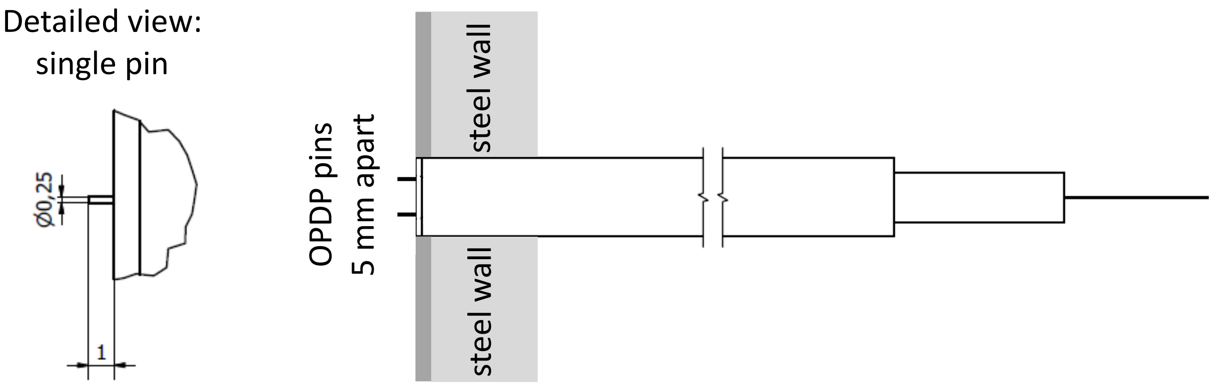

Figure 25: Cross-section of the two optical fibre pins and their housing as installed in the steel wall. Dimensions in mm.

Care was taken when installing the optical fibre's plastic housing, ensuring flush mounting with the wall surface. The device was set to output at 10 000 Hz to an external computer. Synchronization once again was achieved by receiving the global sync pulse sent to all devices at the start of each test. An OPDP allows for detection of air bubbles in the flow. A recorder detects the difference in reflected light within the fibre when a pin's surrounding medium changes (water to air and vice versa). This is recorded as changes from 0 Volts (air) to approximately 5 Volts (water). Using two channels (two pins recording separately) and the knowing the distance between them allows for estimation of the bubble velocity and size (Eikelboom, 2016) during a wave impact. Although initially there were concerns over the pins getting damaged by severe wave impacts or entrained sand particles, the presented setup proved to be robust. Unfortunately, the void fraction data was not available for the test selected for analysis (see Section 3.4.).

3.2.6. Additional cameras

Three GoPro Hero 5 Black cameras (Figure 26 - left) were deployed during the tests to provide visual reference and supplementary data for analysis and redundancy. The coordinates and purpose of each camera can be found in Table 11, and their mounting positions in Figure 27. For brevity, these cameras are hereafter termed *overview* (or OV), *side view* (or SV) and *window* (W) – as indicated in Figure 27.

Figure 26: Three GoPro cameras were used during the tests (pictured on the left). Manufacturer: GoPro. Model: CHDHX-501 'Hero 5 Black'. These were simultaneously controlled using a wireless remote (pictured on the right). Manufacturer: GoPro. Model: 'Smart Remote' ARMTE-002.

Image source: Manufacturer website
Source links: *https://shop.gopro.com/accessories-2/the-frame-hero5-black/AAFRM-001.html (left)*
https://shop.gopro.com/EMEA/accessories-2/smart-remote/ARMTE-002.html (right)

Throughout the tests, all three cameras recorded 2.7k resolution footage at 60 fps at a bitrate of 60 Mbps (see Table 12 for a complete list of settings). The footage was saved onto 128 GB SD cards installed in the cameras. Offloading the files was done after a test had finished through the cameras' USB interface. The same cable supplied power during operation, using two separate portable power banks for SV and W cameras, and a USB power supply adapter for the OV camera. In order to simultaneously start and stop recording for all cameras, a wireless GoPro ARMTE-002 '*Smart Remote*' was used (Figure 26- right).

For synchronization purposes, three red LED lights were positioned within the frame of each camera. These were wired to light up with the initiation of the synchronization pulse at the beginning of each test. The window and high speed cameras utilized the same LED.

The lighting setup consisted of a 200 W LED floodlight mounted right above the overview camera (visible in Figure 27– right), and a more focused LED light source mounted on the side wall, just above the side view camera. The lighting setup for the window camera is identical to the one presented in Section 3.2.2. for the high-speed camera.

Figure 27: Mounting positions of GoPro cameras. Left: an image from the overview camera (OV) showing the promenade. Cameras marked in red. W denotes window camera (hidden behind the wall), SV – side view camera, and OV – overview camera. Centre: window camera as seen from behind the wall. Right: the overview (OV) camera was mounted on a frame, which was suspended on the so called 'blue carriage' crane.
Adapted from (image-right): Streicher (2017, p. 12)

Table 11: Position, coordinates (GCS) and intended application of the three GoPro cameras.

Camera	**Position**	**Coordinates (GCS)**			**Recorded footage**	**Analysis possibilities**
Overview (OV)	On frame (blue carriage)	X = 172 m*	Y = 2.50 m*	Z = 8 m*	Top view of promenade & steel wall; Overtopping flow over promenade; Crosswise inconsistencies in the flow	Run-up height at steel wall
Side view (SV)	Right wall (when looking at steel wall)	X = 177.26 m	Y = 0.066 m	Z = 5.44 m	Side view of promenade; Overtopping flow and bore-to-bore interactions	Overtopping flow thickness & front velocity
Window (W)	Behind window	X = 179.09 m	Y = 1.12 m	Z = 4.76 m	View through window on steel wall; Flow before/during impact	Bubble size and entrained air void fraction**

** Approximate coordinates, varied between tests*
*** The framerate of the camera might be insufficient for the purpose*

Considering that the video recordings were taken with the possibility for conduct analyses at a later point, it was important to estimate the minimum resolution (distance covered by an individual pixel) for each camera. The theoretical minimum (i.e. lowest) values were estimated as listed below:

- Overview camera – approximately: 5.5 mm/px (on steel wall); 9.5 mm/px (on promenade);
- Side view camera – approximately: 2.78 mm/px (on opposing flume wall at dike crest);
- Window camera – approximately: 0.4 mm/px (at the window outer surface).

Obtaining sufficient resolution of the image was also a deciding factor in the choice of camera settings and mounting location.

A summary of the camera recording settings and specifications is presented in Table 12.

Table 12: A list of camera settings used throughout the tests.

Specifications adapted from: GoPro (2016, pp. 44-45)

Resolution	**2.7k**
Horizontal resolution	2704 px
Vertical resolution	1520 px
Aspect ratio	16:9
Framerate	60 fps
Bitrate (average)	60 Mbps
Field of view	
FoV setting	Linear
Vertical FoV (estimated)	~52.8°
Horizontal FoV (estimated)	~82.7°
Frame correction	In-camera, Linear
Recording mode	
Overview (OV)	Auto
Side view (SV)	Protune
Window (W)	Protune
Light sensitivity (SV, W)	400 ISO
Light sensitivity (OV)	Auto
Shutter speed	Auto
Stabilization	No
Estimated recording time - 128 GB SD card (for settings above)	4 h 17 min

3.3. Small scale test

The small scale physical model tests were conducted outside of the WALOWA initiative, in early 2015. The work of Streicher et al. (2016) is based on these exact experiments (two of the authors later also participated in the WALOWA initiative). The model setup is largely identical to the one used in the WALOWA tests, albeit with a few differences that are outlined later in this section. The purpose of introducing these experiments is to facilitate the small-to-large scale comparison needed for this study. However, it is important to point out that the author of this work did not personally participate in the small scale test programme, and data was accessed through collaboration with one of the Streicher et al. (2016) authors. This section is also largely based on the Streicher et al. (2016) publication, where more details can be found.

3.3.1. Model setup

The 1:25 scale (termed *small scale*) physical tests were conducted by Streicher et al. (2016) at a Ghent University testing facility in 2015. The flume is 30 m in length, 1.2 m in height, and 1 m wide, and equipped with a piston-style wave generator with reflection compensation (Streicher, et al., 2016). The model setup is schematically represented in Figure 28. Similar to the large scale tests, the small scale model has a 1:35 foreshore extending towards a 1:2 dike, a dike crest (also termed promenade) length of 0.40 m (1:25; corresponding to 2.325 m in 1:4.3 scale), and finishing off with a wall with matching height (0.275 m in 1:25, or 1.60 m upscaled to 1:4.3). One notable difference is the lack of a break in the slope (1:10) at the offshore extent of the foreshore, which was present in the large scale test setup.

Irregular waves were generated using a JONSWAP spectrum with a peak enhancement factor γ=3.3. With regard to the wave conditions, six of the small scale tests matched the wave conditions for the large scale tests maintaining Froude-similitude (see Table 4 in Section 3.1.1.). A detailed comparison of the two model setups is presented later in Section 3.3.3.

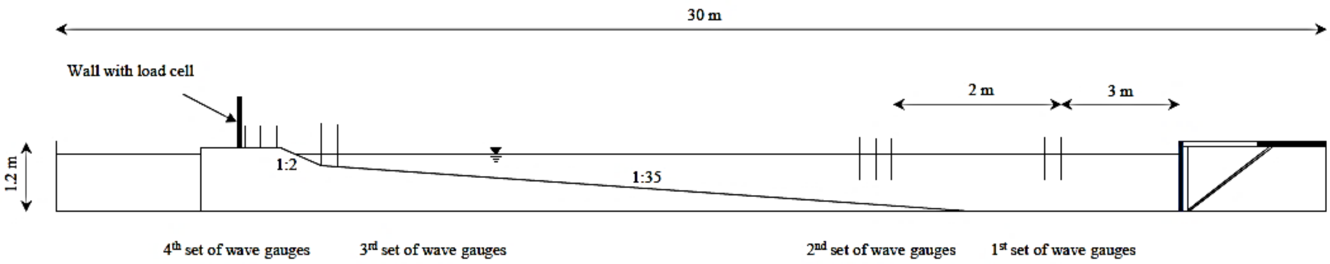

Figure 28: Schematic representation of the cross-section of the Streicher et al. (2016) model setup. Data obtained from these tests is used for comparison purposes with the WALOWA tests.

Source: Streicher et al. (2016, p. 3)

3.3.2. Measurement setup

A detailed explanation of the measurement setup for the small scale tests can be found in Streicher et al. (2016). Here, emphasis is instead kept on the data that was provided for comparison purposes.

Load cell

In order to record the impact forces at the wall, a load cell and strain gauge combination was used (Streicher et al., 2016). The load cell used was a 3 kg Tedea-Huntleigh manufactured unit, model 1042, sampling at 1000 Hz (Streicher et al., 2016). The width of the front plate was reported by the authors to be 0.1 m wide. Figure gives an overview of the small scale model promenade as built.

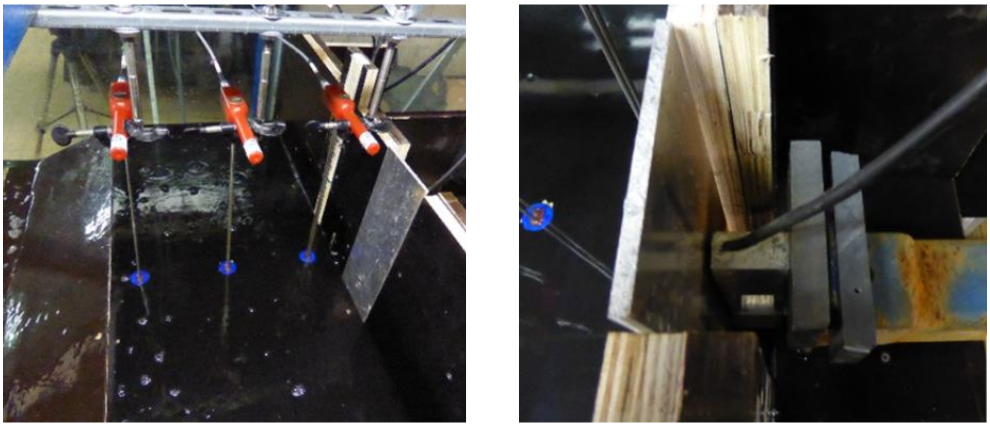

Figure 29: Load cell used in the small scale tests conducted by Streicher et al. (2016). Left: view from the promenade. Right: top view of the mounting setup.

Image source: Streicher et al. (2016, p. 3)

Side-mounted camera

A camera (termed *side-mounted camera*) recorded the impact events at the wall, also capturing the wave approach along the foreshore (limited to the dike toe area), the overtopping and post-overtopping flow (bore propagation) and the impacts at the wall. This recording covered the entirety of the small scale test chosen for analysis (corresponding to WLW_Irr_1_F in large scale). The device was mounted outside of the flume, recording through the transparent flume walls. Analysis of the video allowed for insight into the flow evolution and obtaining flow thickness and velocity information. A distance scale was positioned in the centre of the camera frame, oriented vertically, allowing for flow layer estimates of the flow layer thickness along the promenade. The video parameters for the available recording were determined to be:

- Resolution: horizontal – 1280 px; vertical – 720 px;
- Framerate: 25 fps;
- Bitrate – 6 Mbps.

3.4. Comparison of the two models

The large scale and small scale model setups were individually introduced in Sections 3.1. and 3.3.1., respectively. Here, a summarized comparison of the two models is presented in Table 13. The parameters only relate to large scale test WLW_Irr_1_F and its corresponding run in the small scale, since these tests were later studied in greater detail (see Section 3.4. and Chapter 4).

Table 13: Comparison between the small and large scale tests, including model geometry and construction, and wave parameters for the two tests later compared (see Section 3.4. and Chapter 4).

	Small scale tests* (Streicher et al., 2016)	**Large scale tests (WALOWA)**
Model scale	1:25	1:4.3
Model geometry and materials		
Foreshore	Concrete	Sand
	No 1:10 slope at offshore extent	1:10 slope at offshore extent
Dike	Wood	Concrete
Dike slope	1:2	1:2
Dike height [m]	0.52	0.53
Promenade	Wood	Concrete
Promenade slope	None	1:100
Promenade length [m]	2.33	2.33
Promenade wall	Wood	Steel
Wall height [m]	1.60	1.60
Wave conditions (WLW_Irr_1_F and corresponding small scale test)**		
Waves	Irregular; matching timeseries	Irregular; matching timeseries
Spectrum	JONSWAP; $\gamma = 3.3$	JONSWAP; $\gamma = 3.3$
Test duration* [s]**	6265	6257
Number of waves (N)	1000	1000
H_{m0} [m]	1.08	1.07
$T_{m-1,0}$ [s]	5.58	5.80
Offshore depth (h_{paddle}) [m]	4.01	3.99
Depth at dike toe (h_{toe}) [m]	0.29	0.28
Crest freeboard (R_c)	0.23	0.25

** Parameters have been Froude-upscaled to 1:4.3 for better comparability*
*** Parameters as measured during the tests (where relevant)*
**** Obtained from load cell timeseries (first to last impact)*

The similarity between the two model setups and wave conditions (Table 13) indicates a reasonable basis for comparison. Nevertheless, model effects are anticipated due to several notable differences. With regard to the foreshore, there is a variation in the configuration of the offshore extent of the two models, where the small scale test has a more gradual slope in several sections, which also extends comparatively closer to the wave generating board. As was shown in Section 3.1., the large scale model has a break in slope at the offshore extent. Furthermore, the materials used for the foreshore construction vary between the two test setups. The use of sand for the large scale test means not only that the foreshore can vary during a test, but also that the foreshore roughness will be comparatively different (and possibly also vary during a test as it adapts to the wave conditions). In comparison, the concrete foreshore in the small scale test will remain constant in shape, and also with regard to its roughness.

An additional difference between the two model setups are the model total length (longitudinally) and width (transversely). Froude-upscaling the dimensions of the small scale test setup to match the WALOWA test scale (scaling factor λ = 5.81), these differences amount to a 16.25 m shorter overall model length and a 0.81 m wider flume width. The difference in model length in particular could affect the interaction between incoming and reflected waves, although it is later shown that the wave interaction mechanisms correspond well between the two models (see Chapter 4).

Naturally, the variations outlined above and their anticipated effects on the incoming waves should be kept in mind before attributing any observed differences solely to scaling bias. It is therefore reasonable to facilitate the comparison between the two models using metrics measured at the onshore extent of the foreshore and/or the dike itself. Further elaboration could again be found throughout Chapter 4.

3.5. Methodology

This section introduces the approach adopted to achieve the aims of this thesis, with emphasis on the data from measuring instruments used for analysis purposes in this thesis. Note that not all experimental measuring techniques (see Sections 1.2. and 3.2.) are directly applied for the comparison of wave impact forces conducted in this thesis.

3.5.1. Hydraulic physical tests

To necessitate a study of scale effects, two corresponding tests, one in 1:25 scale and one in 1:4.3 scale, were chosen for comparison. The large scale test, as previously mentioned, was WLW_Irr_1_F. The small scale test featured the same irregular wave generation signal, Froude-downscaled to the respective scale. Both tests correspond to a 1:17 000 year storm event with an additional 20% enhancement, equating to very severe wave conditions. The wave parameters for these tests were presented in Table 13 in Section 3.4. Data from these tests was processed by individual parties in the WALOWA team and shared between participants, stemming from the project's collaborative nature. This is the case, for example, for the impact force data from the load cells (both small and large scale) and the pressure sensors (large scale). On the other hand, postprocessing of data for several instruments (see Section 3.2.) was under the author's control. Out of these devices, in this section emphasis is kept on the laser scanner and side view camera due to their large contribution to the analysis later presented in Chapter 4. Additional data processing was also necessary for the small scale test.

3.5.2. Wave induced forces at the wall

In this work, a primary tool for quantifying scaling bias was the force-time signal recorded at the wall. Based on the literature review (see Section 2.6. in Chapter 2) it was anticipated that if the comparison of the impact forces between the small scale and the large scale test does show scaling effects, these would be present primarily in the initial *dynamic force peak* portion of the force-time signal. Furthermore, it was expected that the Froude-upscaled small scale data will tend towards overpredicting the related force magnitudes (Bullock et al., 2001, Lafeber et al., 2012a, 2012b). If this effect is present, it could reasonably be attributed at least partially to differences in air entrainment and detrainment mechanisms, and resultant 'cushioning effect' (or lack thereof) (Bullock, et al., 2001, 2007; Blenkinsopp & Chaplin, 2011). However, a direct comparison between the two models of the influence of entrapped or entrained air on scaling bias by means of air void fraction measurements was not feasible. This is down to the fact that obtaining flow aeration data was outside the scope of the small scale test that had already been conducted by Streicher et al. (2016) (one of which is used here as the 'small scale' test in the comparison). Therefore, no small scale aeration data was available. A further consideration was that impact force measurements using pressure sensors perform better at capturing the initial *dynamic force peak* (Chen et al., 2014), where the effects of the void ratio (increased compressibility and lower density of the air-water mixture; Bullock, et al., 2001) are most prevalent (Lafeber et al., 2012a, 2012b). For the small scale test, however, pressure sensors were not implemented. Without capturing the initial impact peak in detail, it is difficult to quantify the contribution of the air void ratio to scaling bias. Instead, a qualitative approach was adopted, where the findings of Lafeber et al. (2012a, 2012b) introduced in Section 2.5. were utilized.

This necessitated the comparison between impact forces be done using data from the load cells used in both tests. An identical filtering routine was applied to both force-time signals, scaled accordingly to match the respective model scale. The force data processing itself (including filtering) was outside the scope of this thesis, and was instead performed by the WALOWA team. The following filter and threshold parameters were reported:

Large scale

- Frequency domain:
    - Low pass filter = 60 Hz;
    - Band pass filter 1 = 1.366 to 1.370 Hz;
    - Band pass filter 2 = 4.103 to 4.107 Hz;
    - Filter design: Butterworth.
- Other:
    - High pass threshold = 0.14 kN/m;
    - Detrend;
    - Baseline correction.

The small scale force data processing and filtering was also done externally. The parameters applied were reported as follows:

Small scale

- Frequency domain:
    - Low pass filter = 25 Hz;
    - Filter design: Butterworth
- Other:
    - Detrend;
    - Baseline correction.

The provided post-processed load cell data for both scales included the complete timeseries of all impacts sampled at 1000 Hz, as well as the time and peak magnitude of each detected impact event. To apply the classification of bore impacts after Streicher et al. (2016), the largest 10% of peak force impacts for each scale were identified, and the value of the lower peak recorded manually. Note that for the force data of the small scale test, no high pass threshold was applied, resulting in a higher total number of discernible impacts, but up unitl lower magnitudes. This was taken into consideration when the impact force analysis was conducted. For the Streicher et al. (2016) classification based on the force peak ratio, the 10% of highest impacts related to the corresponding total number of impacts. This decision was made based on the closer threshold of the corresponding lower intensity impacts in this 10% group. Additionally, the sensitivity analysis was also performed for the alternative definition of these impacts, but did not show notable differences in the impact type distribution. More information can be found in Section 4.3. (also refer to Appendix 13).

For the indepth analysis of individual impacts, a decision was made to directly compare force-time signals of the highest 4 impacts at each respective scale. These constitute the $F_{1/250}$, which is the arithmetic mean of the largest forces within 1/250th of the number of waves. These impacts were also used fot the flow evolution analysis (Section 3.5.3.).

Synchronization of the load cell data for the large scale tests was achieved as elaborated in Section 3.2. For the small scale test, this could be determined with sufficient accuracy from the moment the first wave was observed impacting the load cell.

3.5.3. Flow evolution

The flow evolution parameters were of interest in order to relate the recorded impact forces to the overtopping events that caused them. This analysis was conducted for the four largest peak impact events at both scales and aimed to outline the interaction mechanisms observed for the pre-impact flow and their respective force-time signal at the wall during impact. The goal was to assess how well these compare between the two scales, and if scaling bias can be observed. For this purpose, the largest peak force events were determined from the load cell data for both the small and large scale test. The corresponding events were then extracted from the laser scanner profile measurements and side view camera (large scale), and for the side-mounted camera (small scale).

Laser scanner

The primary purpose of the laser scanner was to capture a representative two-dimensional profile of the water surface near the wave impact location (end of foreshore to steel wall). This allows for a number of analyses to be performed. Here, the device's data was used to provide insight into the wave propagation mechanisms, determine pre- and post-overtopping flow characteristics, to obtain the overtopping flow layer thickness and bore front velocity along the promenade.

The processing of the laser scanner data was done through Matlab. As mentioned, the SOPAS recording software allows the user to export data under a CSV format. The original CSV file was then split into smaller files, each containing 5000 lines and maintaining the original header. This enables easier processing of the data due to the more manageable file sizes. A script was used to load the recorded data into Matlab, generating a so called 'output' file containing:

- *R-ϑ* – the distance value for each successfully recorded pulse, corresponding to an angle (θ, in degrees) and time value (in ms); R is recorded in mm.
- *RSSI* – the intensity of the received reflected signal for each successfully recorded R-value, in time;
- *t* – the timesteps corresponding to each scanned profile; measured in ms.

Once the data is loaded, a conversion from polar to Cartesian coordinates is necessary. This is done using Eq. 3.1. for the x-coordinate, and Eq. 3.2. for the z-coordinate. Note that the obtained coordinates correspond to the LCS reference system.

$$x_i = R\sin\theta - x_s \tag{3.1.}$$

$$z_i = h_s - R\cos\theta\cos\phi \tag{3.2.}$$

where x_i and z_i are the coordinates of a scanned point *i* in LCS, *R* is the recorded distance and ϑ the corresponding angle value, both equating to polar coordinates, φ is the slant angle, x_s is the horizontal offset of the device with regard to the LCS origin point, and h_s the vertical distance, again, from the origin of LCS to the device. Figure 30 gives an overview of these parameters.

Both the mounting method and inaccessible position necessary for mounting the laser scanner were expected to introduce slight deviations in the orientation of the device. Once the coordinates were converted, it was possible to assess whether there is need for correction. For this purpose, the known size, position, and orientation of the steel wall were used as a reference. Furthermore, the position of the scanned profile along the (vertical) steel wall was determined and marked at the wall foot and top part. By then measuring the distance to the flume wall (where the device was mounted), the slant angle could be corrected. Additionally, it was found that the device's vertical axis was slightly rotated (0.515° towards the wave board). This was corrected for in the coordinate conversion process by subtracting the offset value from the predetermined FoV (original FoV 18° to 132° corrected to 17.485° to 131.485°). Lastly, the device's internal reference system assumes the vertical axis to be 90°. This was also corrected for by subtracting 90° from the original recorded angle value. Eq. 3.3. gives the correction parameters for obtaining ϑ_{cor}.

$$\theta_{cor} = \theta - 90^o - C_{err} \tag{3.3.}$$

where C_{err} is the vertical axis rotation correction factor (0.515°).

Note that for the conversion in Eq. 3.1. *and* 3.2. ϑ *is* now substituted with ϑ_{cor} . The finalized conversion parameters ate given in Table 14.

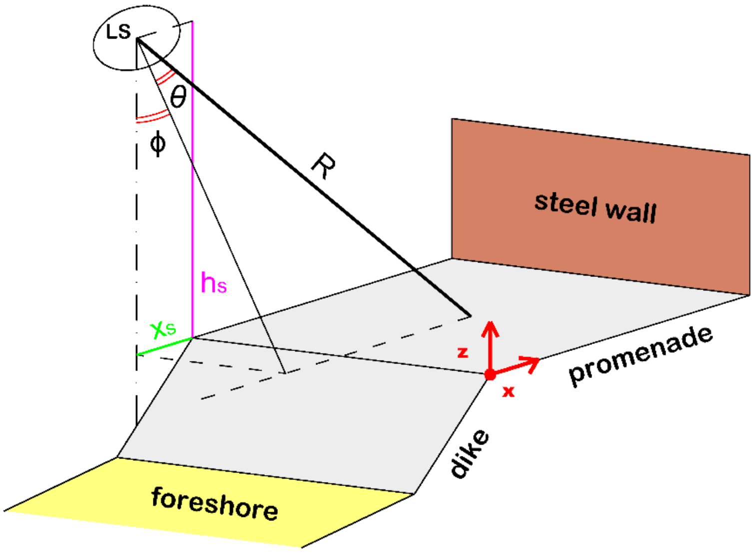

Figure 30: Schematic representation of parameters needed for converting the laser scanner coordinates.

Table 14: Finalized conversion parameters for obtaining Cartesian coordinates in LCS reference system for the laser scanner recording.

Parameter	**x_s**	**h_s**	**R**	**θ**	**θ_{cor}**	**C_{err}**	**ϕ**
Unit	**[mm]**	**[mm]**	**[mm]**	**[deg]**	**[deg]**	**[deg]**	**[deg]**
Value	526.3	4749	*vary in space and time*		θ-90°-C_{cor}	0.515	23.21

Once the Cartesian coordinates were obtained, a five-element median filter was then applied to each point in both space and time, as suggested by Diamantidou (2014). This allows for erroneously recorded individual spots to be corrected, but also proved beneficial for correcting variations in distance measurements due to the varying reflectivity of the scanned surface. It was apparent that this latter effect is especially prominent for points scanned along the steel wall. The median value of 5 elements produced a satisfactory correction of this effect (Figure 31).

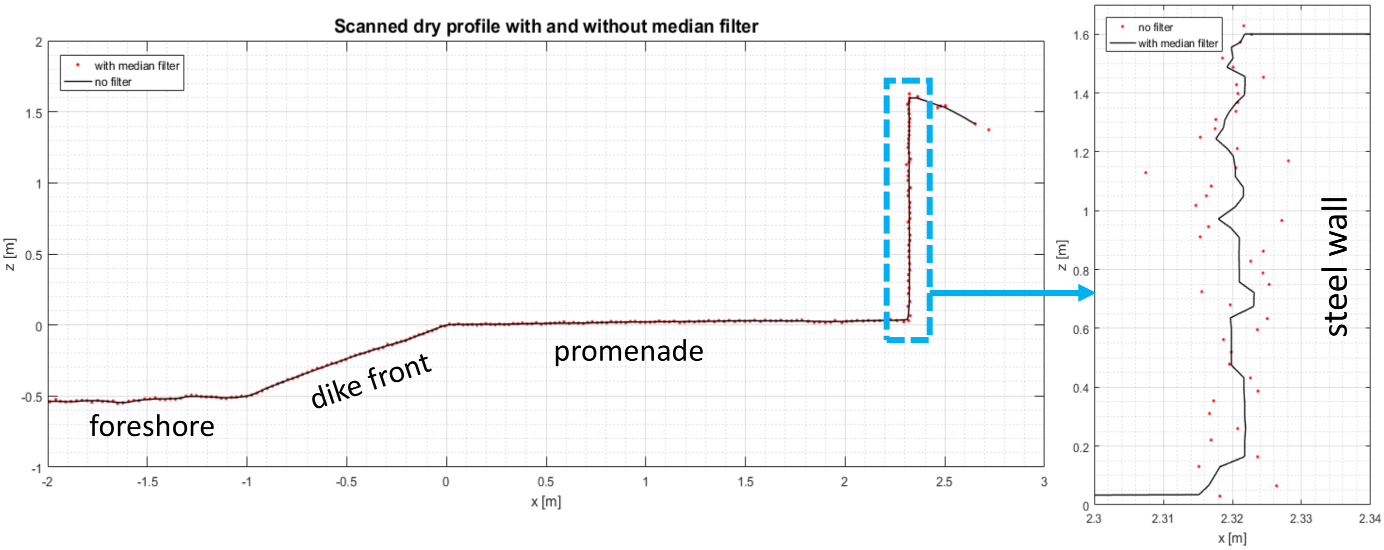

Figure 31: Comparing a single scan profile with and without a 5-element median filter applied for a dry profile. Left: points match reasonably well along the dike and promenade. Right: scattered points are observed at the wall, and are brought within a +/- 3 mm accuracy (note: scales are distorted).

It was important to obtain a reliable measurement of the dry profile of the model to use as baseline for the flow evolution analysis and obtaining the post-overtopping flow parameters (velocity and layer thickness). This was achieved with a 10 second recording of a completely dry model. The same steps as outlined above were followed (including a 5-element median filter), but then all corresponding points (within a single angle value ϑ) were averaged in time to calculate a more reliable profile measurement. This method produced an even smoother baseline profile than the one seen in Figure 31, improving the accuracy to approximately +/- 1.5 mm along the steel wall surface.

The *x* and *y* coordinates of the dike crest, landward end of promenade, foot and top of the steel wall, were determined and related to a corresponding FoV angle (ϑ_{cor}). The position of these points was later important for the velocity and layer thickness determination by the application of a so called geometrical filter – limiting the scan data to the scanned points of interest in space.

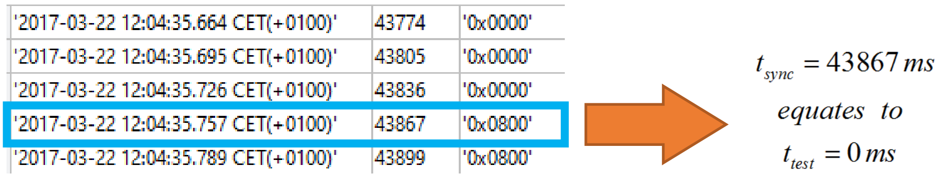

'2017-03-22 12:04:35.664 CET(+0100)'	43774	'0x0000'
'2017-03-22 12:04:35.695 CET(+0100)'	43805	'0x0000'
'2017-03-22 12:04:35.726 CET(+0100)'	43836	'0x0000'
'2017-03-22 12:04:35.757 CET(+0100)'	43867	'0x0800'
'2017-03-22 12:04:35.789 CET(+0100)'	43899	'0x0800'

$$t_{sync} = 43867\,ms$$
$$equates \;\; to$$
$$t_{test} = 0\,ms$$

Figure 32: Determining the sync pulse time t_{sunc} for test WLW_Irr_1_F equating to start of test (t_{test}). The blue rectangle outlines the initiation of the sync pulse (third column) and its corresponding time value (second column).

Since the laser scanner recording was handled by a separate computer, the initiation of a recording was started manually before the beginning of a test. In order to achieve synchronization with all other measurement devices, the sync pulse first had to be identified. The sync pulse is recorded in a separate column in the CSV file. When the pulse is sent, the value in this column changes (Figure 32) for the duration of the pulse (set to 1 second in the WALOWA tests). The test start is assumed to be the moment when the sync pulse is first recorded (t_{sync}), equating to $t_{test} = 0\ s$.

A flowchart of the laser scanner data processing approach summarises the steps outlined above (Figure 33).

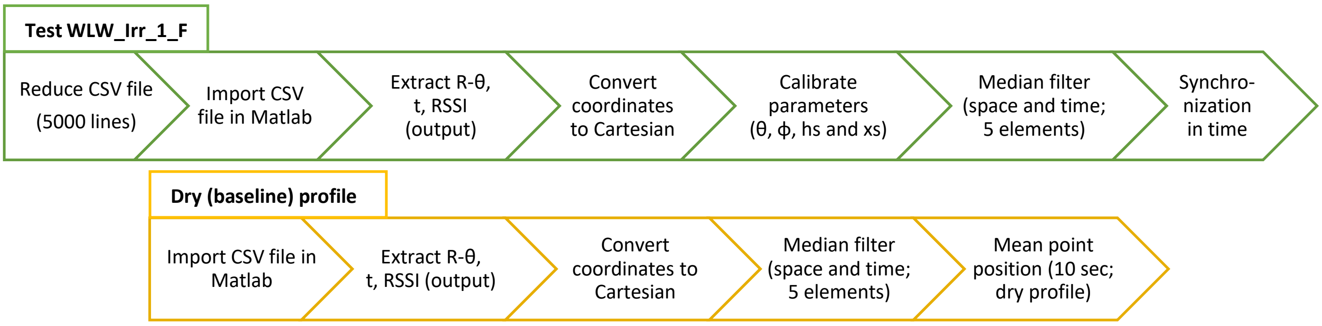

Figure 33: Flow chart summarising the sequence of laser scanner data processing for the test WLW_Irr_1_F (green) and obtaining a baseline (dry) profile (yellow).

3.5.4. Flow layer thickness and velocity

The flow layer thickness and velocity of the post-overtopping flow are two of the parameters included in the equation proposed by Van Doorslaer et al. (2017) for predicting the impact force at the wall (Eq. 2.4. in Section 2.3.2.), but also relevant for the pre-impact flow evolution analysis (Section 3.5.3.). For this purpose it was decided to obtain these parameters using the laser scanner and the side view camera data (large scale) and the side view camera (small scale). This decision was mainly based on the availability of the above data. Due to time constraints, more traditional layer thickness and velocity measurements used in the large scale tests could not be implemented in this work. For the parameters for the large scale tests, a semi-automated method was applied using Matlab. The duration of the scan which captured the timeframe between the bore front overtopping the dike and it impacting the wall was manually extracted. The average bore front velocity over the promenade was determined using the generalized Eq. 3.4.

$$U_{b,avg} = \frac{B}{N_s \frac{1}{f_i}} \tag{3.4.}$$

where $U_{b,avg}$ is the bore front velocity averaged over the promenade, B is the promenade length, N_s is the number of samples (frames or series of scanned profiles in this case) captured between overtopping the dike crest and initial impact with the wall, and f_i is the sampling frequency of the device.

For the laser scanner, this was slightly altered to instead implement the actual average time between scans rather than f = 35 Hz, since it was observed that the timestep value varied slightly between individual scans. Therefore, the promenade length (distance covered) was divided by the product of the number of (laser) scans and the average time between a scan. The obtained values were then compared with the footage captured by the side view camera, again using Eq. 3.4. to calculate $U_{b,avg}$.

Both methods produced similar results (order 0.1 s), although sometimes discrepancies were found. In such cases, it is recommended that the side view camera estimate is used. This is based on three considerations. First, it was observed that the bore was not always perfectly uniform along the width of the flume (y-axis). This could affect both the initiation of overtopping and the moment of impact with the load cell. Since the laser scanner 'observes' the bore only in two dimensions, such irregularities can produce an erroneous result. With the camera footage, it is possible to focus on a longitudinal profile that intersects the load cell, or an alternate definition of overtopping altogether. Secondly, the camera's sampling rate of 60 frames per second allows for greater precision when compared to the laser scanner's 35 Hz sampling rate. Lastly, it is possible that for a particularly shallow bore tip the laser beam will penetrate the water body and reflect internally, resulting in an underestimate of the layer thickness (Streicher, 2013). Hofland, et al. (2015) reported a threshold of 3 cm in vertical (z-axis) direction for run-up measurements along an inclined hard surface.

For determining the layer thickness (large scale), again the duration of an overtopping event was isolated from the laser scanner data. The peak of this parameter needed to be determined for the seaward end of the promenade (closest to the dike crest) (Van Doorslaer et al., 2017). Since there was no one point that measured in that exact location, and furthermore considering that the location of the points along the x-axis is slightly shifted when an overtopping flow is present, it was decided that the first four points along the promenade are going to be used. For the same duration of laser scanner recording used in the velocity determination, the change in the z-coordinate for the four points relative to the dry dike elevation (due to the 1:100 slope) was extracted, and the single maximum value among all four points was deemed the peak flow layer thickness for the corresponding event.

4. Results and Discussion

In this section, results based on the analysis of the data acquired through the WALOWA 1:4.3 tests (referred to as *large scale* tests) and the 1:25 scale tests (termed *small scale* tests) is presented, supplemented by discussion of results and their evaluation within the context of the previously introduced literature review (Chapter 2). All comparisons are made between the large scale WLW_Irr_1_F test and its corresponding small scale counterpart. This is done in both a quantitative and qualitative manner. The former is predominantly based on the load cell-derived force measurements and post-overtopping flow parameters, while the latter consists of an evaluation of the pre-impact flow evolution for the highest impacts at their respective scale.

Section 4.1. outlines the differences between the two scale models in the peak impact forces, with emphasis on the highest recorded impacts. Then, a comparison of the pre-impact flow evolution for the highest four impact between the two scales is made and linked to the force-time signals for these events (Section 4.2.). Section 4.3. outlines observed similarities and differences between the two models when applying the bore impact classification after Streicher et al. (2016), and their distribution in relation to the force magnitude.

4.1. Comparison of peak impact forces

The peak impact force comparison is based on the load cells data for the large scale test WLW_Irr_1_F (1:4.3) and corresponding small scale (1:25) test. Although pressure sensors were used in the WALOWA tests, such measuring equipment was not part of the small scale test setup (refer to Section 3.5.2. for more details). Similarities and notable differences between the two model setups and conditions were also previously discussed (see Section 3.4.). For the purpose of this comparison, the large scale test serves the role of proto-full-scale, meaning that small scale test data is Froude-upscaled to 1:4.3 using a scaling factor $\lambda = 25/4.3 = 5.81$.

In total, 531 individual impact events were distinguished from the load cell force-time signal after filtering was applied to the large scale tests. In the small scale tests, the number of impacts was slightly higher at 572 total impact events distinguished, again, after filtering. As previously noted in Section 3.4., both tests were of nearly identical (Froude-scaled) duration and had the same number of incoming waves ($N = 1000$). A direct comparison of the recorded peak force during an impact event for both small and large scale tests is presented in Figure 34 in the form of an exceedance curve. Here, the small scale results are Froude-scaled to the large scale Delta flume test of 1:4.3 (using a scaling factor $\lambda^2 = 5.81^2$). Due to the difference in total force peaks detected, the x-axis is normalized between the two scales using $P_i = n/(N_{imp}+1)$, where n is the ranking of the impact force sorted by magnitude, and N_{imp} the total number of impacts at the respective scale. At first sight, it is apparent that the force data between the two tests matches reasonably well both in magnitude and distribution. This suggests that the differences between the two model setups (see Section 3.4.) did not introduce large model effects, but also that scale effects are limited.

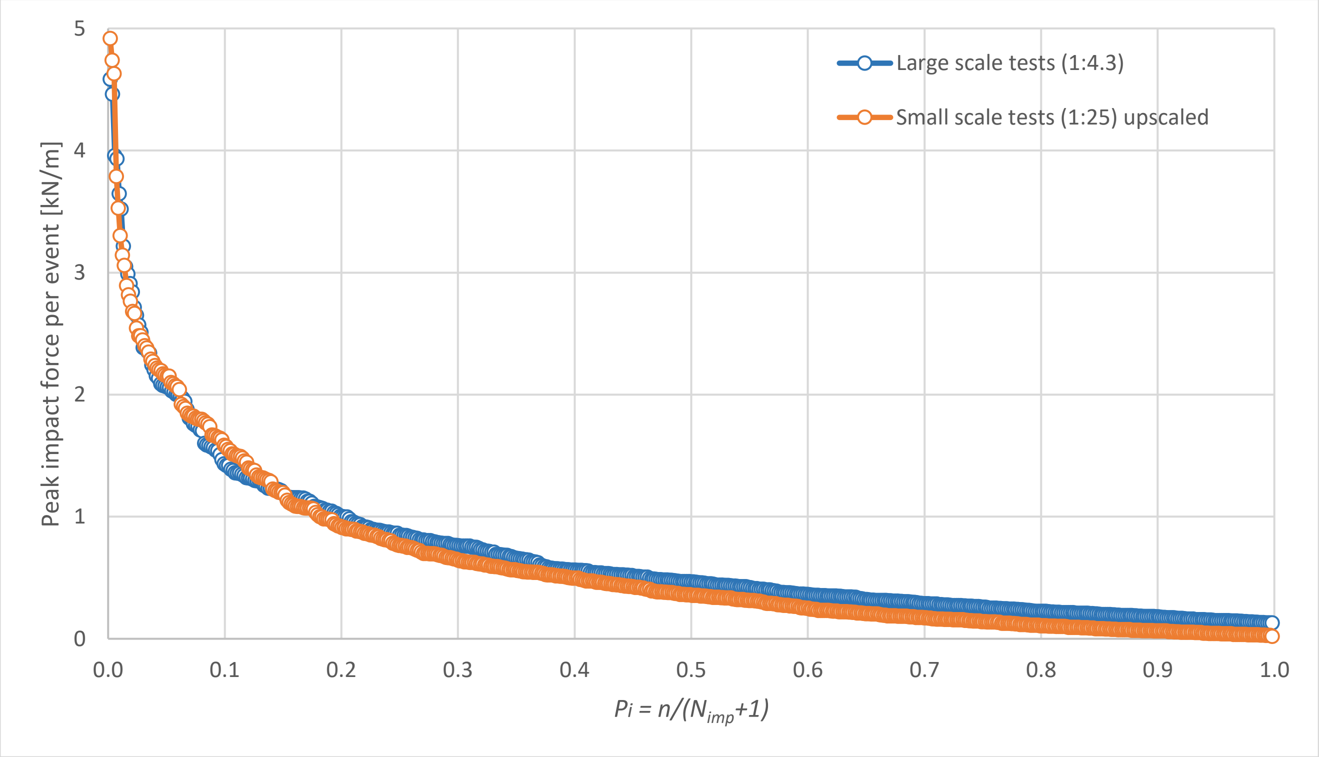

Figure 34: Comparison of small and large scale tests exceedance curve for all recorded impact events. Force data from load cells. Small scale data has been upscaled to match the scale of the large scale tests ($\lambda^2 = 5.81^2$).

The x-axis in Figure 34 is dependent on the number of impact events (and therefore force peaks) that could be distinguished from the signal. As mentioned, these differ between the two scales, but this is also at least partially due to the fact that more lower intensity impact events could be distinguished from the force-time signal of the small scale test. The difference in magnitude of the lowest force threshold is relatively large, at 0.1305 kN/m at large scale and 0.02 kN/m at small scale (Froude-upscaled to 1:4.3). For example, Chen (2016) uses a peak over threshold (POT) method based on the form of the mean wave power (Goda, 2010) and a fixed time interval roughly equal to the duration of a single impact event. To enable a better comparability between the force events in the two models, in Figure 35 a high pass threshold of 0.13 kN/m (1:4.3 scale) was used in the small scale model data. This matches the noise-induced lower threshold limitation in the large scale data and leads to a reduced number of impacts in the small scale model (N_{imp} = 438 events). The x-axis is again normalized using $P_i = n/(N_{imp}+1)$, this time using the updated N_{imp} value in the small scale test. The same data is also presented in Figure 36 using a base-ten logarithmic x-axis.

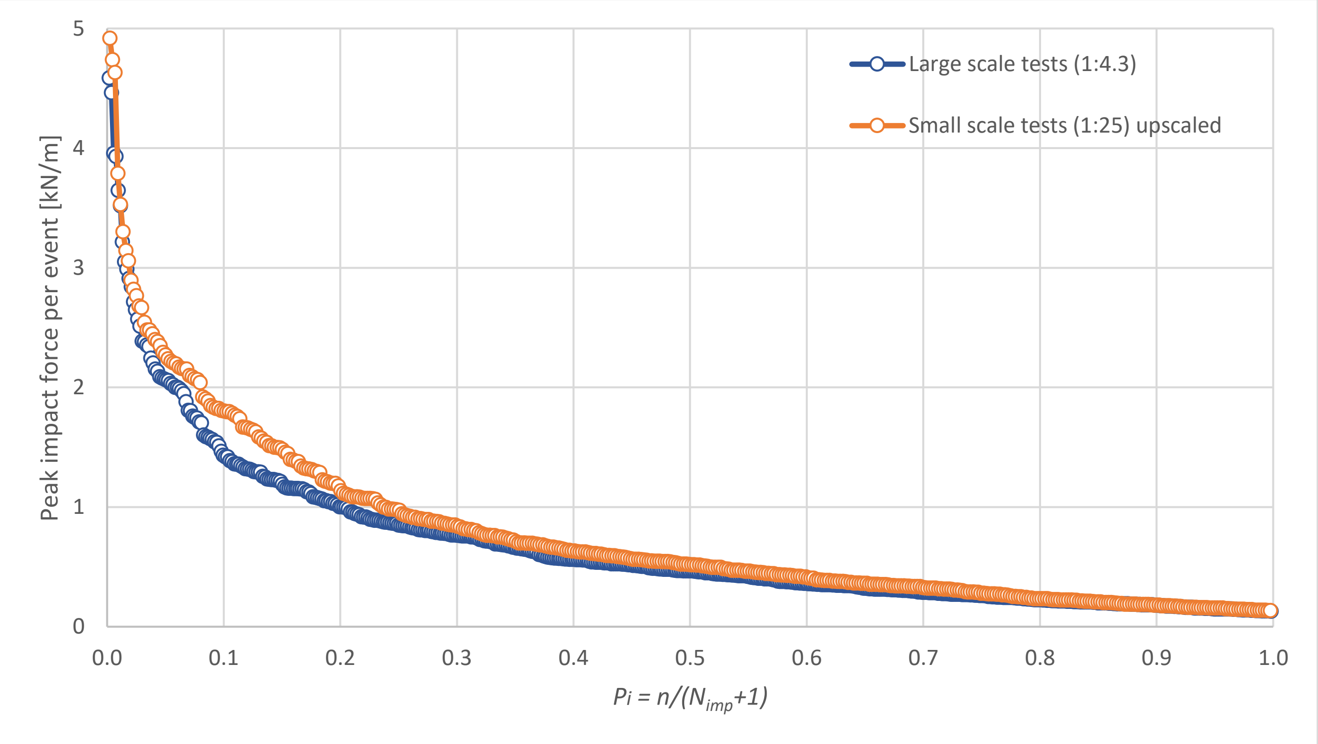

Figure 35: Comparison of small and large scale tests exceedance curve for all recorded impact events above a high pass threshold of 0.13 kN/m (1:4.3 scale). Force data from load cells. Small scale data has been upscaled to match the scale of the large scale tests ($\lambda^2 = 5.81^2$).

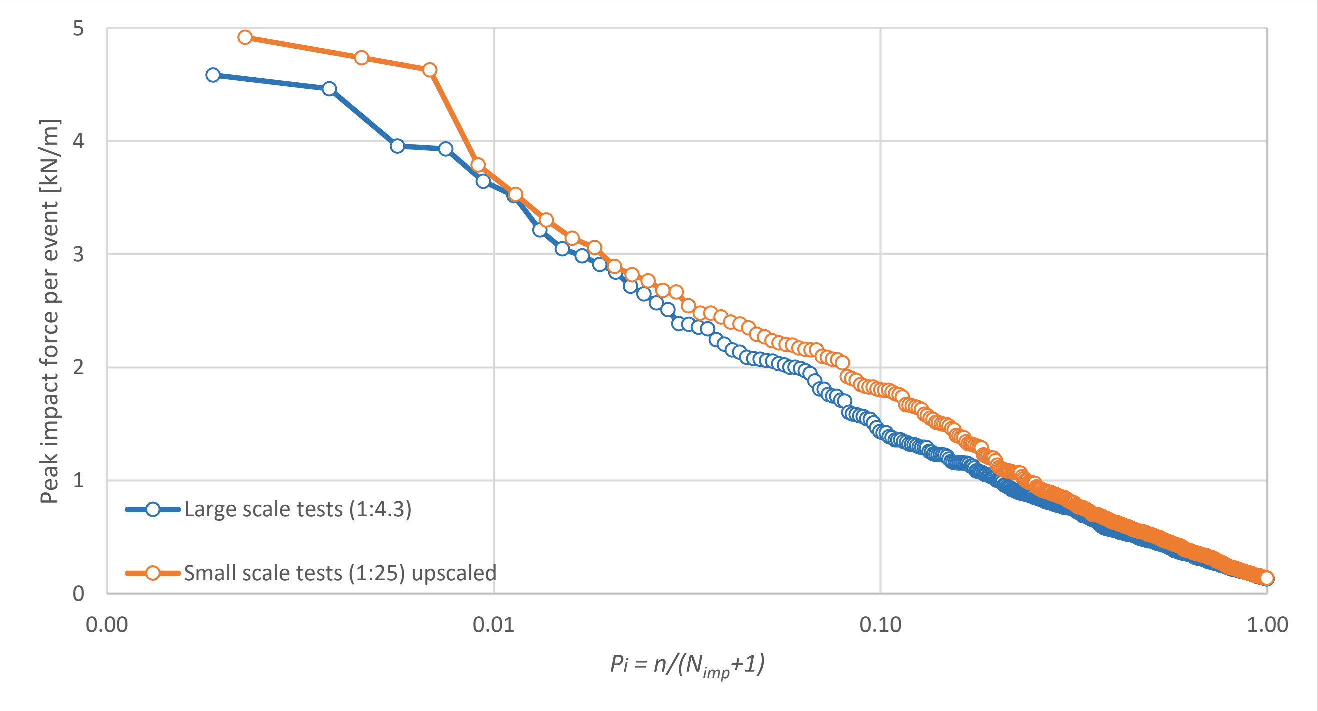

Figure 36: Comparison of small and large scale tests for all recorded impact events above a high pass threshold of 0.13 kN/m (1:4.3 scale). The x-axis uses a base-ten logarithmic scale. Force data from load cells. Small scale data has been upscaled to match the scale of the large scale tests ($\lambda^2 = 5.81^2$).

Some notable differences that can be observed from Figure 35 and Figure 36 are:

- The three highest peak force events are higher in the small scale tests;
- The two lines tend to converge for P_i between 0.01 and 0.03, but are generally slightly higher (order 0.1 kN/m) at small scale;
- Small scale peak impact force magnitudes tend to be higher for P_i between 0.03 to 0.3 with the highest difference around $P_i = 0.12$ (order 0.3 kN/m);
- Impact events for P_i higher than 0.3 but below 0.8 follow a very similar trend, although slightly higher for the small scale peak impact forces (order 0.05 kN/m);
- The two lines converge again for P_i above 0.8.

Part of the trends outlined above can more clearly be distinguished in Figure 37, where both the largest 10% of impact forces (left) and the highest 100 impact events (right) for both scales are presented. Note that the former is calculated after applying the high pass threshold of 0.13 kN/m for the small scale force data.

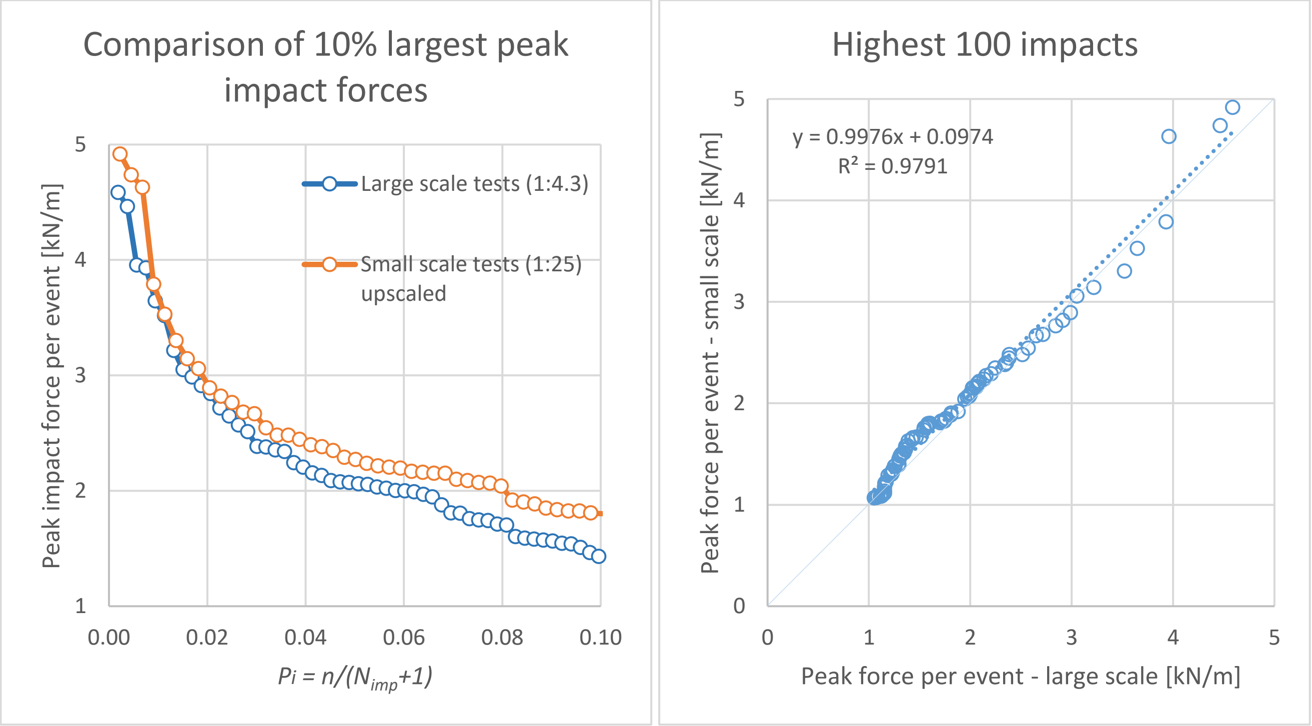

Figure 37: Comparison of the largest 10% of impacts forces after high pass threshold correction (left) and the highest 100 impact forces (right) for both small and large scale tests. Force data from load cells. Small scale data has been Froude-upscaled to match large scale data ($\lambda^2 = 5.81^2$).

A comparison of the forces at the two scales by applying some commonly used metrics is presented in Table 15. Here, F_{max} is the single highest recorded peak force at the wall, F_{mean} is the arithmetic mean of all discernible forces above the high pass threshold, $F_{m,10}$, $F_{m,50}$ and $F_{m,100}$ are again the arithmetic mean but for the largest 10, 50 and 100 impact force peaks, respectively, $F_{1/250}$ is the average of the highest 4 impact events for a test of approximately 1000 primary waves, as described by Van Doorslaer et al. (2017), and $F_{10\%}$ the arithmetic mean of the highest 10% of impacts (above the high pass threshold).

In all metrics compared in Table 15, the Froude-upscaled forces from the small scale tests are higher. However, the differences observed are relatively low, at about 7 to 10 % for the highest intensity impact events. $F_{m,10}$, $F_{m,50}$, and $F_{m,100}$ all show a similar trend, although with an even lower margin (2 to 5 %). So far, it seems that the small scale peak force data show a tendency for overprediction when Froude-upscaled, especially for the highest intensity impacts. However, the results in Table 15 indicate that some of the metrics chosen for comparison show a smaller bias. It is therefore important to consider the relative difference in scale between the two models.

Table 15: Comparison of forces at the two scales using popular metrics. Number of impacts after application of high pass threshold of 0.13 kN/m. Force data from load cells. Small scale data has been upscaled to match the scale of the large scale tests ($\lambda^2 = 5.81^2$).

	Large scale (1:4.3)	**Small scale (upscaled to 1:4.3)**	**((Small scale/Large scale)*100)-100**
	load cell data [kN/m]	load cell data [kN/m]	%
$\mathbf{F_{max}}$	4.59	4.92	7.3
$\mathbf{F_{mean}}$	0.69	0.77	12.5
$\mathbf{F_{m,10}}$	3.63	3.68	1.5
$\mathbf{F_{m,50}}$	2.34	2.43	3.9
$\mathbf{F_{m,100}}$	1.79	1.89	5.2
$\mathbf{F_{10\%}}$	2.30	2.53	10.0
$\mathbf{F_{1/250}}$	4.23	4.52	6.7

In this comparison, the large scale test serves the role of a baseline to compare to, what could be termed a 'proto-full scale' model. Hence, the small scale model's relative scale is then 1:5.81 ($\lambda = 25/4.3 = 5.81$). In this relative sense, the small scale test is actually a comparatively large scale experiment. Bearing in mind that often such experiments are conducted at higher scale factors (λ), the approximately 2 to 12 % difference shown in Table 15 is expected to increase (Heller, 2011). This is not expected to follow a linear trend (i.e. linear extrapolation of the results presented here is not advisable), and requires, for example, several additional experiments at intermediate scales and a true prototype-scale baseline case. Nevertheless, it is safe to imagine that upscaling of the 1:25 model data to prototype scale will further increase this gap, due to, in essence, scaling bias (Heller, 2011). Furthermore, so far this seems to support the findings of the literature review (Chapter 2) and previous research (e.g. Bullock et al., 2001, 2007; Lafeber et al., 2012a, 2012b), where it was suggested that Froude-upscaing small scale derived impact force data can lead to overestimation in the peak impact forces.

4.1.1. Force-time signal

Figure 38 and Figure 39 show the force-time signal from the load cells for the entire test length (large and small scale, respectively). All identified peaks in the signals are marked with red circles, with the highest four impacts forces further circled in blue. It is apparent that even though the two wave generation signals were identical, the highest impacts (marked in blue in both figures) occurred at different moments in time, meaning different waves (or wave groups) caused them. The maximum peaks in both scales appear to be occurring at very close timepoints in Figure 38 and Figure 39, but further analysis showed that they are more than 4 minutes apart (time in 1:4.3 scale), meaning they also were caused by completely different waves. It should be noted that an apparent discrepancy was observed in the instantaneous water surface elevation η measurements of the wave gauge at the dike toe for the large scale test. However, this was later attributed to erroneous measurements. More information can be found in Appendix 10.

It could be reasoned that the variations outlined above can be at least partially attributed to model effects, at least two of which are thought to be the additional break in slope at the offshore extent and the mobile bed in the 1:4.3 tests (see Section 3.4.). Both can alter the wave group propagation along the foreshore. Scale effects could contribute to this variation in force peak distribution in time. However, the forces also have an inherent variability. Chen et al. (2014) remarked that even for a single scale, regular wave setup, relatively large variations in the force-time signal between tests were observed. Lafeber et al. (2012a) also touched on the difficulties in achieving reasonable flow similarity between two scales even for a single wave packet, attributing this to scaling bias introduced during the wave propagation and pre-impact stages. It is thought that this is also the case here, furhter exacerbated by the long and complicated propagation process of the generated irregular waves. The respective bias contribution of scale and model effects and inherent variability could not be determined. Therefore, a qualitative approach is applied (see Section 4.1.2. and 4.2.), looking at specific impact patterns between the two scales and their corresponding force-time signal, post-overtopping flow parameters, and applying the concept of ELPs (Lafeber et al., 2012b) that was introduced in Chapter 2.

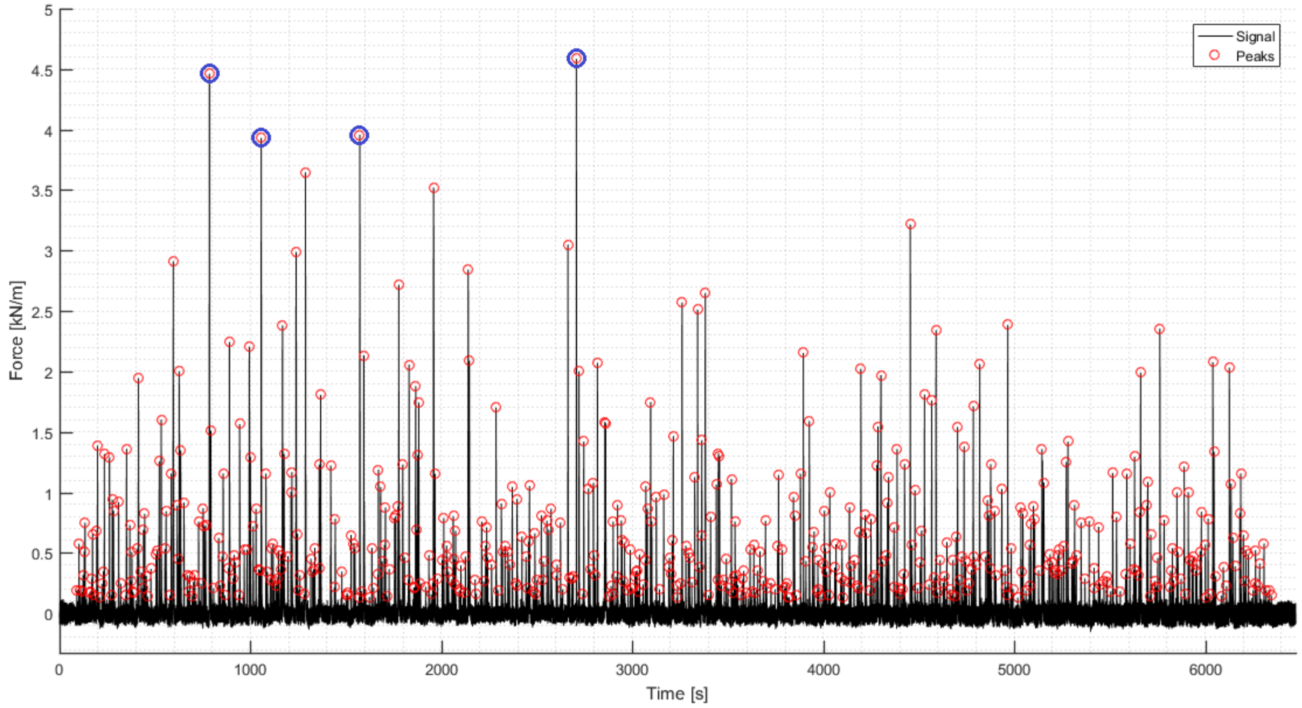

Figure 38: Force-time signal for the entire length of test WLW_Irr_1_F (large scale). Values in model scale (1:4.3). Highest four impact forces are circled in blue. Force data from load cells.

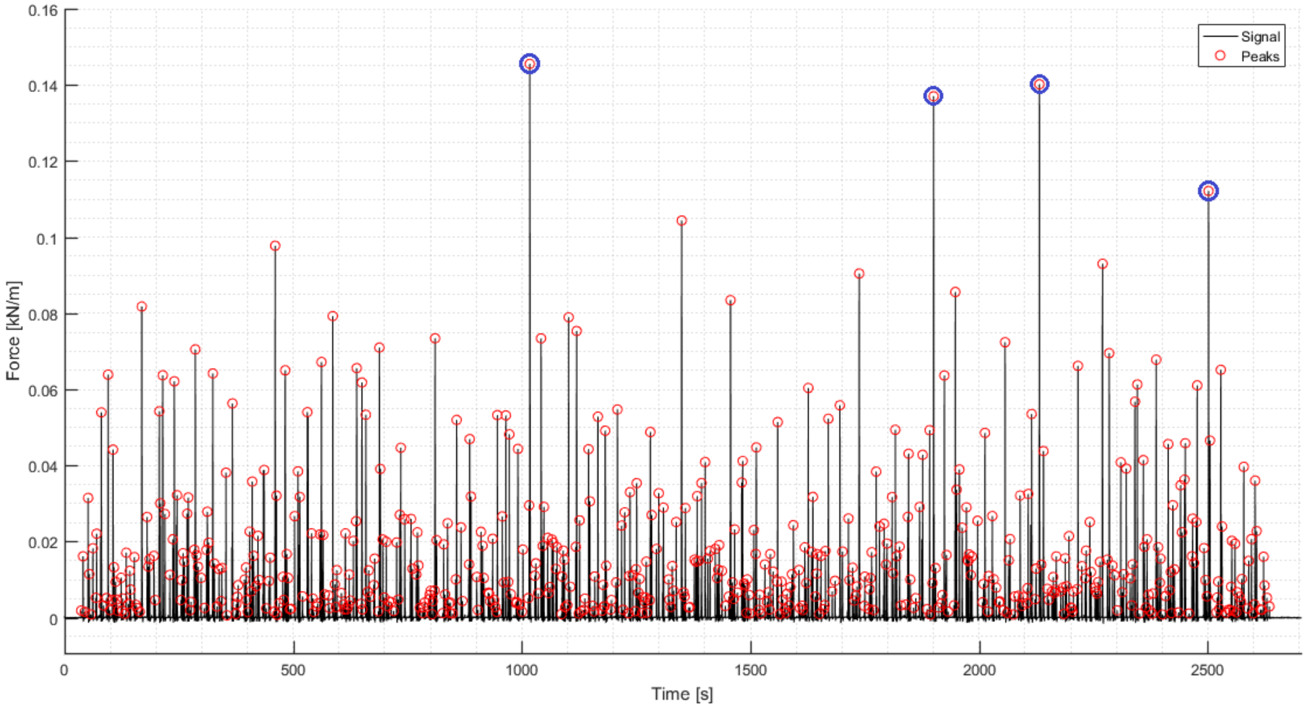

Figure 39: Force-time signal for the entire length of the small scale test. Values in model scale (1:25). Highest four impact forces are circled in blue. Force data from load cells.

4.1.2. Maximum impact forces

Usually for design purposes the highest impact forces are of most interest. Therefore, the four impact events that produced the highest forces on the wall for both scales were individually analysed. This comparison was based on the load cells data since pressure sensors were not used in the small scale tests. Note that for brevity, the impacts will be referred to with a letter-number combination. For example, *L1* is the highest large scale impact force peak recorded, *S3* the third highest in small scale and so on.

The magnitude of the highest four impacts from both small and large scale tests are plotted in Figure 40. For a 1000 waves test these can also be linked to the definition of $F_{1/250}$ (Van Doorslaer et al., 2017), therefore, this is also plotted in Figure 40 - right. The exact peak force values are also compared in Table 16.

Table 16: Peak values for the four largest impact forces at each scale (plotted in Figure 40). The larger value for a given set is highlighted in blue. Data from load cells. All values in 1:4.3 scale.

Large scale tests (1:4.3)	**kN/m**	**L1**	**L2**	**L3**	**L4**	**$F_{1/250}$**
		4.59	4.46	3.96	**3.93**	4.23
Small scale tests (1:25) upscaled	**kN/m**	**S1**	**S2**	**S3**	**S4**	**$F_{1/250}$**
		4.92	**4.74**	**4.63**	3.79	**4.52**
(Small scale/Large scale)*100-100	**%**	+7.3	+6.2	+17.0	-3.6	+6.7

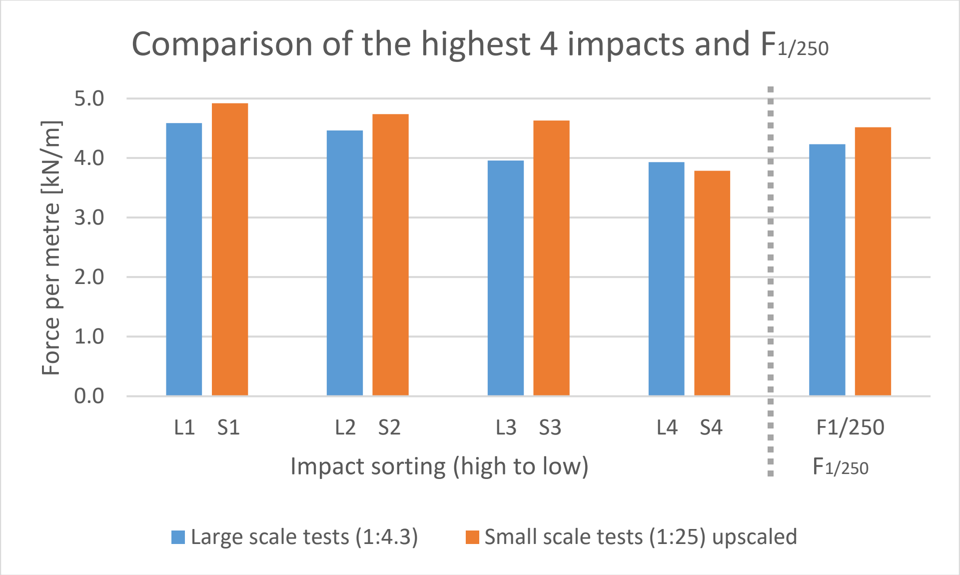

Figure 40: Comparison of the highest four impacts recorded for the small (denoted S) and large (denoted L) scale test (left). Comparison of the calculated $F_{1/250}$ force for both scales (right). Force data from load cells. Small scale data has been upscaled to match the scale of the large scale tests ($\lambda^2 = 5.81^2$).

Applying the classification of Streicher et al. (2016) introduced in Section 2.2.1., the impact types are divided between *dynamic bore impacts* (L1, L3, S1) and *quasi-static-down-rush bore impacts* (L2, L4, S2, S3, S4) – see Table 17. As expected, no *pulsating bore impacts* are found here, as these are usually low force events (Streicher, et al., 2016). Furthermore, all impacts show the typical two-peak force-time signal shape, with L1 especially matching the classic 'church-roof' shape outlined by Oumeraci et al. (1993).

The force-time signals for the four highest impacts at both scales can be found in Figure 41. All data is presented in 1:4.3 scale (Froude-upscaled for small scale model). Axes are kept identical between all plots, and the time-axis is aligned using the moment of initial impact with the wall. Note that the apparent similarity in force-time evolution of the impacts here is likely coincidental due to the fact that they occur at different points in time. The impact signals are later also considered when assessign the pre-impact flow evolution (Section 4.2.).

In Streicher et al. (2016) it was noted that about 70% of *dynamic bore impacts* were further identified to include an *interaction* wave interference pattern – collision between a reflected and an incoming bore influencing the impact mechanism at the wall. Analysis of the force signal and video footage for the four highest impacts at both scales showed wave interaction patterns for both *quasi-static/down-rush bore* and *dynamic bore impacts*.

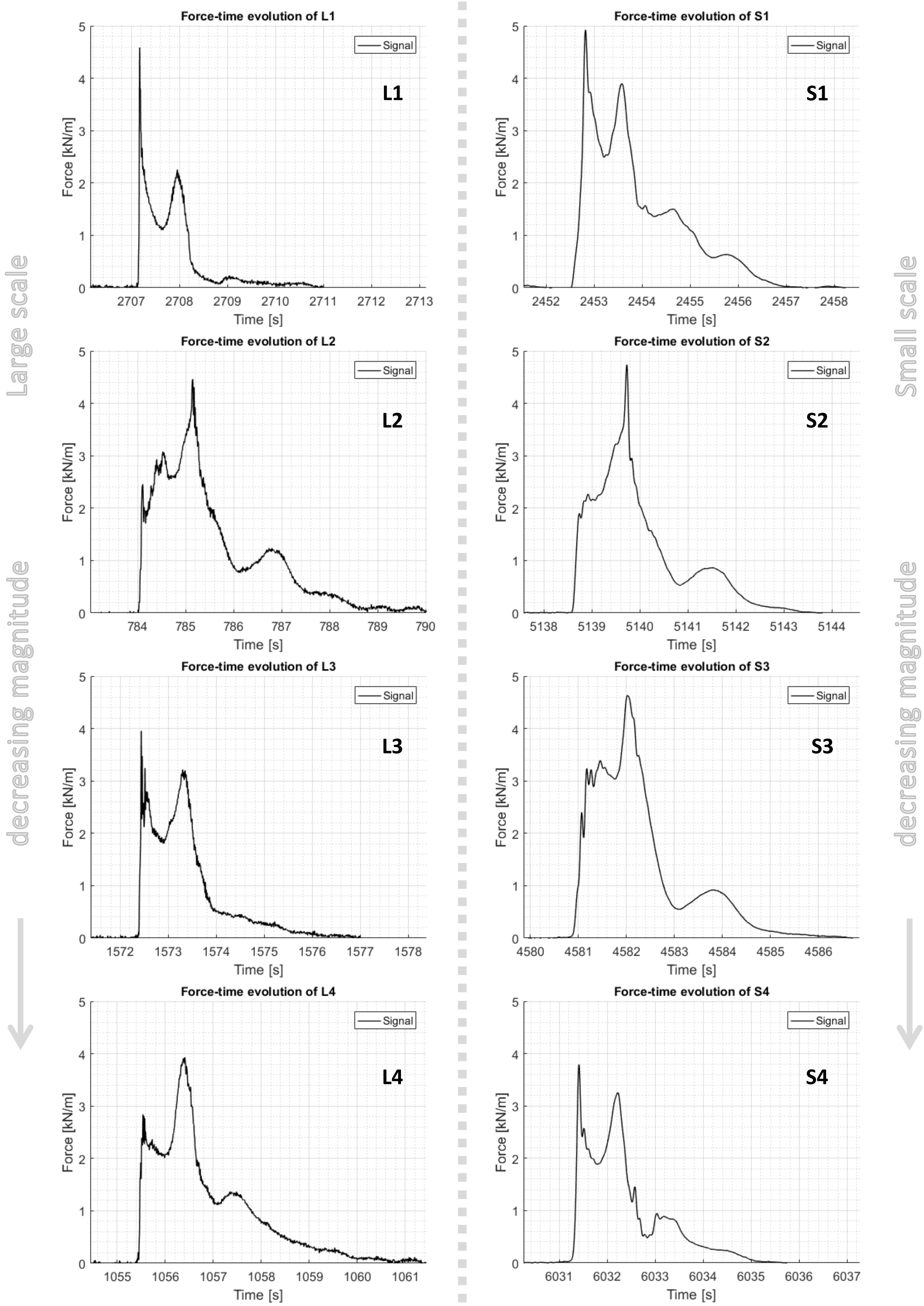

Figure 41: Force-time signal for the four highest impacts for large scale (left; L1 to L4) and small scale (right; S1 to S4). Vertical and horizontal axes identical for all impacts. Force data from load cells. Small scale force and time Froude-upscaled to match the large scale tests (λ = 5.81).

All eight impact events featured at least some residual water on the promenade – *wet bed*, but also sometimes of substantial layer thickness. For these impacts, although reflected bore induced breaking was observed, this did not occur in immediate proximity to the wall. Therefore, entrapped pockets of air, as observed by Streicher et al. (2016), did not contribute to the (four) maximum impact forces in this particular test setup.

Table 17: Classification of impacts after Streicher et al. (2016). The force peak ratio determines how an impact is classified. Threshold for dynamic bore impact is $F_1/F_2 > 1.2$ (Streicher et al., 2016).

Impact	Peak 1 (F_1)	Peak 2 (F_2)	Peak ratio F_1/F_2	Classification after Streicher et al. (2016)	Larger peak
L1	4.59	2.26	2.03	Dynamic bore impact	F_1
L2	3.08	4.46	0.69	Quasi-static/ down-rush bore impact	F_2
L3	3.96	3.22	1.23	Dynamic bore impact	F_1
L4	2.84	3.93	0.72	Quasi-static/ down-rush bore impact	F_2
S1	4.92	3.89	1.26	Dynamic bore impact	F_1
S2	2.27	4.74	0.48	Quasi-static/ down-rush bore impact	F_2
S3	3.39	4.63	0.73	Quasi-static/ down-rush bore impact	F_2
S4	3.79	3.25	1.16	Quasi-static/ down-rush bore impact	F_1

Further analysis of the force data and video recordings for the largest 10 peak forces impact events at each scale did confirm however the occurrence of such events. In the large scale test these impacts were L5, L7 and L8 (following the previously introduced naming scheme). Their peak impact force was between 72 to 86% of the magnitude of the corresponding $F_{1/250}$ (3.65 kN/m, 3.52 kN/m, and 3.22 kN/m, respectively). Unfortunately, these events occurred after the high-speed camera had stopped recording. At small scale only one such impact where air entrapment occurred was identified – S9, with a magnitude 64% that of the corresponding $F_{1/250}$ value (2.89 kN/m in 1:4.3 scale). It is interesting that this impact mechanism seems to be less prevalent at small scale, which is later also discussed in Section 4.3 .

Although comparatively lower in magnitude, it is often suggested not to disregarded the entrapped air pocket type of impacts, especially when considering the global exerted force on the wall (Lafeber et al., 2012a, 2012b; Bullock, et al., 2001). It is also interesting to see that with regard to the 10 highest impact events, the entrapped air pocket impacts appear to occur more frequently in the large scale test. This is also later confirmed in Section 4.3. where the impact classification of Streicher et al. (2016) indicates that the small scale test shows more *quasi-static/down-rush bore impacts* for the highest 10 events sorted by peak magnitude. A reasonable assumption would be that this discrepancy between the two models is at least in part caused by differences between the two models. The post-overtopping flow which governs whether such interference mechanism occur is dependent on, amongst other, the incident wave parameters (e.g. Chen, 2016, Van Doorslaer et al., 2017), which are affected by the foreshore variations between the two models. Nevertheless, investigating the impact mechanisms that were responsible for the observed (four) highest peak forces is also of interest. This is therefore further explored in Section 4.2. where the bore evolution for each of these highest impacts is analysed in detail.

Based on Bullock et al. (2001) and Blenkinsopp & Chaplin (2011), it is relevant to compare not only the maximum peak forces, but also their respecitve rise times between the two scales. Since the so called 'cushioning effect' of air usually (although not necessarily) leads to lower rise times, the more abundant presence of air in the flow in the full scale tests is expected to lead to lower (faster) rise times as well. However, analysing the signal shows that in the current tests, rise times appear to actually be higher (slower) for the samll scale tests. This can be explained with the fact that comparison is made between load cell data and not pressure sensors. As previously elaborated, Chen et al. (2014) noted that the initial rise in peak pressure is better captured by pressure sensors rather than load cells. An example of this effect is obvious in Figure 42 for a dynamic bore impact event (L3) from the large scale test, where both devices were available. For the small scale tests however, pressure sensors were not installed, so it is not advisable to draw conclusion on rise times soely based on the load cell data.

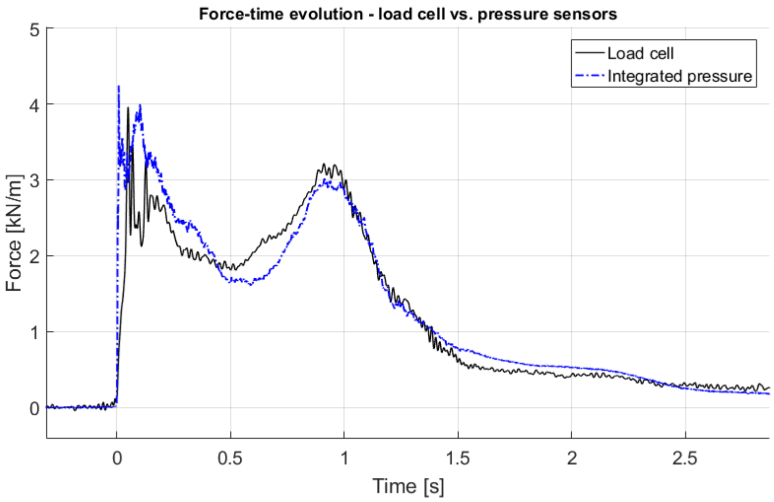

Figure 42: Force-time signal for a dynamic bore impact (L3) as captured by the pressure sensors (dashed blue line; integrated pressure) and load cells (black line). Note how the former exhibits a shorter rise time.

4.1.3. Flow layer thickness and velocity

Both layer thickness and velocity were suggested (e.g. Van Doorslaer et al., 2017; Chen, 2016) as governing parameters relating the overtopping flow to the forces at the wall (see Section 2.1.2.). Van Doorslaer et al. (2017) and Streicher et al. (2016) reported a low correlation between the overtopping flow velocity and the resulting loads. The latter noted the same for the peak layer thickness measured at the seaward extent of the promenade. Van Doorslaer et al. (2017) also reported improved correlation when the instantaneous discharge is used instead, which is approximated by the product of the two parameters (front velocity and layer thickness).

For the small and large scale tests, these parameters for the four largest impacts are presented in Table 18 (elaboration on the methods for obtaining these values in was presented in Section 3.5.4.). Figure 43 plots impacts L1 to L4 and S1 to S4 against the peak layer thickness (d_{crest}), the average bore front velocity along the promenade ($U_{b,avg}$) and the instantaneous overtopping discharge at the dike crest ($q_{inst}=U_{b,avg}\, d_{crest}$). It is apparent from Figure 43 that neither of the suggested correlations holds true as far as these eight maximum impacts (L1 to L4; S1 to S4) are concerned. Although the dataset is very small, an argument can be made for the importance of predicting exactly these high force impacts. It is nevertheless interesting to see that some of these values correspond well between the two scales. Later, these parameters are included in the force comparison resulting after the bore evolution analysis (see Section 4.2.3.).

Table 18: Layer thickness, bore velocity, instantaneous discharge, and peak impact force for the four highest impacts at each scale. Small scale data Froude-upscaled to 1:4.3.

	Peak layer thickness	**Average bore velocity**	**Instantaneous discharge**	**Peak impact force**
	d_{crest} [m]	$U_{b,avg}$ [m/s]	q_{inst} [m^3/s/m]	F [kN/m]
L1	0.33	2.58	0.85	4.59
L2	0.37	3.88	1.44	4.46
L3	0.50	2.85	1.41	3.96
L4	0.38	2.79	1.06	3.93
S1	0.73*	2.62	1.91*	4.92
S2	0.37	3.94	1.45	4.74
S3	0.44	3.37	1.49	4.63
S4	0.44	2.95	1.29	3.79

** The layer thickness for S1 includes a substantial residual water layer on the promenade (approximately 17 cm in 1:4.3 scale)*

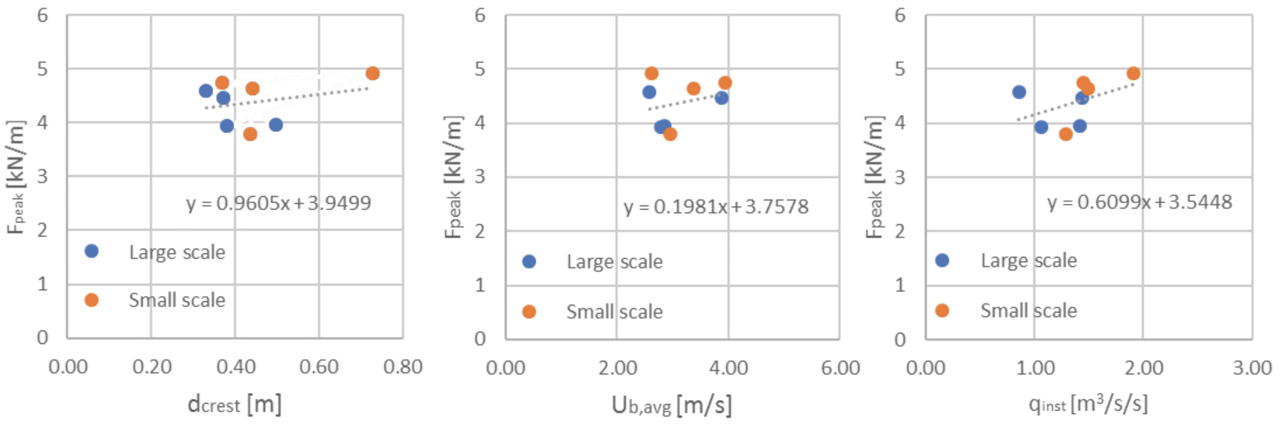

Figure 43: Scatter plot of peak impact force compared to peak layer thickness at dike crest (d_{crest}; left), average bore front velocity over the promenade ($U_{b,avg}$; center), and instantaneous overtopping discharge at dike crest (q_{inst}; right). Values for these parameters are presented in Table 19.Small scale data is Froude-upscaled to 1:4.3.

4.2. Pre-impact flow evolution

Analysis of the flow evolution for the four highest impact events outlined in Section 4.1.2. is beneficial for understanding what mechanisms that are responsible for causing these events, and to identify features and characteristics that may have contributed to the high loads exerted on the wall. To enable this, data from the laser scanner and side view camera (large scale) and a side-mounted camera (small scale), as well as the force-time signal evolution from the load cells at both scales, was synchronized and analysed. The goal was to identify common traits in the force-time signal, the bore evolution before and during an impact, and the overtopping flow layer thickness and bore front velocity. This is supplemented by comparisons with the three elementary loading processes (ELPs) outlined by Lafeber et al. (2012b) – see Section 2.5.1.

4.2.1. Large scale impacts

Wave catch-up

For three of the four largest impacts (L1, L3 and L4), an almost identical overtopping mechanism was observed from the laser scanner and video recording. It is believed that this contributed to the high loads on the wall recorded during those events. Figure 44 illustrates the pre-impact sequence for L1 as observed by the laser scanner, and similar plots are available for L3 and L4 in Appendix 11.

Two distinct wave crests can be observed propagating over the foreshore towards the dike (Figure 44 – a. to c.). The faster propagating wave crest eventually 'catches up' to the slower propagating one, which occurs before the impact with the wall. The overtopping process begins with the first wave impacting the front of the dike slope (Figure 44 – d.) and subsequently overtopping it (Figure 44 – e.), quickly followed by the second wave. The initial impact of the former with the dike front further facilitates the catch-up to occur. Moreover, a more efficient overtopping process for the second wave seems to result from this, where less energy is dissipated due to the lack of a direct impact with the dike front. This is evident from the estimated velocity obtained by the time each bore needed to propagate between the first two promenade-installed wave gauges (0.45 m apart, see also Appendix 3), which was approximately 2.45 m/s for the first one and 3.86 m/s for the second one. An exact point of 'catch-up' is difficult to define due to the turbulent nature of the flow, but for L1, L3 and L4 this occurred sometime after the overtopping of the dike crest, but before the impact with the wall (approximately x = 0 to 1.5 m in the LCS reference system described in Section 3.1.2.).

As the catch-up occurs (Figure 44 – f.), the initial overtopping volume (related to the first wave) appears to be accelerated by the large volume of faster propagating water body resulting from the efficient overtopping of the second wave. The slightly higher promenade-averaged velocity (2.58 m/s) observed from the point of initial

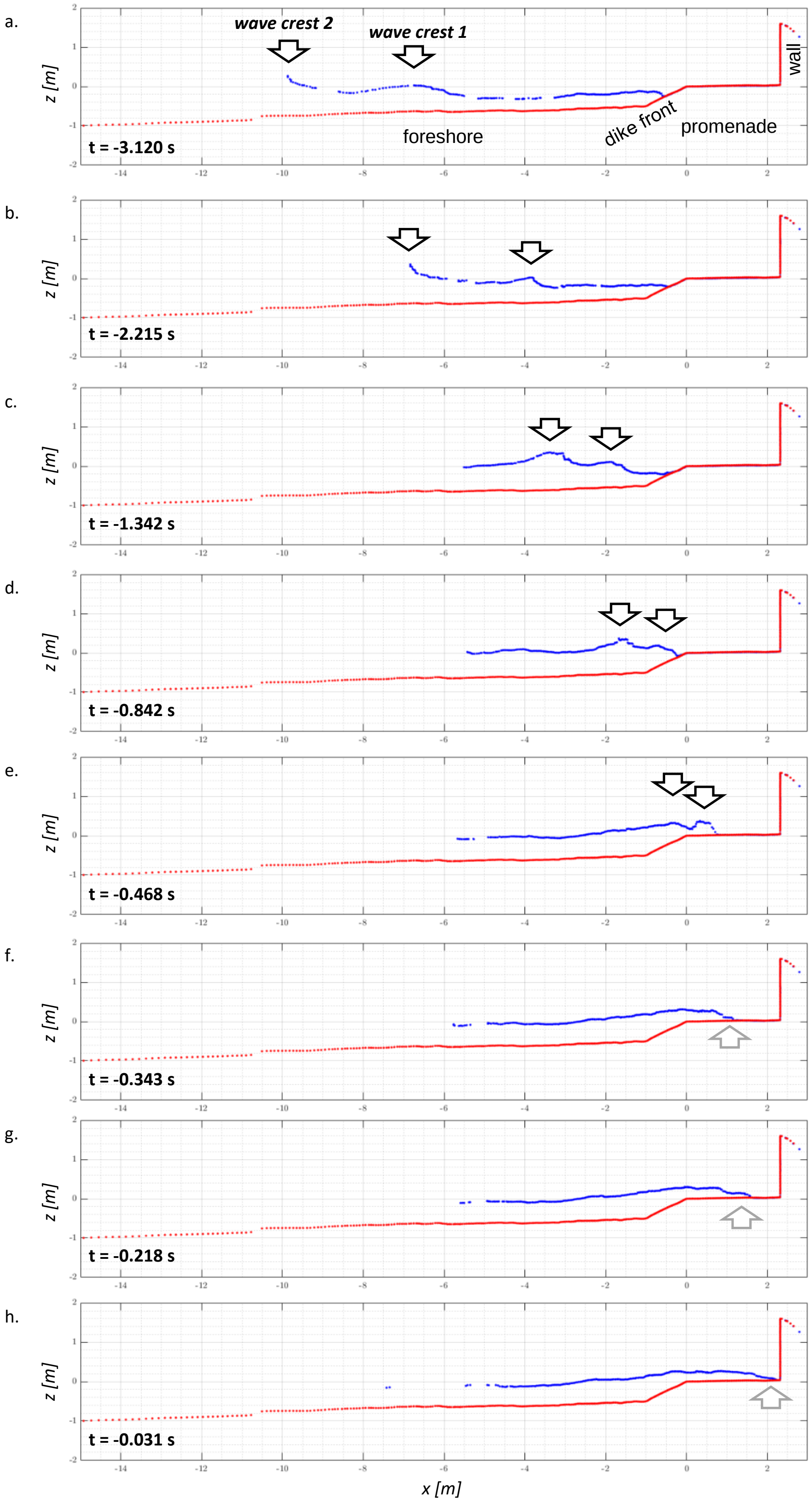

Figure 44: Profile of the propagation and overtopping of the two waves that caused the largest impact force (L1). Blue line indicates the water surface, red line – the model profile. The black arrows (a. to e.) indicate the two distinct wave crests. The grey arrows (f. to h.) indicate the accelerated bore front of the first overtopping wave. Profile obtained from laser scanner recording. Timesteps related to t = 0 s corresponding to the moment of impact (t = 2707.14 s). Coordinates in LCS.

overtopping to the moment of impact seems to support this. The overtopping volume related to the first wave then propagates towards the wall in the form of a relatively shallow bore front (Figure 44 – f. to h.; grey arrow). It is this part of the bore that impacts the wall first, followed by the rest of the water body, which can be of comparatively substantial thickness.

Figure 45 shows a different perspective of the pre-impact stage for L1, captured by the side view camera at the promenade (see Section 3.2.6.). Here again, the two waves are seen during the process of overtopping the dike (Figure 45 – a.), where the catch-up has not yet occurred. The accelerated bore tip after the second wave overtops the dike can be seen in Figure 45 – b., where the extended tip of the bore is observed propagating towards the wall. The bore is relatively uniform and the impact is not disturbed by any significant reflected bores (Figure 45 – c. and d.). The force time signal for L1 exhibited a dominant *dynamic force peak* (Figure 45 - right) and a relatively high peak ratio F_1/F_2 of 2.3.

It seems that the sharp initial force peak can be attributed to both the velocity and the uniformity of the bore front. Although a bore and not a traditional crested breaking wave, the concept of ELPs can still be applied. ELP1 – *Direct impact*, as defined by Lafeber et al. (2012b) – see Section 2.5.1., can be related to the initial impact between the bore front and the wall, followed by ELP2 – *Building jet,* related to the change of momentum the fluid experiences at the wall interface. The high degree of air entrainment will lower the compressibility of the air-water mixture. ELP3 – *Pulsating gas* pocket, is not observed in this type of impact as described by Lafeber et al. (2012b), although it could be argued that it is included in the smaller air cavities (bubbles and smaller air pockets) during the initial impact. The comparatively high difference in magnitude between the *dynamic force peak* and the *quasi-static force peak* could likely also be attributed to the relatively low peak flow layer thickness at the dike crest (0.33 m) and resulting instantaneous overtopping discharge (0.85 $m^3/s/m$). It's also worthwhile pointing out that this overtopping mechanism appears to relate to the *dynamic bore impact* of Streicher et al. (2016), but this is not always the case as can be seen from the force-time signal of L4. Regardless of the classification, the time signal of L4 still shows strong similarity to L1 and L3 (Figure 41 in Section 4.1.2.), where similar a very similar overtopping mechanism was observed.

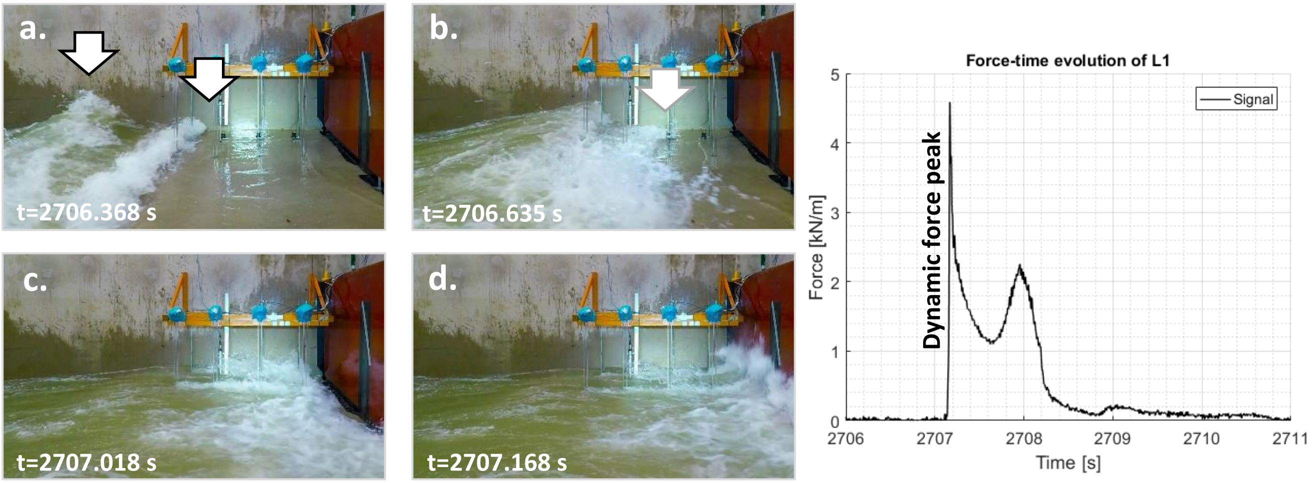

Figure 45: Impact sequence for L1 (left) and resulting force on the wall (right). The first wave is overtopping the dike, closely followed by a second wave (a.); after catch-up, a shallow bore tongue extends, accelerated by the overtopping flow of the second wave (b.); the bore is uniform and the impact of the bore front is qualitatively similar to ELP1 (c.); after initial impact (ELP1), the run-up stage resembles ELP2, and both cause the large initial force spike (d.; right).

Wave collision

Unlike impacts L1, L3 and L4, there was no wave catch-up observed before L2 occurred. Instead, a single wave can be seen propagating along the foreshore towards the dike (Figure 46 – a.). At the same time, a small body of water, likely a previous wave, is observed reflecting off the dike front (Figure 46 – b.). The incoming wave breaks violently just before reaching the dike front (Figure 46 – c.), and it is believed this is at least partially caused by the collision with the small reflected wave. The post-overtopping flow is highly turbulent, and a large volume of water of significant layer thickness (0.37 m and 1.44 $m^3/s/m$, respectively; both measured at the dike crest until moment of impact) propagating along the promenade (Figure 46 – d. and e.).

Figure 47 shows the post-overtopping flow as recorded by the side view camera. The post-overtopping bore is not uniforms as was observed for L1 (Figure 45 – left), L3 and L4 (Appendix 11). Instead, the bore front appears to be broken up into multiple spays of water. This can be related to the shape of the force-time signal, where no single dominating *dynamic force peak* can be discerned, but is instead observed to rise in a stepwise manner. The force-time signal is dominated by the *quasi-static force peak*, which is caused by the subsequent run-up and down-rush of the overtopping flow along the wall (Chen et al., 2014). The impact falls well within the *quasi-static/down-rush bore impact* category (Streicher et al., 2016).

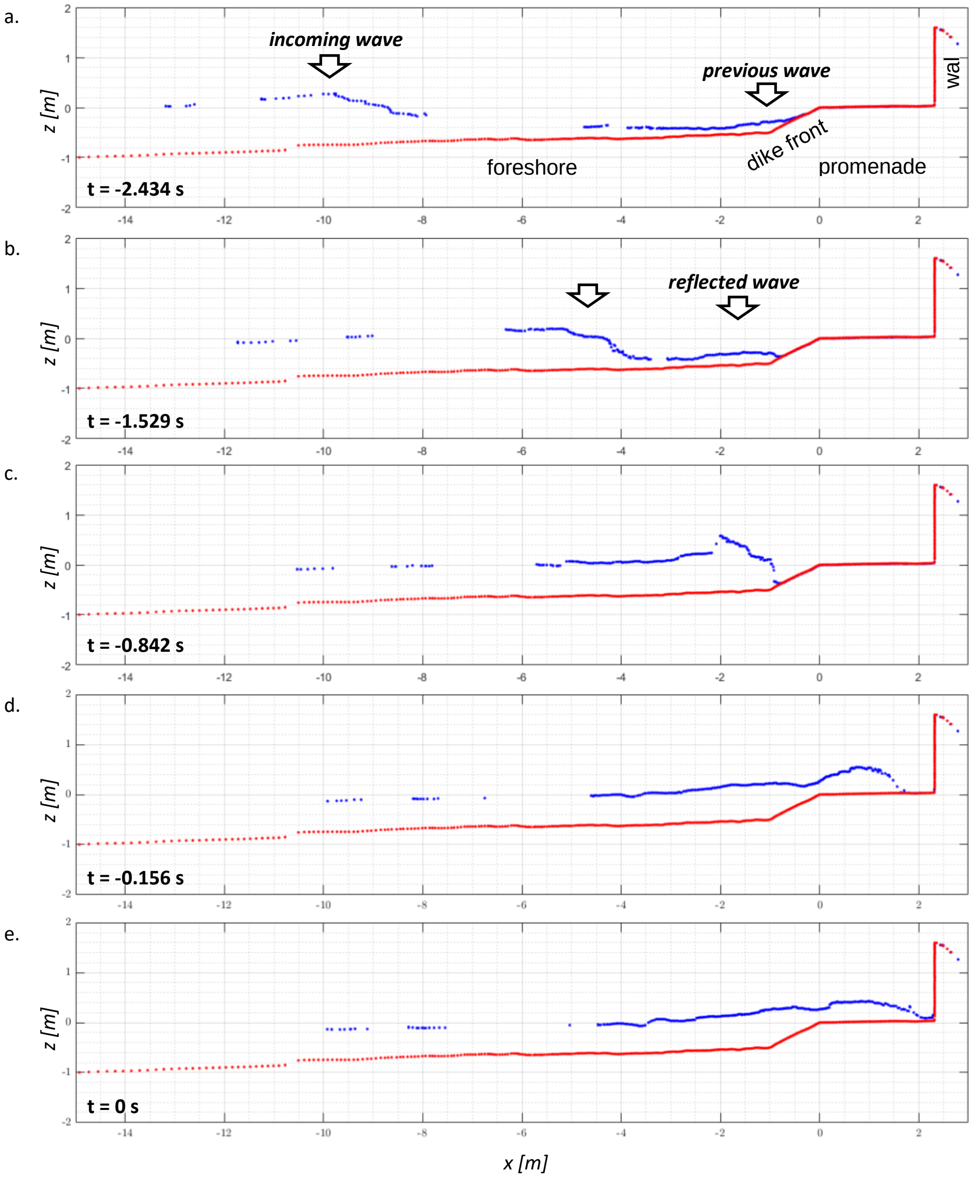

Figure 46: Profile of the propagation and overtopping of the wave that caused impact L2. Blue line indicates the water surface, red line – the model profile. The black arrows (a. and b.) indicate an incoming wave and a previous wave reflected off the dike front. The two collide (c.) and the incoming wave overtops the dike (d. and e.). Profile obtained from laser scanner recording. Timesteps related to t = 0 s corresponding to the point of impact (t = 784.01 s). Coordinates in LCS.

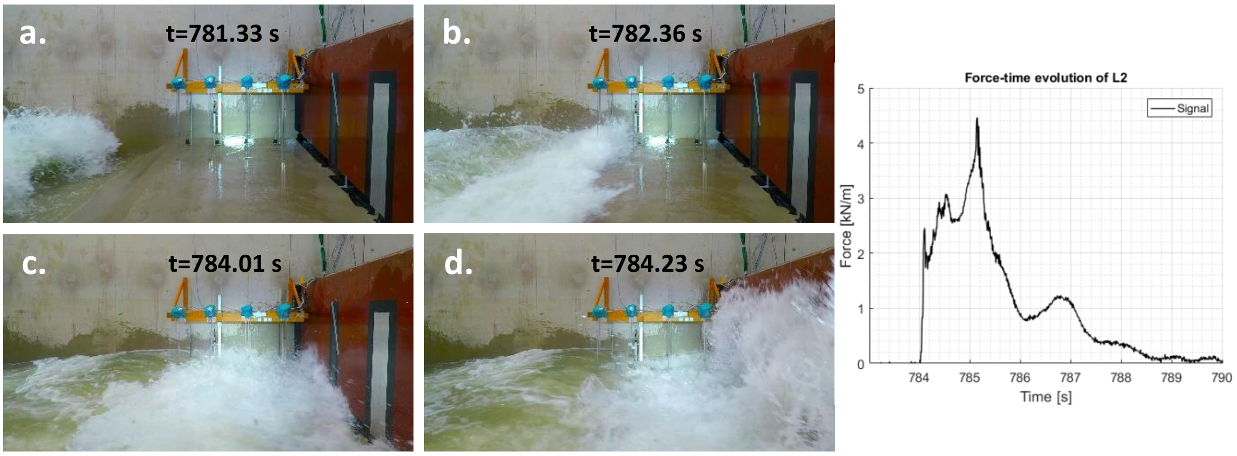

Figure 47: Impact sequence for L2 (left) and resulting force on the wall (right). The incoming wave breaks before reaching the dike (a.), then overtops it (b.); the post-overtopping flow is highly aerated and turbulent (c.); run-up on the wall, note the substantial layer thickness of the incoming wave (d.), which contributes to the dominant quasi-static force peak (right).

The lack of a uniform bore front is possibly related to the lower influence of the *dynamic force peak*, and subsequently of the *Direct impact* ELP (peak ratio for this impact was 0.69 after Streicher et al. (2016); see also Table 17 in Section 4.1.2.). The involvement of all ELPs is expected to be highly variable both between individual impacts and between scales (including the additional considerations introduced by Lafeber et al. (2012a), see Section 2.5.2.). However, whether these could affect the dominant *quasi-static force peak* is debatable.

As previously mentioned, please refer to Appendix 11 for the laser scanner recorded timesteps for impacts L3 and L4.

4.2.2. Small scale test

The small scale pre-impact analysis is based on a side-mounted camera looking through the transparent walls of the flume towards the promenade, and the load cell data for the impact forces on the impacted wall (see Sections 3.3. and 3.5.). Both common attributes and differences were found in comparison to Section 4.2.1., however, these are summarized in Section 4.2.3.

Sequential overtopping

With regard to S1, a unique interference pattern was observed where three consecutive waves impacted the wall in short succession, and with increasing magnitude. The third wave produced the high recorded peak impact force (S1), and the pre-impact mechanism observed is termed ‘sequential overtopping’. It was observed that the residual water layer from the previous two impacts did not have sufficient time to drain (Figure 48 – a.), which enabled the third wave to overtop the dike without directly impacting the dike front. Instead, it broke roughly in the region of the dike crest, appearing similar to a plunging wave (Figure 48 – b.). The breaking of the third wave appears to be caused by both the structure (dike front causing decreasing depth) and the reflected previous (second) wave. The overturning crest subsequently ‘slid’ over the substantial residual water layer present on the promenade (approximately 17 cm – upscaled to 1:4.3) and a turbulent and highly aerated flow impacted the wall (Figure 48– c. and d.). Since the wave breaking did not occur in immediate proximity to the wall, no entrapped air pocket was observed forming at the water-structure interface. Nevertheless, large air bubbles are clearly present within the water body, as can be seen in Figure 48 – d, attributed to the wave breaking process.

This ‘sequential overtopping’ impact sequence was not observed for any of the other seven highest impacts that were analysed. Furthermore, the corresponding waves in the large scale test were found to produce an almost identical sequence of impacts. However, the impact mechanism for the third wave differed significantly. In the large scale scenario, the second wave had ample time to drain off of the promenade, and the subsequent

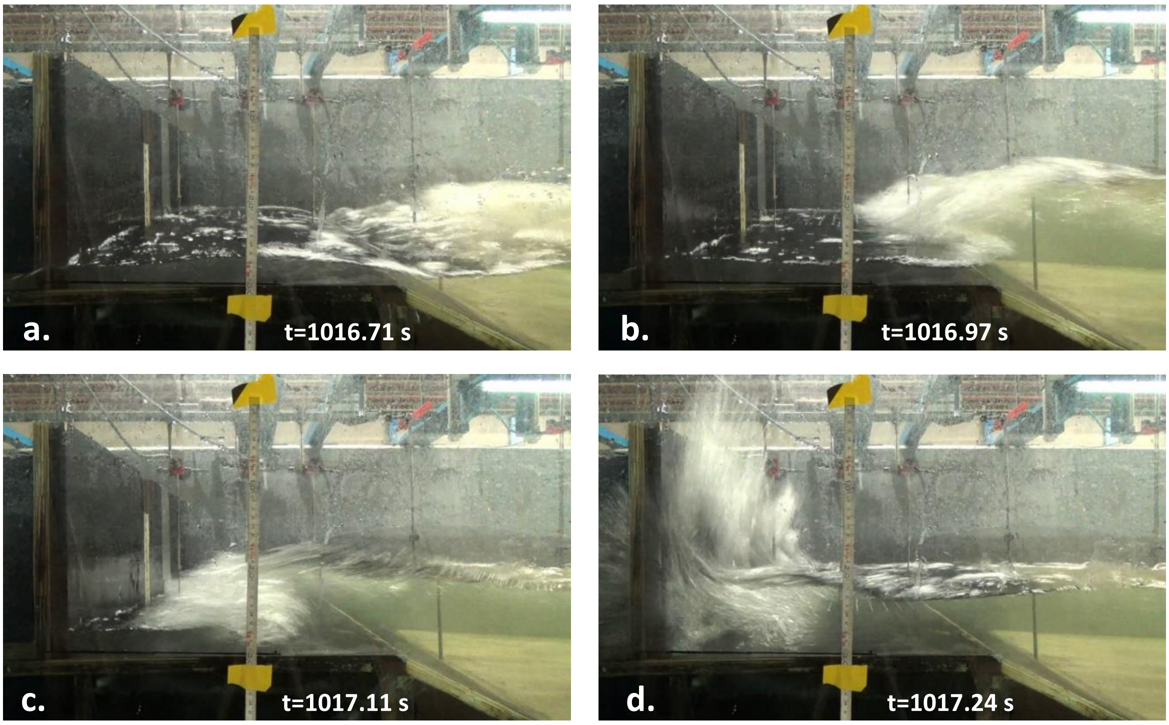

Figure 48: Impact sequence for S1. Timesteps in model scale.

wave impacted the dike front directly, resulting in much of its energy being dissipated in the process. Thus, the maximum impact at the wall in large scale was still recorded for the third wave, but was only 21% of the corresponding peak force in small scale, see Figure 49. Note also how the force-time evolution differs between the third impact in small and large scale. For the former, a dominant first *dynamic force peak* is observed, which was necessitated by the fast and uniform bore. Note also that in such cases, the high residual water layer raises the location of the impact heightwise.

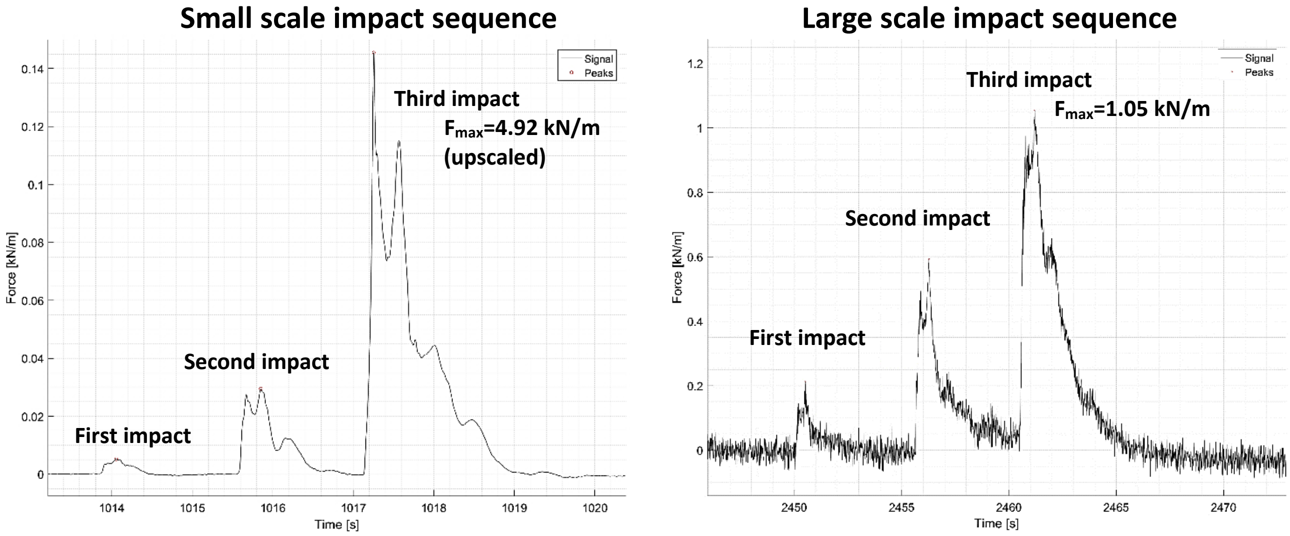

Figure 49: Sequential overtopping impact sequence for small scale (left; values in 1:25 scale) and large scale (right; values in 1:4.3 scale). Note that the axes' scales differ.

Regarding ELPs, the conclusions are identical to the ones presented for the *dynamic bore impact* classified large scale impacts (see Section 4.2.1.). The question is raised whether the overtopping mechanism as described for S1 can occur in the large scale tests and produce similar in magnitude and force-time evolution impact events. A relatively similar large scale impact event (L5) was mentioned in Section 4.1.2., which however did not correspond directly to the impact mechanism observed for S1. Furthermore, the wave breaking for L5 was close to the wall, causing entrapment.

Wave catch-up

For impacts S2 to S4, again the pre-impact mechanism observed was wave catch-up, as was the case for several large scale impacts (L1, L3 and L4). Once again, a faster propagating wave was observed 'catching up' up to a slower one. For S4 this occurred approximately at the dike crest, which corresponding well to the pre-impact flow mechanism observed for the aforementioned large scale impacts. On the other hand, the catch-up for S2 and S3 was observed to occur earlier. It is unclear whether this could be considered a predominantly a model or a scale effect. Some notable differences were observed between the three small scale impacts.

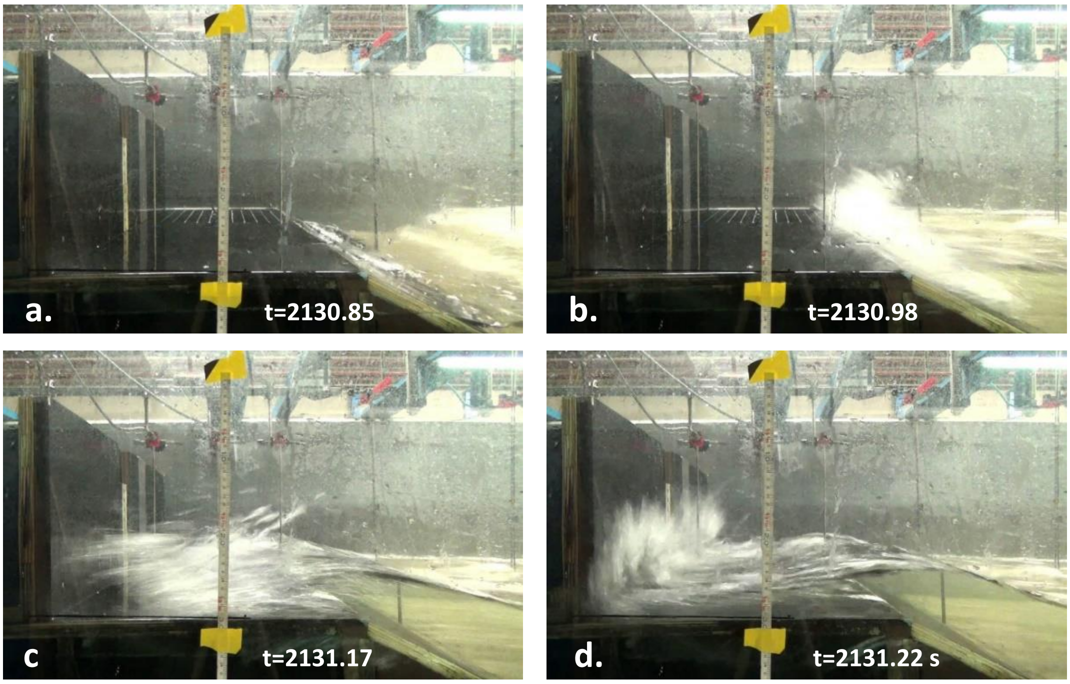

Figure 50: Impact sequence for S2. Timesteps correspond to 1:25 scale. Note the wave catch-up visible in the right part of the first timestep (a.).

For S2, again a very small wave is reflected off the dike front (Figure 50 – a.), then subsequently collides with the now merged (due to catch-up) incoming wave (Figure 50 – b.). This mechanism is also very similar to the one described for L2 (wave collision), and the subsequent violent breaking of the incoming wave and overtopping mechanism also appear qualitatively and even quantitatively similar (see Section 4.2.3.). In fact, the force-time signal evolution for these two impacts (L2 and S2) is almost identical (see Figure 52 – L2 and S2 in Section 4.2.3.), which correlates well with the pre-impact similarities observed. The lack of a large (in relative terms) *dynamic force peak* component in the S2 force signal is again attributed to the scattered, non-uniform post-overtopping flow front that impacts the wall first (Figure 50 – c.), before the subsequent overtopping flow (Figure 50 – d.). Note that due to the clear flume walls and position of the camera, the non-uniformity (visible splashes) of the bore is more clearly distinguishable.

S3 followed a similar pre-impact mechanism to S2. A catch-up is observed at an almost identical spot before the dike front. One notable difference is the lack of a collision with a reflected wave, but the post-overtopping flow again lacked a uniform front, with individual splashes instead impacting the wall first. The force-time evolution for S2 also shows certain similarities to that of S3, as could be observed in Figure 41.

The fourth largest impact (S4) also involved a three-wave interaction, however, this differed from the mechanism described for S1. Instead, the overtopping process resembled the one observed for the large scale impacts L1, L3 and L4, where efficient overtopping was facilitated by the first wave overtopping the dike front. In the case of S4, a very small initial wave overtopped the dike first, quickly followed by the previously described slower and faster propagating waves (wave catch-up). The latter therefore negated a significant impact with the dike front, which resulted in a fast propagating uniform bore impacting the wall. These bore features correspond to the slightly larger *dynamic force peak* observed in the force-time signal. Furthermore, similarities in the pre-impact evolution of S4 when compared to L3 and L4 extend to the loads on the wall. The force-time signal for these three impacts is very similar in both evolution and in magnitude, suggesting that this pre-impact mechanism is likely well represented by the small scale model. A comparison between L3 and S4 can be found in Figure 52 – right, in the following section. Timesteps of the pre-impact flow evolution for S3 and S4 is given in Appendix 12.

4.2.3. Comparison between the two models

At both scales, the pre-impact wave interaction mechanism and post-overtopping flow evolution appear to be related to the highest impact force events' force-time signal evolution. It stands to reason then that a good replicability of the former mechanisms should result in an accurate representation between a scaled down model and its large scale counterpart. In the current comparison, flow similarities between the two scaled models were apparent, but there were also some notable differences. A summary of the three interference patterns observed for the eight impacts analysed is given in Table 19.

Table 19: Summary of pre-impact wave interaction mechanisms observed for the four highest impacts at each scale.

Impact	Catch-up	Collision	Sequential overtopping
L1	Yes	No	No
L2	No	Yes	No
L3	Yes	No	No
L4	Yes	No	No
S1	No	Yes	Yes
S2	Yes	Yes	No
S3	Yes	No	No
S4	Yes	No	Some similarities

Out of the four highest impacts at their respective scales, the most common wave interaction pattern was the so-called *wave catch-up*. It was observed (with some variations) in three out of four impacts at each scale (L1, L3, L4, and S2, S3, S4). In comparison, the point of catch-up seemed to occur slightly earlier in the small scale tests, although the lack of a laser scanner and the differing camera setup in that test makes a definitive conclusion more difficult. It seems that another mechanism that the wave catch-up may facilitate (provided catch-up occurs after the dike crest) relates better to the resulting high impact forces. This is the tendency for the second (faster propagating) wave to negate a direct impact with the dike front. As was shown for L1 (Section 4.2.1.), this likely relates to its resulting higher post-overtopping velocity. It seems that in the small scale test, the setting for avoiding a direct impact with the dike front is also linked to the high impact force events. However, the conditions under which these occurred varied for S4, and even more so for S1. The dominant peak in the force-time signal appears to be governed at least in part by the uniformity of the post-overtopping bore front – the more uniform the bore, the larger the initial *dynamic force peak* and vice versa. This is illustrated in Figure 51 – right for impact L4. However, naturally this factor should not be viewed in isolation but within the context of other relevant processes and parameters.

Only one of the impacts was caused by a single large propagating wave – L2, but still, a wave interaction mechanism termed *wave collision* was observed. A small reflected wave aided in the breaking of the incoming wave before the dike front, which caused a non-uniform, scattered water spray bore front to impact the wall first. Furthermore, this overtopping mechanism was observed in the second largest small scale impact (S2), and the remarkably similar force-evolution signals (Figure 52 – left) seem to confirm that the inverse of the uniform front–high dynamic force peak relation is also true. This is further supported by the similar in force-time and pre-flow evolution impact S3 (see Figure 51). Notable is that L2 and S2 were high velocity impacts ($U_{b,avg}$) with very similar flow depths d_{crest} (see Table 20). Mostly though, comparing the difference in peak impact force (5%)

and estimated instantaneous overtopping flow discharge (q_{inst}; 0.8 %), even if interpreted as a scale effect (which naturally could be debated), appears to be negligible (see also Figure 52 – left).

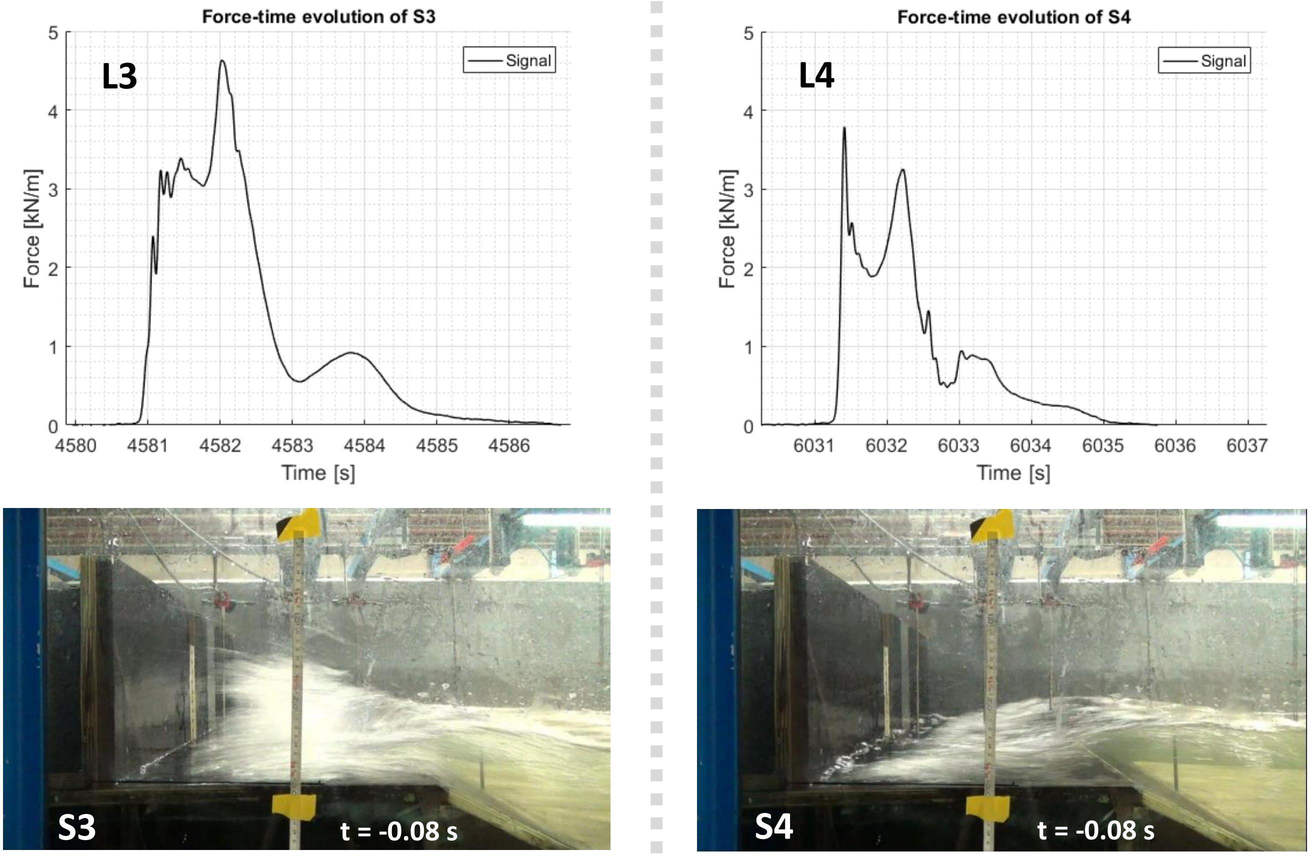

Figure 51: The force-time signal and freeze-frame for impacts S3 (left) and S4 (right). Frames captured at corresponding moments before the respective impact occurs. Note the difference in the bore front uniformity and the corresponding change in dominant impact peak.

Table 20: Comparison of overtopping flow parameters for impacts with comparable force-time signal (given in Figure 52) and pre-impact flow evolution. Small scale data Froude-upscaled. The blue rectangles mark the instantaneous overtopping discharge q_{inst} and F_{peak}, which have been shown to be related (Van Doorslaer, et al., 2017).

	d_{crest}	$U_{b,avg}$	q_{inst}	F_{peak}
L2	0.372	3.88	1.44	4.46
S2	0.369	3.94	1.45	4.74
S2/L2*100-100 [%]	**-0.8**	**1.6**	**0.8**	**6.2**
L3	0.497	2.85	1.41	3.96
S4	0.436	2.95	1.29	3.79
S4/L3*100-100 [%]	**-12.3**	**3.7**	**-9.1**	**-4.2**

The *sequential overtopping* process was observed only for S1. This basically enabled the same efficient overtopping by avoiding a direct impact with the dike front for at least one of the waves. Some similarities could be drawn to the overtopping mechanism observed for S4, and in both cases, a breaking wave was formed, and the resulting uniform bore caused a sharp first peak. However, in the case of S1 this was due to a collision with a reflected wave. The waves corresponding to S1 at large scale caused significantly lower impact forces on the wall due to differences in the return flow on the promenade. Furthermore, a large residual water layer was observed before S1 occurred. This impact mechanism appeared to not scale between the two models, as the corresponding large scale impact was shown to differ significantly in flow evolution and subsequently in peak force magnitude. However, it is unclear whether this is due to scale effects or differences in the propagation of the incoming waves along the foreshore.

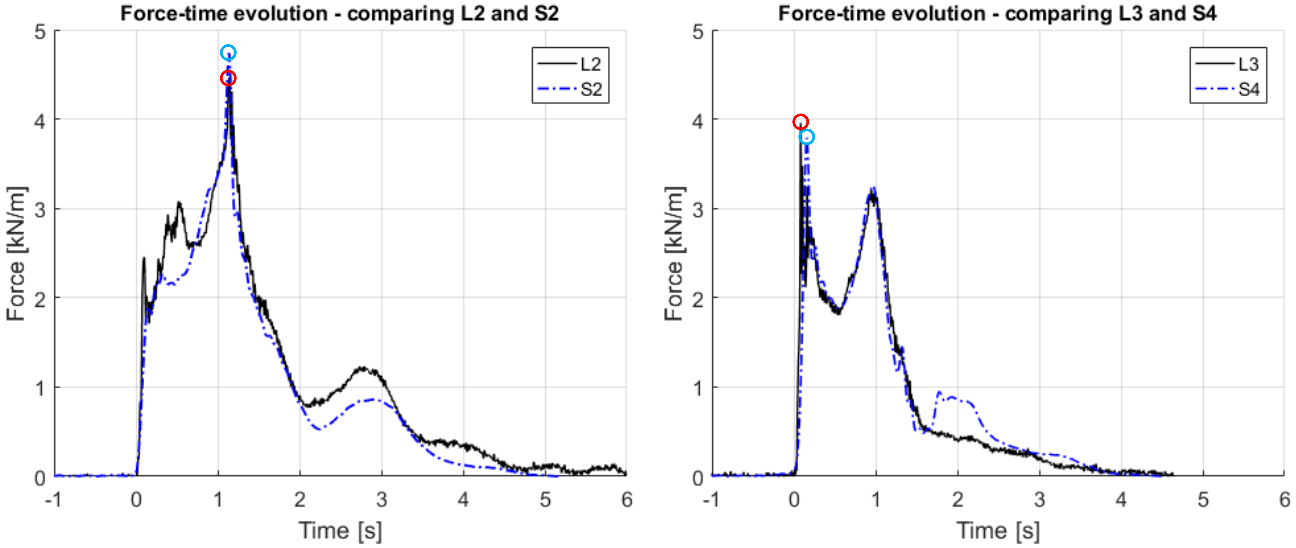

Figure 52: The similarities in pre-impact flow evolution caused very similar loads on the wall. Comparison of the force-time signal evolution for L2 and S2 (left) and L3 and S4 (right). Force peak marked in blue (small scale) and red (large scale). Impacts aligned according to t_{impact} = 0 s. Small scale data Froude-uspcaled to 1:4.3. Force data from the load cells.

With regard to the overtopping mechanism and resulting loads on the wall, S4 resembles more the L3 and L4 large scale impacts. This is especially true for the former (L3), as can be seen from Figure 52 - right. As noted above, these events were similar in their pre-impact flow evolution, which further points towards a valid relation between the overtopping mechanism and the resulting force-time signal evolution. Due to their similarity, these mechanisms were also compared in Table 20 and Figure 52 – right. These impacts exhibit a (slightly) larger *dynamic force peak*, where the Froude scaling effects due to difference in air entrainment and detrainment (Blenkinsopp & Chaplin, 2011), and variability of elementary loading processes (Lafeber et al., 2012b) are generally expected increase. Although S4 is lower in absolute impact force peak magnitude (4.2%) than S3, it achieves this for a relatively lower instantaneous discharge (9.1%). Even though this difference could be perceived as scaling bias in the impact force, it is rather small, especially when considering the accuracy of the measurement techniques and the inherent variability of wave impacts in general. It is possible therefore to interpret this result as not showing a definitive scaling bias.

4.3. Distribution of impact types

The method proposed by Streicher et al. (2016) for classifying bore impacts based on their force-time signal evolution was outlined in Section 2.2.1. This method relates the ratio of the *dynamic force peak* (F_1) and the *quasi-static force peak* (F_2), and classifies impacts as either *dynamic bore impact* (F_1/F_2>1.2) or *quasi-static/down-rush bore impact* (F_1/F_2<1.2). This classification was already applied to the highest four impacts at each scale in Section 4.1.2. Here, the same classification was conducted for the highest 10% peak impact forces recorded at each scale. This equated to 53 impact events at large scale and 57 at small scale. Note that the 10% limit is related to the total number of discernible impact events at each scale rather than applying the matching threshold used earlier in Section 4.1. This was done due to the more similar lower magnitude threshold equating to 1.43 kN/m (53rd impact at large scale) and 1.59 kN/m (57th impact at small scale). Furthermore, applying the high pass threshold of 0.13 kN/m to the small scale tests did not appear to introduce a large variation in the results. Further elaboration on this can also be found in Appendix 13.

With regard to outlining scale effects, the peak ratio classification can prove a quick and useful tool for assessment of the performance of the two models. Figure 53 shows how the classification of the highest 10% of impacts between the two scales, which appears to be similar.

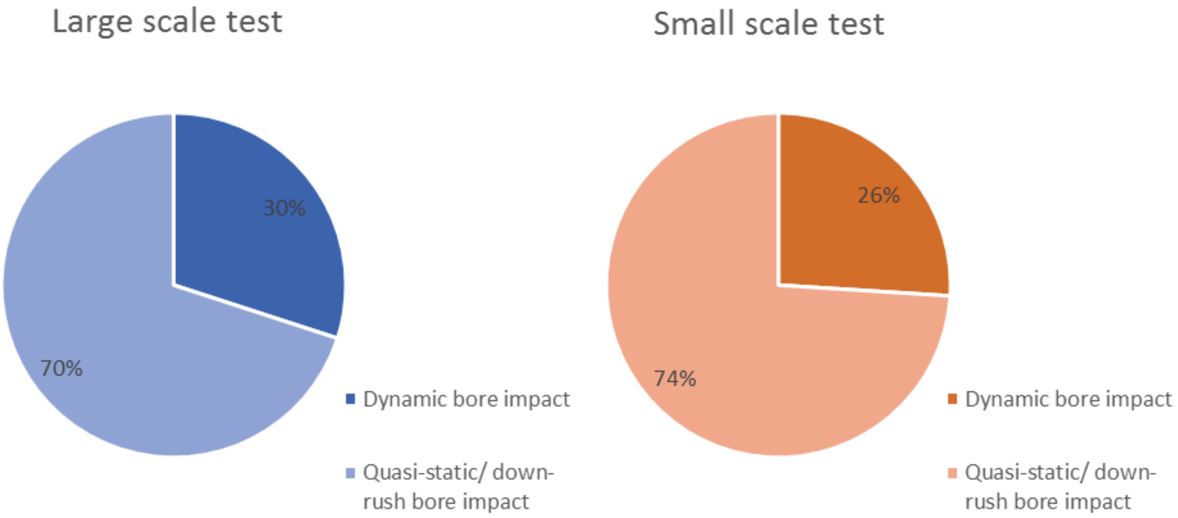

Figure 53: Distribution of impact types for the 10% highest impact force events at both scales following the classification of Streicher et al. (2016).

Streicher et al. (2016) defined a force peak relation threshold of 1.2 times the second peak. Another classification based on the force peak ratio was proposed by Kortenhaus & Oumeraci (1998) for deep water wave impacts. Although the latter is not directly applicable in the present case, Kortenhaus & Oumeraci (1998) used comparatively larger values. Therefore, a sensitivity analysis was conducted to assess the effect changing this parameter has on the classification distribution between the two scales, with values ranging from 1.0 to 2.4 (Appendix 13). The bore impact type classification distributions for several values is shown in Figure 54. The distribution of impact types between the two test scales remains very similar.

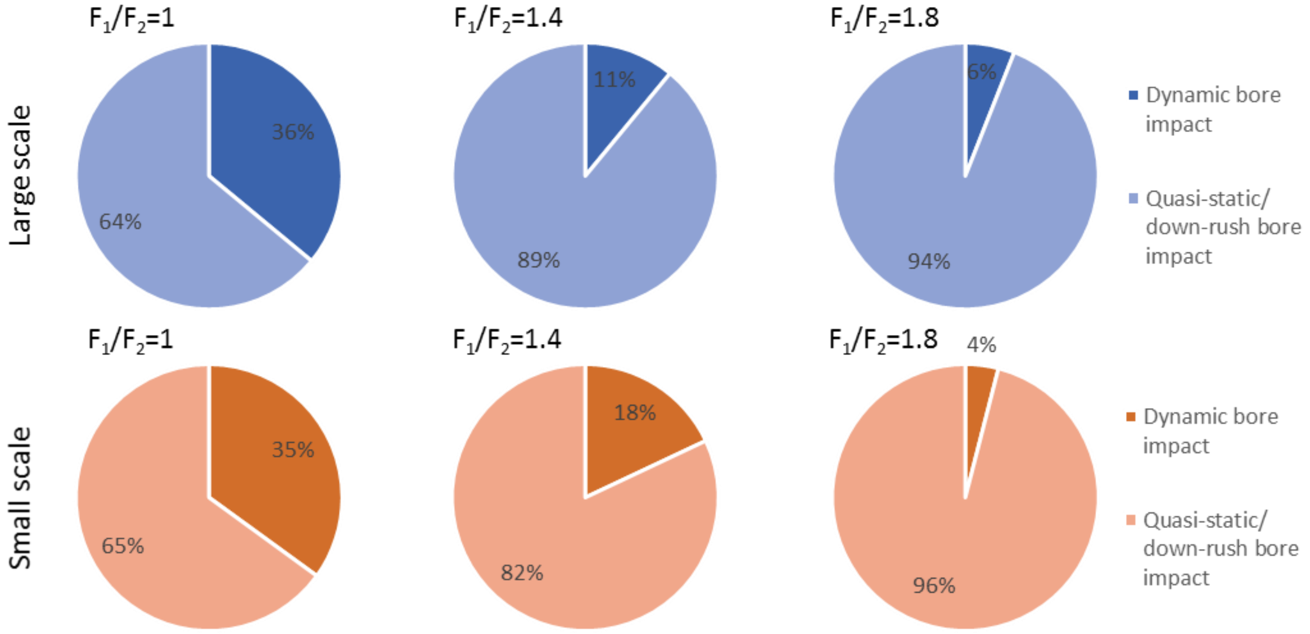

Figure 54: Sensitivity analysis of the force peak ratio relation to the bore impact classification proposed by Streicher et al. (2016) between the two tests (small and large scale). A similar relation is observed between the two scales.

Although Figure 53 and Figure 54 show a similar distribution between the bore impact classifications after Streicher et al. (2016), it was determined that this is not the case for the largest peak force events. Figure 55 shows the impact classes of the largest 10 impact events at both scales. The abundance of quasi-static/down-rush bore impacts in the small scale test is not visible in its large scale counterpart. This discrepancy in the results leads to the conclusion that the 1:25 model, while achieving similar force peak intensities might not be replicating the impact mechanisms responsible for these. Bearing in mind the reasonable similarity between the two models, this can at least partially be attributed to scaling bias.

It was also noted in Section 4.1.2. that at large scale, three entrapped air pocket impacts out of the 10 largest were observed versus only one such impact at small scale. The results in Figure 55 do support this, and the four air pocket impacts (L5, L7 and L8; S9) are classified as *dynamic bore impacts*. The lack of more of these impacts at small scale does negate a possible source of scaling bias, which are the entrapped air impatcs.

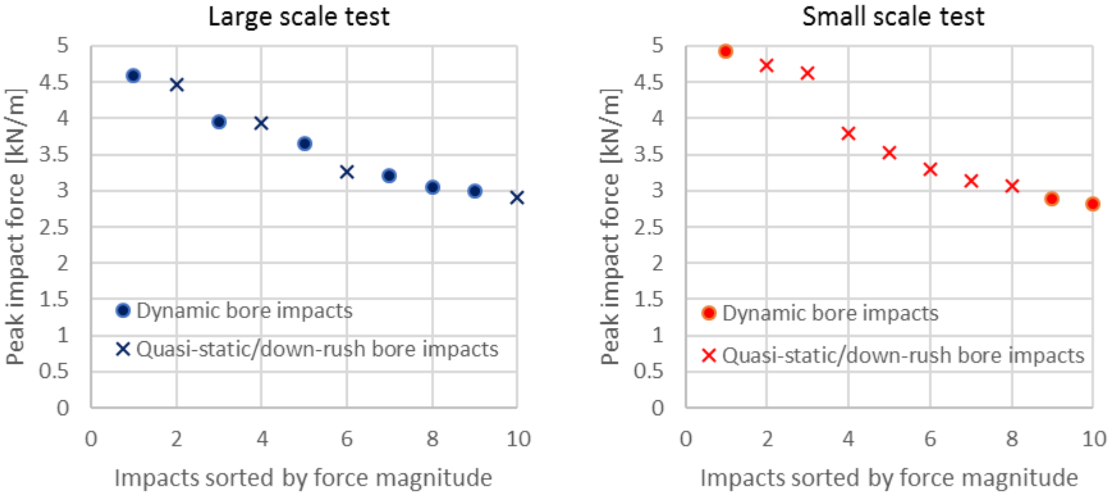

Figure 55: The 10 highest impacts classified as either dynamic or quasi static/down-rush bore impacts after Streicher et al. (2016). Large scale (left) and small scale (right) test data. Note the discrepancy in the type of bore impacts between the two models. Peak impact force measurements from load cells. Small scale data Froude-upscaled to 1:4.3.

Furthermore, the type of the dominant force peak is of importance. A *dynamic force peak* is associated with a high rise time and short duration (Bullock et al., 2001; Van Doorslaer, et al., 2017), and affects mainly structural elements with a high natural frequency (Chen, 2016). Therefore, in a case where no additional large scale model is available for comparison purposes, such a discrepancy in the type and classification of the impact events could lead to wrongful conclusions with regard to e.g. design considerations.

5. Conclusions and Rrecommendations

5.1. Conclusions

The first aim of this research was to determine the extent of Froude similitude induced scaling bias in hydraulic physical models related to a post-overtopping flow impact. For this purpose, two tests conducted at similar setups, one at 1:4.3 scale and another at 1:25 scale, were compared in terms of peak impact forces and impact mechanisms. To necessitate the comparison, the small scale test results were upscaled to 1:4.3 following Froude law, which results in a relatively low scaling factor λ=5.81. It was determined that as a whole, the extreme small scale impact events were somewhat larger than their large scale counterparts. This was especially prominent when comparing the largest four force peak impact events on the wall, where the difference was about 7% on average. While this seems to fit the narrative of scaling bias, conclusions should be conservative in attributing this solely to the latter, since the contribution of model effects or random variability cannot be excluded. Also notable was the discrepancy in the occurrence of entrapped air pocket impacts between the two models. While such events were observed in the large scale test, constituting three of the ten largest impacts, their prevalence was lower (one out of ten) in the small scale model, negating a potential source of scaling bias.

Further analysis focused on the pre-impact flow evolution in aims of outlining the differences and/or similarities between the two scales. This comparison was again based on the largest four impacts, and it was found that at both scales wave-to-wave interactions largely govern the pre-impact flow evolution and resulting force-time signal at the wall. Three interaction mechanisms termed *wave catch-up*, *wave collision*, and *sequential overtopping* were observed. A combination of these can also occur within a single impact event. The conclusion is reached that some of these mechanisms scale well between the two models, suggesting a good performance of the small scale test in replicating large scale conditions.

Wave catch-up results in larger overtopping events, facilitated by both the enhanced severity of a two-wave flow, and the possibility for enabling of a more efficient overtopping mechanism when the second wave does not impact the dike front directly. Depending on the characteristics of the bore as it propagates along the promenade, these impacts could either result in *dynamic force peak* dominance (uniform bore front), or a *quasi-static force peak* dominance (non-uniform bore front resembling scattered water spray). Although *wave catch-up* tended to occur earlier for the small scale impact events, it is likely that the foreshore variation between the two models have contributed to this. A *wave collision* interference pattern is caused when a reflected and incoming wave(s) collide, which was observed to cause a breaking of the latter. Depending on where the collision occurs, the resulting bore front can again be either uniform (collision at dike crest and high residual water layer on the promenade), or non-uniform (collision prior to dike foot), with the corresponding dominant peaks as described for *wave catch-up*. Lastly, *sequential overtopping*, similarly to *wave catch-up*, resulted in more efficient overtopping due to high residual water layer from previous overtopping waves. This mechanism produced the highest impact force in the small scale test, but was not found to develop in the same way in the corresponding large scale impact. This suggests that a discrepancy for this impact mechanism is present, meaning the sequential overtopping mechanism can wrongly be considered as representative if only small scale data is available. Although the difference in scale is again thought to partly contribute to this discrepancy, once more model effects should not be ignored and their contribution further analysed. Comparison of two sets of impacts with similar post-overtopping characteristics and force-time signals did not show a definitive tendency for scaling bias when considering the influence of natural variability and the accuracy of the measurement techniques used.

Lastly, the *dynamic* and *quasi-static impact force* ratios for the largest 10% of impacts at each scale were analysed, and the bore impact classification suggested by Streicher et al. (2016) applied. The bore impact types were found to be very similarly distributed between the two classes, and a sensitivity analysis showed that changes in the impact peak ratio threshold of 1.2, proposed by Streicher et al. (2016), do not affect this distribution significantly. The ratio of *dynamic bore impacts* (dominant first peak) to *quasi-static/down-rush bore impacts* (dominant second peak) was however different when just the highest 10 impacts were considered. The small scale model seems biased towards the latter *quasi-static/down-rush bore* type for these extreme impact events, which then points towards a possible difference in the impact mechanisms between the two scales. Furthermore, since the force-time signal is linked to the pre-impact flow evolution, it is possible to conclude that some variation in these is also present between the two models. This line of thinking is also supported by the discrepancy in entrapped air pocket impacts previously mentioned. It is also concluded that the Streicher et al. (2016) bore impact classification approach has potential as a useful tool for gaining quick insight into quantifying impact and model comparability. However, the subset of impact events chosen for this can vary the outcome considerably and should be carefully considered.

The second aim was to explore the applicability of innovative measuring devices in a hydraulic flume setting. These devices were the Terrestrial Laser Scanner (TLS), waterproof action cameras and the use of the wall-mounted window and optical pahase detection probe (OPDP) for void fraction measurements.

The laser scanner has previously been used in hydraulic modelling experiments at Deltares, however, the specifics of how it was applied during the WALOWA tests are of interest. The large model size and compound profile being scanned did not prevent the acquisition of reliable measurements over the length of the promenade and the steel wall. The sequence between overtopping and initial run-up at the wall was accurately captured. However, once continued run-up has been observed, the deflection of the flow and large amount of water spray negates an accurate measurement. In addition, the full foreshore propagation of the waves could not be reliably captured by the device, which is a function of the scan distance and the reflectivity of the scanned surface (water in this case). This suggests that the device is not suitable for e.g. reflection analysis using the present setup. The application of a median filter in space and time improved the scanned surface accuracy to satisfactory levels.

The action cameras proved beneficial in obtaining visual reference of the flow. Furthermore, the resolution, framerate and general high picture quality for the particular camera model used were sufficient for obtaining the bore front velocity averaged over the promenade. The video footage also proved useful when analysis of the laser scanner data was being conducted. Powering of the cameras proved difficult due to the requirement to ensure the devices remained watertight and the banning of the use of 220 Volt power sockets within the model area during a test. The large recorded file sizes should be taken into consideration, as these can potentially slow the workflow for a demanding project such as the WALOWA experiments. The fixed wide-angle lens means that these devices are most useful for short to medium distances (order 5 m; dependent on the test case, settings used and required accuracy), and the changing Field of View (FoV) options between different resolution settings could introduce added difficulty in the test planning phase. The use of the in-camera barrel distortion correction profile is recommended as this can negate the laborious efforts of postprocessing correction of the footage.

The flush-mounted window installed in an opening in the steel wall allowed for the use of a high-speed camera to record the bubble plume evolution during a wave impact. While this measuring technique has potential, this was not utilised in the present work. The high data output limits the applicability of this method to tests of shorter duration. For the present model setup, controlled lighting of the flow was difficult to achieve, resulting in varying exposure throughout the duration of a wave impact even. This can also make analysis of the recordings difficult to automate. It was also apparent that the framerate and shutter speed were sometimes insufficient for capturing a clear image of the flow during the run-up phase, although image clarity improved once the flow had decelerated. The optical phase detection probe (OPDP) proved robust enough for measurement applications in a large scale model even under direct wave impacts. This device has the benefit of outputting smaller file size when compared to the high-speed camera. It is therefore recommended for longer experiments.

5.2. Recommendations

With regard to the first aim of this thesis, the following recommendations are made:

- Increasing the certainty in evaluating scale effects means to limit all other variables, such as model effects and inherent variability, to a minimum. Although very similar, the two models compared in this work were not ideal replicas of each other. It is therefore recommended that a small scale model is built that replicates the large scale test setup completely;
- It is recommended that the number of tests analysed is increased and the confidence interval of extreme forces determined to quantify the inherent variability of wave impacts and increase the reliability of the obtained results;
- Use of a larger relative scale difference between the two models will lead to an increase in the effect of scaling bias. It is therefore recommended that 1:1 scale (prototype) tests replicating the model setup investigated here are conducted. The addition of (at least) a third scaled model will also enable the assessment of the non-linearity of the scaling effects;
- Inclusion of pressure sensors at both scales. Chen et al. (2014) remarked on their suitability for better capturing the dynamic force peak component of an impact. It is in this peak where the effects of the scaling bias due to the air void fraction are expected to be most prevalent, and a more accurate analysis of impact 'cushioning' and pressure rise times will be made possible. The use of pressure sensors will also enable a similar analysis as the one done by Lafeber et al. (2012b) for identifying Elementary Loading Processes (ELPs) in the signal output of the individual units;
- Air void ratio measurements at both scales are recommended for quantifying the bubble size distribution and plume evolution in time. An optical phase detection probe (OPDP) is recommended due to its relatively easy implementation and minimum obstruction to the flow. For shorter tests, this can also be supplemented by a high-speed camera in a setup similar to the present tests.

Recommendations relating to the second thesis aim are presented below.

Water proof action cameras

Note that these are relevant for the camera model used in the WALOWA tests:

- Quick and easy offloading of data is essential, especially on a tight schedule. It is recommended that this be a key consideration when designing a test programme. It is recommended, if possible, to avoid using the camera's USB 2.0 connection, and instead offload data directly from the memory card. This requires both a robust mounting solution and easy access to the device itself;
- Due to the very wide fisheye lens it is recommended that these cameras are suitable for use at small distances. Depending on the model of camera, settings used, and test setup, this could be as little as 30 to 40 cm (minimum focus distance);
- Direct access to every camera is strongly recommended to allow for troubleshooting, offloading of data, and direct operation of the device. Using the remote control to operate the cameras proved sporadic at best, further necessitating direct access. Furthermore, the remote range is severely reduced once operating inside the flume, so it is advisable to test the position of the cameras based on the ability to reliably control them;
- The following settings are recommended: Protune mode to enable manual selection of ISO; digital video stabilisation – off;
- For run-up measurements, it is recommended that the wall-mounted window is extended upwards and a camera positioned behind it (estimated minimum distance approximately 1.60 m behind the wall for the WALOWA setup).

High-speed camera and optical phase detection probe (OPDP)

- It is recommended to mount the camera as securely as possible to avoid the need for finetuning focus;
- The use of a telephoto lens is recommended to allow for a narrower depth of field;
- Framerates higher than 100 fps seem necessary for capturing the water flow during the initial run-up phase. It is recommended that this is taken into consideration when considering similar application of the device;
- It is strongly recommended that lighting of the impacting flow is done from below for obtaining more evenly-illuminated recordings (see also Appendix 14);
- The pins (optical fibres) of the OPDP need to penetrate the air bubbles for accurate aeration measurements. It is recommended that a OPDP with angled and partially encased fibres is used to ensure this.

Laser scanner

- It is recommended that the Standard Resolution (SR) model of the SICK laser scanner is used, as it provides a reasonable trade-off between accuracy and increased scan distance;
- The possibility to implement the 5 echoes setting to eliminate droplet reflections should be explored for run-up measurements;
- A recommendation on mounting accuracy is to ensure the device installed without deviations from the intended position. This allows for quicker and accurate coordinate conversion during data processing;
- Aligning the scanned profile with an axis of particular interest, for example a profile leading to the pressure sensors array or load cell plate, can be beneficial for analysis purposes due to the inevitable transverse variations in the flow.

References

Allis, M., Peirson, W. & Banner, M., 2011. *Application of LiDAR As a Measurement Tool For Waves.* Maui, Hawaii USA, Proceedings of 21st International Offshore and Polar Engineering Conference, pp. 373-379.

Bagnold, R., 1939. Interim report on wave-pressure research. *Excerpt Journal of The Institution of Civil Engineers,* Volume 12, pp. 201-226.

Battjes, J., 1974. Surf similarity. *Coastal Engineering Proceedings.*

Blenkinsopp, C. & Chaplin, J., 2011. Void fraction measurements and scale effects in breaking waves in freshwater and seawater. *Coastal Engineering,* Issue 58, pp. 417-428.

Blenkinsopp, C. et al., 2012. Application of LiDAR technology for measurement of time-varying free-surface profiles in laboratory wave flume. *Coastal Engineering,* Volume 68, pp. 1-5.

Bogaert, H., Léonard, S., Brosset, L. & Kaminski, M., 2010. *Sloshing and scaling: results from Sloshel project.* Rhodes, Greece.

Bosboom, J. & Stive, M. J., 2015. *Coastal Dynamics I.* Version 0.5 ed. Delft: Delft Academic Press (VSSD-uitgeverij).

Brosset, L. et al., 2011. *A Mark III panel subjected to a flip-through wave impact: results from the Sloshel project.* Hawaii, USA, Proceedings of 21st International Offshore and Polar Engineering Conference.

Bullock, G. et al., 2001. The influence of air and scale on wave impact pressures. *Coastal Engineering,* Volume 42, pp. 291-312.

Bullock, G., Obhrai, C., Peregrine, D. & Bredmose, H., 2007. Violent breaking wave impacts. Part 1: Results from large-scale regular wave tests on vertical and sloping walls. *Coastal Engineering,* 54(8), pp. 602-617.

Cantersa, F. et al., 2014. Land-use simulation as a supporting tool for flood risk assessment and coastal safety planning: The case of the Belgian coast. *Ocean & Coastal Management,* 101(Part B), pp. 102-113.

Chen, X., 2016. *Impacts of overtopping waves on buildings on coastal dikes.* Delft.

Chen, X. et al., 2012. Hydrodynamic laod on the building caused by overtopping waves. *Coastal Engineering.*

Chen, X., Hofland, B., Altomare, C. & Uijttewaal, W., 2014. Overtopping flow impact on a vertical wall on a dike crest. *Coastal Engineering.*

Cox, J. C. & Machemehl, J., 1986. Overload Bore Propagation Due to an Overtopping Wave. *Journal of Waterway, Port, Coastal, and Ocean Engineering,* 112(1), pp. 161-163.

De Rouck, J. et al., 2012. Full scale impact tests of an overtopping bore on a vertical wall in the large wave flume (GWK) in Hannover. *Coastal Engineering Proceedings,* p. 62.

Derondea, B. et al., 2006. Use of Airborne Hyperspectral Data and Laserscan Data to Study Beach Morphodynamics along the Belgian Coast. *Journal of Coastal Research,* 22(5), pp. 1108-1117.

Diamantidou, E., 2014. *Application of laser scanner for measurement of wave elevation in a wave flume.* Delft: Deltares internal report.

Diamantidou, E., 2014. *Application of laser scanner for measurement of wave run-up, overtopping volume and wave overtopping discharge in a large-scale wave flume.* Delft: Deltares internal report.

Eikelboom, H., 2016. *Verification and validation of a spray water model for maritime structures.* Master Thesis. Delft: Delft University of Technology.

EurOtop, 2016. *Manual on wave overtopping of sea defences and related structures. An overtopping manual largely based on European research, but for worldwide application.* Van der Meer, J.W., Allsop, N.W.H., Bruce, T., De Rouck, J., Kortenhaus, A., Pullen, T., Schüttrumpf, H., Troch, P. and Zanuttigh, B*. www.overtopping-manual.com.* 2nd ed.

Frostick, L., McLelland, S. & Mercer, T., 2011. *User Guide to Physical Modelling and Experimentation: Experience of the HYDRALAB Network.* Leiden, The Netherlands: CRC Press/Balkema.

Fujifilm Corporation, 2016. *Fujinon Machine Vision Lenses. www.fujifilm.eu.* Fujifilm Corporation.

Goda, Y., 2010. *Random Seas and Design of Maritime Structures.*

GoPro, 2016. *Hero 5 Black User Manual.* GoPro Inc. *https://gopro.com/help/productmanuals*.

Haerensa, P., Bollea, A., Trouwb, K. & Houthuys, R., 2012. Definition of storm thresholds for significant morphological change of the sandy beaches along the Belgian coastline. *Geomorphology,* Volume 143-144, pp. 104-117.

Heller, V., 2011. Scale effects in physical hydraulic engineering models. *Journal of Hydraulic Research,* 49(3), pp. 293-306.

Hofland, B., Diamantidou, E., Steeg, P. v. & Meys, P., 2015. Wave runup and wave overtopping measurements using a laser scanner. *Coastal Engineering,* Issue 106, pp. 20-29.

Hofland, B., Wenneker, I. & Gent, M. V., 2013. *Description of the New Delta Flume.* Edinburgh, Proceedings from Coastlines, Marine structures & Breakwaters Conference.

IO Industries, 2011. *Flare High-Speed CMOS Area Scan Camera Series 2M280 / 4M140 CoaXPress. User's Manual. Revision 3.2.* IO Industries Inc.

IO Industries, 2016. *DVR Express Core. User's Manual. Revision 2.2.* IO Industries Inc.

Jonkman, S. N., 2005. Global Perspectives on Loss of Human Life Caused by Floods. *Natural Hazards,* 34(2), pp. 151-175.

Jonkman, S. & Schweckendiek, T., 2015. *Flood Dedences. Lecture notes CIE5314.* Draft version April 2015 ed. Delft: Delft University of Technology.

Kortenhaus, A. & Oumeraci, H., 1998. Classification of wave loading on monolithic coastal. *Coastal Engineering Proceedings.*

Lafeber, W., Brosset, L. & Bogaert, H., 2012a. *Comparison of wave impact tests at large and full scale: results from the Sloshel project.* Rhodes, Greece.

Lafeber, W., Brosset, L. & Bogaert, H., 2012b. *Elementary Loading Processes (ELP) involved in breaking wave impacts: findings from the Sloshel project.* Rhodes, Greece.

Lebbe, L., Meir, N. V. & Viaene, P., 2008. Potential Implications of Sea-Level Rise for Belgium. *Journal of Coastal Research,* 24(2), pp. 358-366.

Nicholls, R., 2004. Coastal flooding and wetland loss in the 21st century: changes under the SRES climate and socio-economic scenarios. *Global Environmental Change,* 14(1), pp. 69-86.

Oumeraci, H., Klammer, P. & Partenscky, H. W., 1993. Classification of Breaking Wave Loads on Vertical Structures. *Journal of Waterway, Port, Coastal, and Ocean Engineering,* 119(4), pp. 381-397.

Ramachandran, K. et al., 2012. Loading of vertical walls by overtopping bores using pressure and force sensors - a large scale model study. *Coastal Engineering Proceedings,* Volume 33, p. 15.

Ryu, Y. & Chang, K., 2008. Green water void fraction due to breaking wave impinging and overtopping. *Exp Fluids,* 45(5), pp. 883-898.

Schüttrumpf, H. & Oumeraci, H., 2005. Layer thicknesses and velocities of wave overtopping flow at seadikes. *Coastal Engineering,* 52(6), pp. 473-495.

Scott, J. C., 1975. The role of salt in whitecap persistence. *Deep-Sea Research,* Volume 22, pp. 653-657.

SICK, 2011. *Operating Instructions. Laser Measurement Sensors of the LMS5xx Product Family. www.sick.com*. SICK AG.

Streicher, M., 2013. *Applying Laser Ranging for the Monitoring of Water Waves in the new Deltares Delta Flume Facility.* Master Thesis. Braunschweig: Technische Universität Braunschweig.

Streicher, M., 2017. *Data storage report.* Draft version April 2017 ed. Ghent: Ghent University.

Streicher, M., Hofland, B. & Lindenbergh, R. C., 2013. Laser Ranging for Monitoring Water Waves in the new Deltares Delta Flume. *The International Archives of the Photogrammetry, Remote Sensing and Spatial Information Sciences,* 34.

Streicher, M., Kortenhaus, A. & Hohls, C., 2016. *Analysis of post overtopping flow impacts on a vertical wall at the Belgium coast.* Ottawa, University of Ottawa.

Valentini, N., Hofland, B. & Saponieri, A., 2014. *Application of LiDAR as a measurement instrument for laboratory water waves.* Varna, Bulgaria, Proceedings of Coastlab 2014.

Van der Meer, J. W. et al., 2010. *Flow depths and velocities at crest and landward slope of a dike, in theory and with the wave overtopping simulator.* Shanghai, China, Coastal Engineering Research Council.

Van Doorslaer, K., Romanoc, A., Roucka, J. D. & Kortenhaus, A., 2017. Impacts on a storm wall caused by non-breaking waves overtopping a smooth dike slope. *Coastal Engineering,* Volume 120, pp. 93-111.

Van Gent, M. R. A., 2001. Wave runup on dikes with shallow foreshores. *Journal of Waterway, Port Coastal and Ocean Engineering,* 127(5), pp. 254-262.

List of Figures

List of Tables

List of Appendices

Appendix 1	Detailed drawing of the WALOWA model setup
Appendix 2	Full list of conducted WALOWA tests and operational devices
Appendix 3	Full list of measuring instruments implemented in the WALOWA tests
Appendix 4	Detailed drawings of the mounting position of the terrestrial laser scanner (TLS)
Appendix 5	Specification sheet – Laser Scanner
Appendix 6	Specification sheet – High-speed camera body
Appendix 7	Specification sheet – High-speed camera lens
Appendix 8	Specification sheet – Pressure sensors
Appendix 9	Specification sheet – Load cells
Appendix 10	Discrepancy in water elevation measurements
Appendix 11	Timesteps of L3 and L4 large scale impacts
Appendix 12	Timesteps of S3 and S4 small scale impacts
Appendix 13	Sensitivity analysis of impact force peaks ratio threshold
Appendix 14	Illumination of the flow for the high-speed camera recording

Appendix 1

Detailed drawing of the WALOWA model setup

A to-scale drawing of the WALOWA model setup is hereby presented.

Drawing	Drawing number	Scale	
WALOWA model setup	01	1:350	1:25

See next page

Scale: 1:350

Physical model: Top view

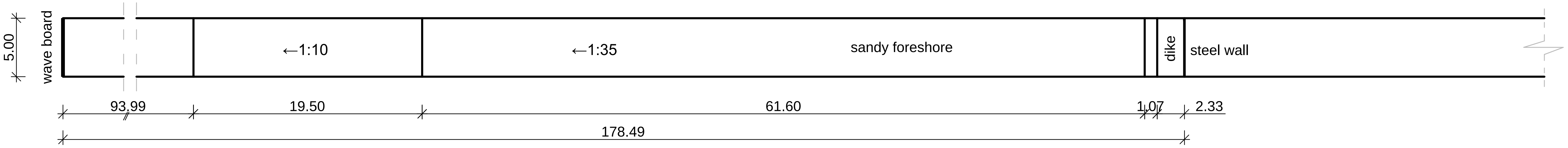

Physical model: Longitudinal section

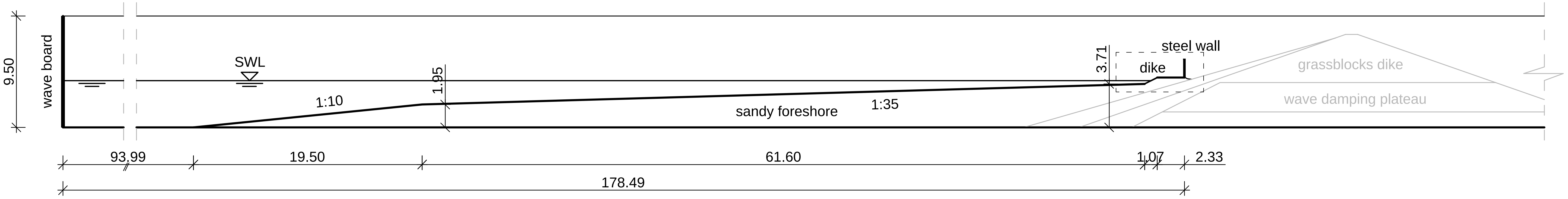

Scale: 1:25

Detail:
Dike, steel wall and promenade: Longitudinal section

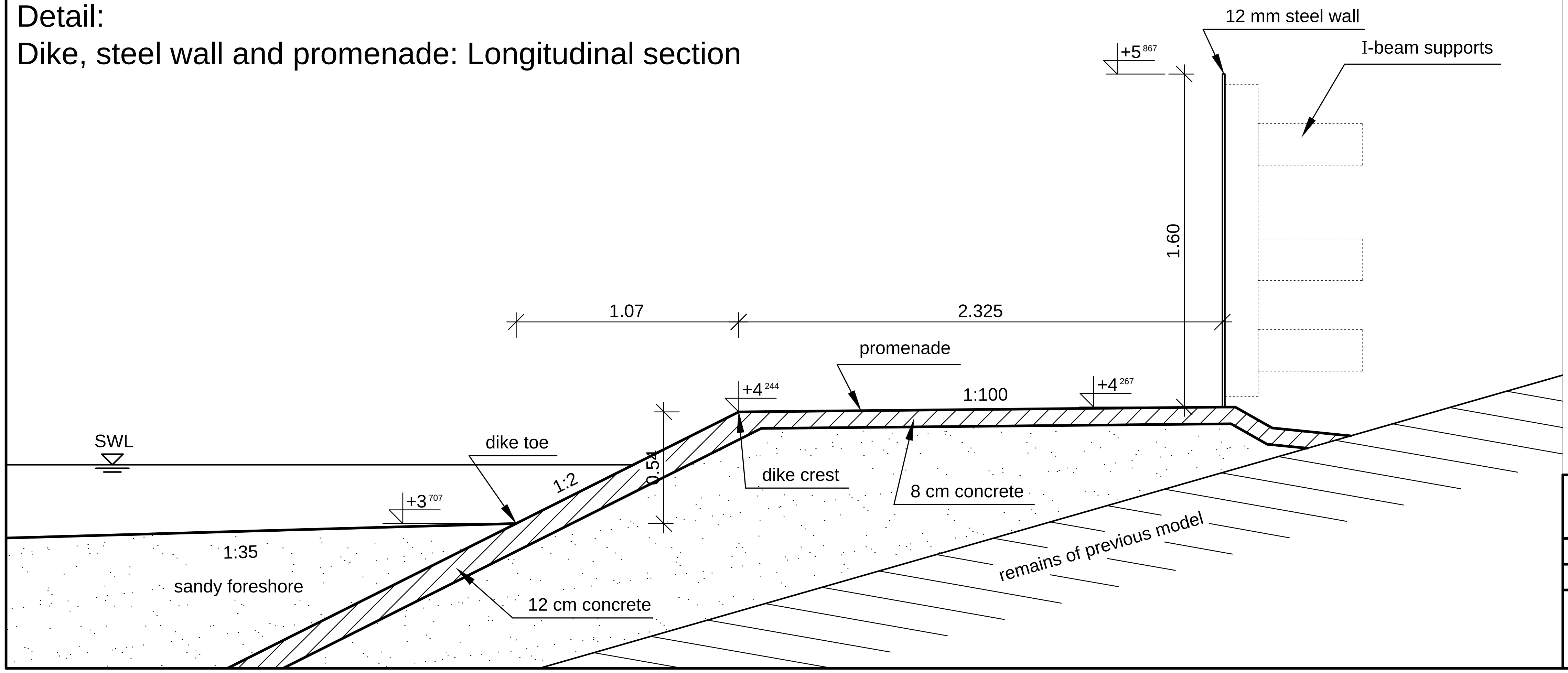

Notes:

1. All dimensions are given in meters.
2. Elevation measurements reference level is assumed to be the flume botton = ±0.00 m.
3. The supporting frame behind the steel wall front is schematically represented.
4. The still water level (SWL) given here corresponds to 3.99 m as measured at the wave board. This corresponds to the measured water level during test WLW_Irr_1_F.
5. Measurement devices and additional mounting frames have been omitted.

Wave Impacts on Storm Walls
A study on scale effects

Delft University of Technology

Krasimir Krasimirov Marinov	Student number: 4535715
Drawing:	Scale: 1:350 1:25
WALOWA model setup	Paper size: A3
	Drawing nr.: 01

Appendix 2

Full list of conducted WALOWA tests and corresponding operational devices

The WALOWA test programme is presented in Table 21. There, the operational status of several measurement (laser scanner, cameras, optical phase detection probe) and supplementary (lighting) instruments is also given. The legend and additional notes for Table 21 are given below.

Legend:

LS	Laser scanner
VFM	Void fraction meter (optical phase detection probe)
HS	High-speed camera
GP	GoPro action camera
OV	Overview
SV	Side view
W	Window
L	Lighting
W1	Light behind window
W2	Light above window
O	Operational
X	Not operational
O	Operational (issue or important change of settings)

Notes:

*	Aperture teporarily adjusted to f/2.8 due to issues with the camera focus
**	Aperture set back to f/1.4 after camera adjustment (finetuning of position, focus and cleaning of the protective case window)
***	Individual files missing/corrupted or incomplete recording
****	Makeshift light diffuser implemented
*****	Channel 2 of device appeared to not be operational

Table 21: WALOWA test programme and corresponding operational devices.

Test day	Date	Test name	LS	VFM	HS	GP			L			
						OV	SV	W	OV	SV	W1	W2
Day 1	20-Mar	Bi_01_4	O	X	O	X	O	X	O	O	X	O
		Bi_01_5	O	X	O	X	X	X	O	O	O	X
Day 2	21-Mar	Bi_01_6	O	X	O	O	O	O	O	O	O	X
		Bi_02_4	O	X	O	O	O	O	O	O	O	X
Day 3	22-Mar	WLW_Irr_1_F	O	X	O	O	O	X	O	O	O****	X
Day 4	23-Mar	WLW_Irr_2_F	O	X	O	O	O***	O	O	O	O	X
Day 5	24-Mar	NO TESTS	-									
Day 6	27-Mar	WLW_Irr_2_S	O	X	O	O	O	O	O	O	O	X
Day 7	28-Mar	WLW_Irr_3_F	O	O	O	O	O	O	O	O	O	X
Day 8	29-Mar	Bi_02_5	O	O	O*	O	O	O	O	O	O	X
		Bi_02_6	O	O	O	O	O	O	O	O	O	X
		Bi_02_6_r	O	O	O	O	O	O	O	O	O	X
		WLW_Irr_8_F	O	O	O**	O	O	X	O	O	O	X
Day 9	30-Mar	WLW_Irr_4_F	O	O	X	O	O	O	O	O	O	X
		WLW_Irr_5_F	O	O	O	O	O	O	O	O	O	X
Day 10	31-Mar	WLW_Irr_1_F_r	O	O*****	O	O***	O	O	O	X	X	X
		WLW_Irr_7_F	O	O*****	O	O	O	O	O	O	O	X
Day 11	03-Apr	WLW_Irr_2_F_r	O	O*****	O	O	O	O	O	O	O	X
		Bi_01_6_r	O	O*****	O	O	O	O	O	O	O	X
Day 12	04-Apr	Bi_03_6	O	O	O	O	O	O	O	O	O	X
		Bi_03_6_1	O	O	O	X	O***	O	O	O	O	X
		Bi_03_6_2	O	O	O	O	O***	O	O	O	O	X
		WLW_Irr_6_F	O	O	O	O	O	O	O	O	O	X

Appendix 3

Full list of measuring instruments implemented in the WALOWA tests

The WALOWA project was a collaborative effort that included many researchers operating a variety of measurement instruments throughout the test campaign. Here, a list of devices that were implemented during the tests is presented (Table 22). This list is partly based on the draft version of an internal document termed ‘Data storage report’ produced by Maximilian Streicher, version 5 April 2017 (Streicher, 2017).

Table 22: Measurement instruments used in the WALOWA tests and their location in GCS coordinates.

Instrument	**Description**	**Name**	**Position (GCS)**		
			X [m]	Y [m]	Z [m]
WHM	**Wave gauge**	WHM02	43.50	-	-
		WHM03	49.50	-	-
		WHM04	61.50	-	-
		WHM07	108.50	-	-
		WHM11	126.50	-	-
		WHM13	155.70	-	-
		WHM14	174.75	-	-
USD	**Ultrasonic distance sensor**	USD1	177.97	4.00	5.25
		USD2	176.93	4.00	5.25
		USD3	177.45	4.00	5.25
		USD4	176.48	4.00	5.25
EMS	**Electro-magnetic current meter**	EMS	176.93	4.34	4.28
WLDM	**Wave gauge on promenade**	WLDM1	176.48	3.76	-
		WLDM2	176.93	3.76	-
		WLDM3	177.41	3.76	-
		WLDM4	177.96	3.76	-
PaddleWheel	**Paddle wheel**	PaddleWheel1	176.45	4.45	4.28
		PaddleWheel2	176.96	4.45	4.28
		PaddleWheel3	177.46	4.45	4.28
		PaddleWheel4	177.97	4.45	4.28
KRM	**Load cell**	KRM01	178.50	3.21	5.42
		KRM02	178.50	3.21	4.45
DR	**Pressure sensor**	DR01	178.50	2.16	4.29
		DR02	178.50	2.16	4.36
		DR03	178.50	2.16	4.43
		DR04	178.50	2.16	4.50
		DR05	178.50	2.16	4.57
		DR06	178.50	2.16	4.64
		DR07	178.50	2.16	4.71
		DR08	178.50	2.16	4.78
		DR09	178.50	2.16	4.85
		DR10	178.50	2.16	4.97
		DR11	178.50	2.16	5.09
		DR12	178.50	2.16	5.21
		DR13	178.50	2.16	5.33
		DR14	178.50	2.10	4.57

		DR15	178.50	2.24	4.57
ASM	**Argus surface meter**	ASM	174.25	1.00	-
GP	**GoPro action camera**	GP_OV	172.00	2.50	8.00
		GP_SV	177.26	0.07	5.44
		GP_W	179.09	1.12	4.76
HS	**High-speed camera**	HS	179.34	1.12	4.63
VFM	**Optical phase detection meter**	VFM	178.50	1.57	4..58
LS	**Laser scanner**	LS	175.64	4.78	8.99
WaveRadar	**Wave radar**	WaveRadar	171.35	3.40	7.85
Profiler	**Mechanical profiler**	Profiler	movable		

Appendix 4

Detailed drawings of the mounting position of the terrestrial laser scanner (TLS)

To-scale drawings of the mounting position of the laser scanner, wooden mounting frame, and measured estimated trace of the scanned profile are hereby presented.

Drawing	**Drawing number**	**Scale**		
Laser scanner position and mounting frame	02	1:100	1:30	1:10
Laser scanner position. Trace of scanned profile	03	1:50		

See next pages

Scale: 1:100

Laser scanner position: Top view

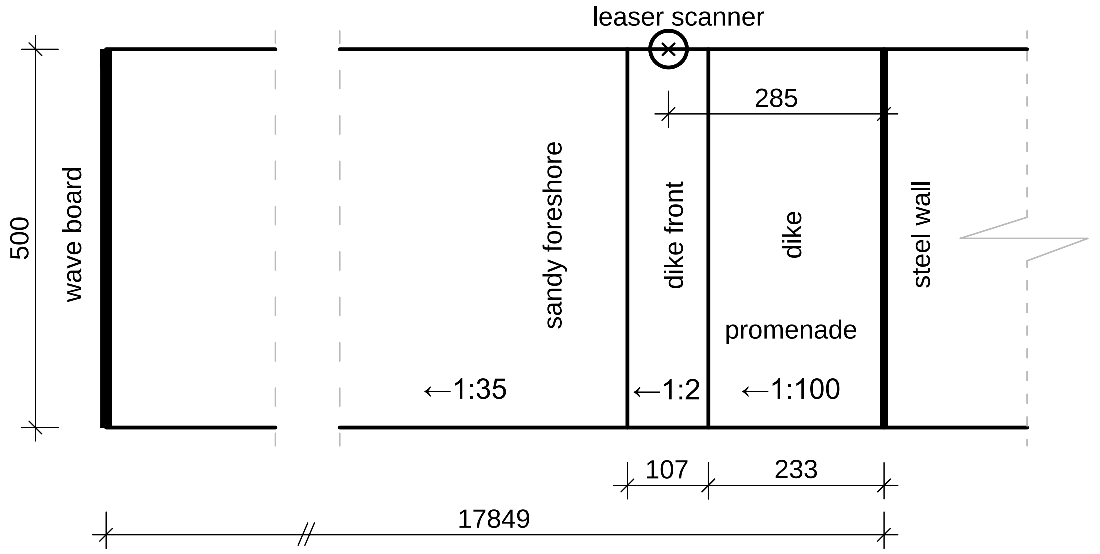

Laser scanner position: Longitudinal section

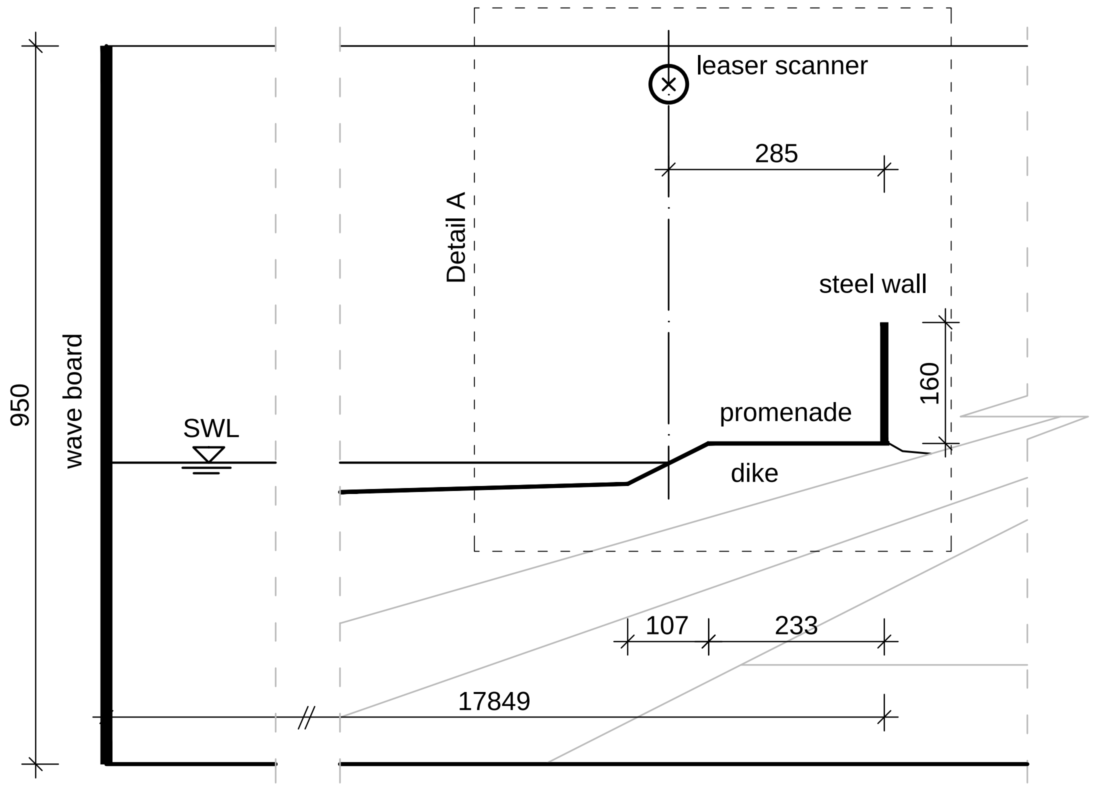

Detail B: Mounting frame

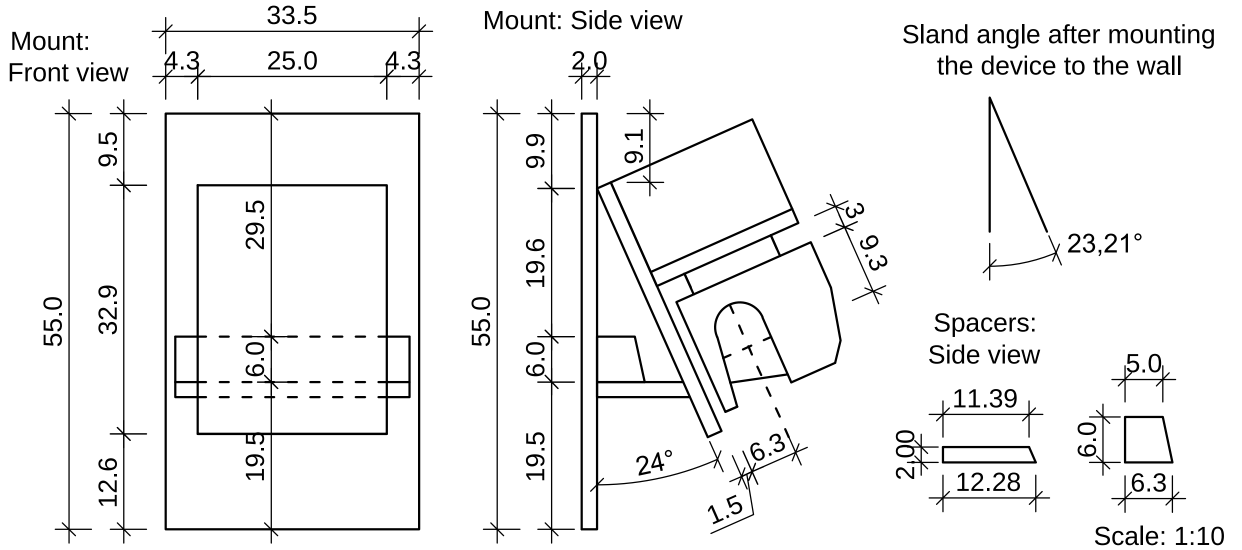

Scale: 1:10

Detail A: Laser scanner precise location

Scale: 1:30

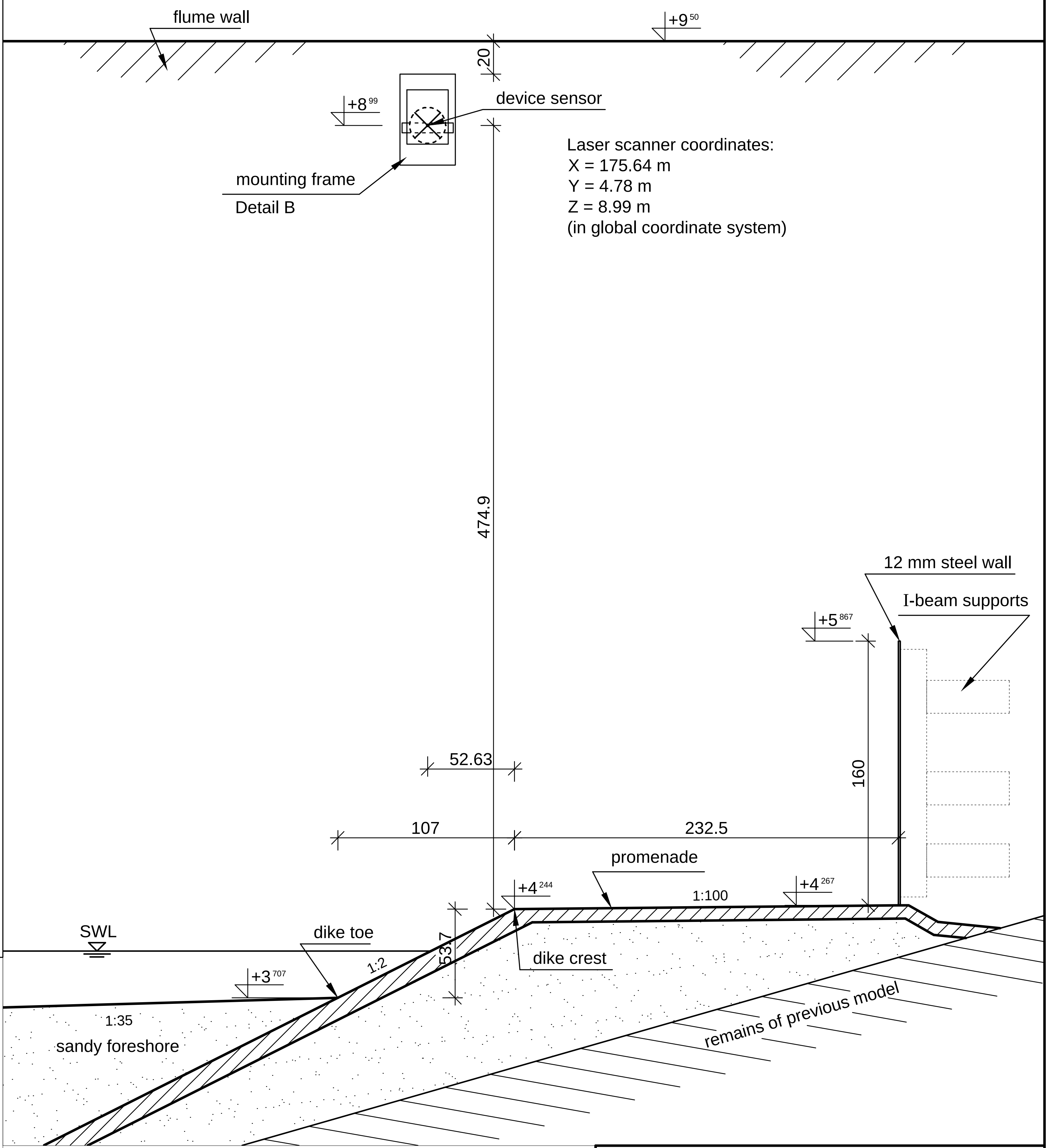

Laser scanner coordinates:
X = 175.64 m
Y = 4.78 m
Z = 8.99 m
(in global coordinate system)

Notes:
1. All dimensions are given in centimeters.
2. Elevation measurements reference level is assumed to be the flume botton = ±0.00 m.
3. Mount angle of 24°. Device slant angle reduced to 23.21° after fixing the device and mount to the flume wall.
4. Supporting frame behind steel wall front schematically represented.
5. Mount material: wood; plywood boards.

Wave Impacts on Storm Walls
A study on scale effects
Delft University of Technology
Krasimir Krasimirov Marinov
Student number: 4535715
Drawing:
Laser scanner position and mounting frame
Scale: 1:100 1:30 1:10
Paper size: A3
Drawing nr.: 02

Position of laser scanner and scanned profile: Top view

Scale: 1:50

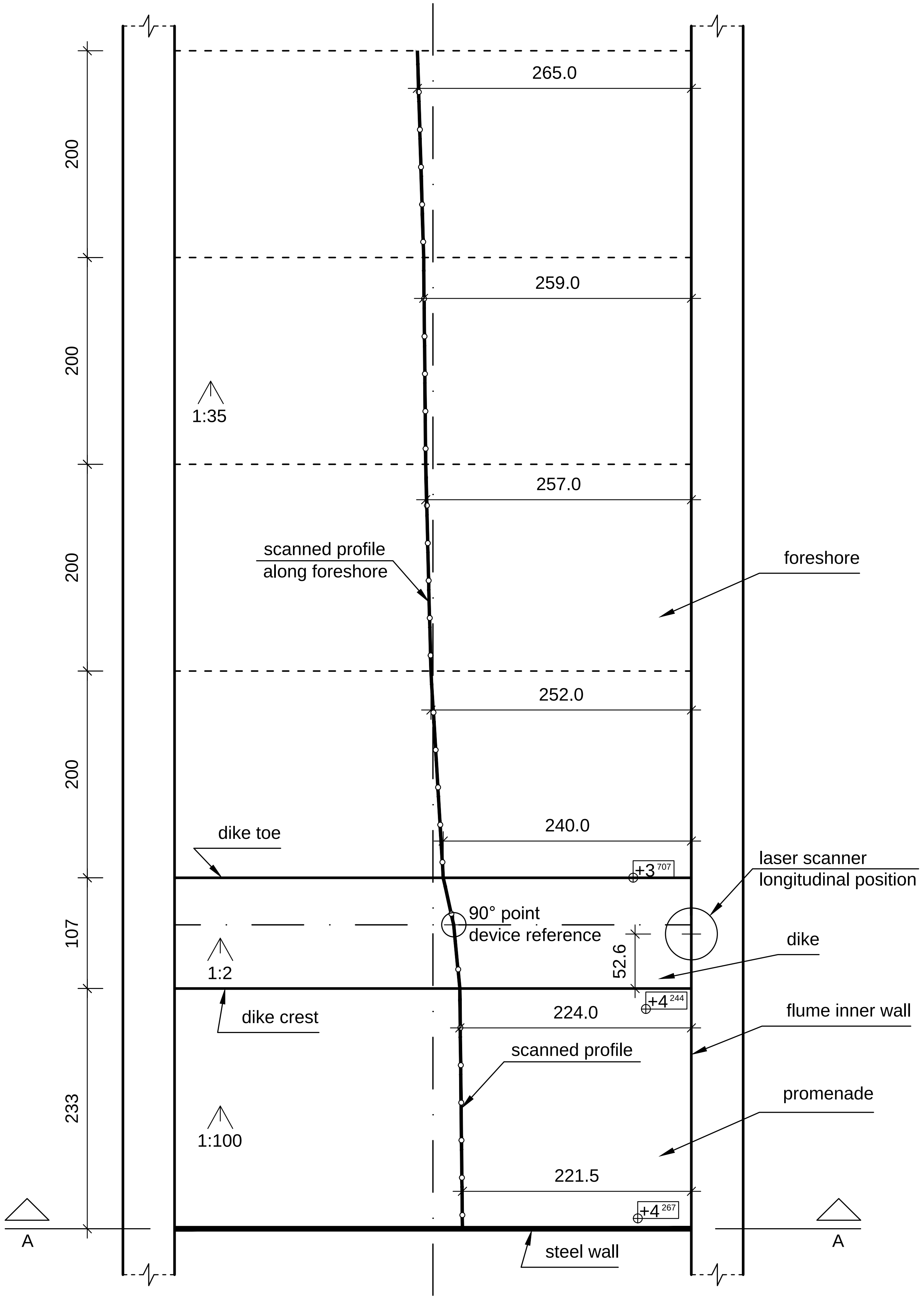

Position of laser scanner: Cross-section A-A

Scale: 1:50

Observer viewpoint towards the wave board

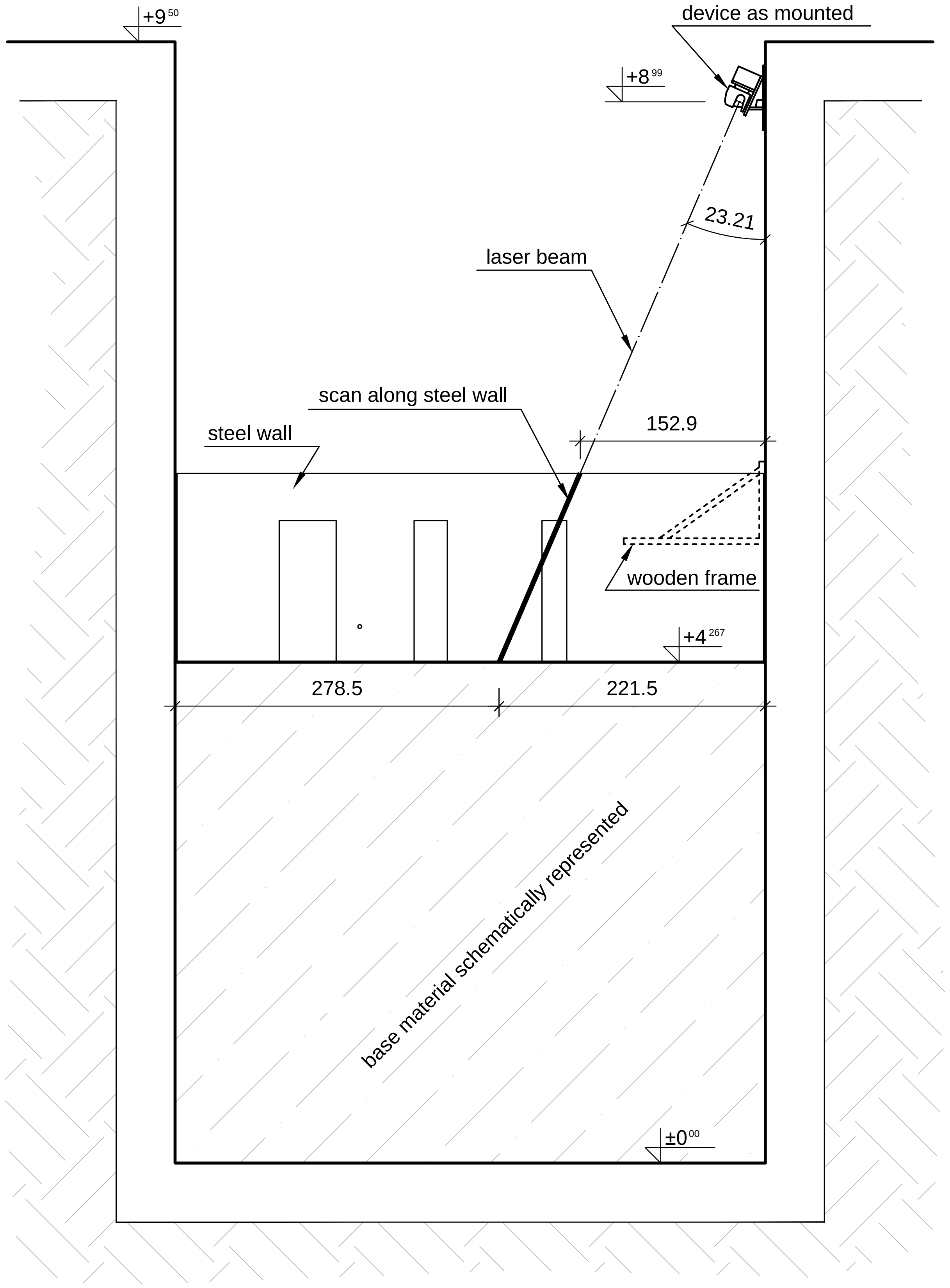

Notes:

1. All dimensions are given in centimeters.
2. Elevation measurements reference level is assumed to be the flume botton = ±0.00 m.
3. Flume cross-section schematically represented; internal dimensions of flume are to scale.
4. Scanned profile along foreshore only in dry conditions (no water in the flume).
5. Some measurement devices have been omitted.

Wave Impacts on Storm Walls A study on scale effects	
Delft University of Technology	
Krasimir Krasimirov Marinov	Student number: 4535715
Drawing:	Scale: 1:50
Laser scanner position. Trace of scanned profile	Paper size: A3 Drawing nr.: 03

Appendix 5

Specification sheet – Laser Scanner

The terrestrial laser scanner (TLS) specification sheet presented here is extracted from the manufacturer's user manual (SICK, 2011, pp. 101-105). For access to the most up-to-date version of this document, please visit the manufacturer's website: https://www.sick.com

See next page

10 Technical specifications

10.1 Data sheet LMS5xx laser measurement sensor

	Minimum	**Typical**	**Maximum**
Functional data			
Scan angle			190 °
Scanning frequency			
Lite	25 Hz		75 Hz
PRO/Heavy Duty	25 Hz		100 Hz
Remission	2 %		Several 1,000 % [1] (reflectors)
Angular resolution			
Lite	0.25 °		1 °
PRO/Heavy Duty	0.1667 °		1 °
Measurement accuracy [2]			
Standard Resolution		±24 mm	
High Resolution		±12 mm	
Measurement error 1st reflected pulse [3]			
Systematic error (at 10 % object remission[4])			
Standard Resolution 1 to 10 m		±25 mm	
Standard Resolution 10 to 20 m		±35 mm	
Standard Resolution 20 to 30 m		±50 mm	
High Resolution 1 to 10 m		±25 mm	
High Resolution 10 to 20 m		±35 mm	
Statistical error (1σ) (at 10 % object remission[4])			
Standard Resolution 1 to 10 m		±6 mm	
Standard Resolution 10 to 20 m		±8 mm	
Standard Resolution 20 to 30 m		±14 mm	
High Resolution 1 to 10 m		±7 mm	
High Resolution 10 to 20 m		±9 mm	
Immunity to external light		70 klx	
Distance from mirror axis of rotation (zero point on the x and y axis) to the rear of the device	93 mm		
Distance between centre of the scan plane and the bottom edge of the housing	63 mm		
Distance measuring range	0.7 m		80 m
Distance measuring range at 10 % object remission			
LMS500-2x000 Lite/PRO, LMS511-2x100 Lite/PRO/Heavy Duty, LMS581-20100 PRO	0.7 m		26 m
LMS511-1x100 Lite/PRO/Heavy Duty, LMS531-11100 Lite/PRO, LMS581-10100 PRO	1 m		40 m
Power-up delay		30 s	60 s

Tab. 43: Data sheet LMS5xx

	Minimum	**Typical**	**Maximum**
General data			
Laser class	Laser class 1 according to IEC 60825-1 (2007-3) (complies with 21 CFR 1040.10 and 1040.11 except for deviations pursuant to Laser Notice No. 50, June 2007)		
Enclosure rating	As per EN 60529 (1991-10); A1 (2002-02)		
LMS500	IP 65		
LMS511/LMS531/LMS581	IP 67		
EMC test	As per EN 61000-6-2 (2005-08), EN 61000-6-3 (2007-01)		
Electrical safety	As per EN 60950-1 (2006-04) and EN 60950-1/A-11 (2009-03)		
Ambient operating temperature range			
LMS500	0 °C		+50 °C
LMS511/LMS531/LMS581	–30 °C		+50 °C
LMS511 Heavy Duty	–40 °C		+60 °C
Storage temperature range	–40 °C		+70 °C max. 24 h
Humidity (taking into account the ambient operating temperature range)	DIN EN 60068-2-61, method 1		
Vibration resistance	As per EN 60068-2-6 (2008-10)		
Frequency range	10 Hz		150 Hz
Amplitude	5 g RMS		
Shock resistance	As per EN 60068-2-27 (2009-05), EN 60068-2-29 (1995-03)		
Single shock	15 g, 11 ms		
Continuous shock	10 g, 16 ms		
Sender	Pulsed laser diode		
Wave length	895 nm	905 nm	915 nm
Divergence of the collimated beam (solid angle)			
High Resolution		4.7 mrad	
Standard Resolution		11.9 mrad	
Light spot size at the front screen		13.6 mm	
Light spot size at 18 m scanning range			
High Resolution		99 mm	
Standard Resolution		228 mm	
Housing			
Material	GD-ALSI12 3.2582.05		
Color LMS500	RAL 5012 (blue)		
Color LMS511/LMS531/LMS581	RAL 7032 (grey)		
Alloy	Excellent weather resistance as per DIN EN 106:1988, plate 3		
Front screen			
Material	Polycarbonate		
Surface finish	Outside with scratch-resistant coating		

Tab. 43: Data sheet LMS5xx (cont.)

	Minimum	Typical	Maximum
System connector			
Material	GD-ALSI12 3.2582.05		
Color	RAL 9005 (black)		
Cable entries (LMS511/LMS531/LMS581)			
Material	Stainless steel/plastic		
Dimensions 5)			
Height			185 mm
Width			155 mm
Depth			160 mm
Total weight (without connection cables)		3.7 kg	
Electrical data			
SELV Supply voltage LMS5xx at the sensor accord. to IEC 60364-4-41	19.2 V	24 V	28.8 V
Permissible residual ripple			±5%
SELV Supply voltage for the LMS511/LMS531/ LMS581 heating accord. to IEC 60364-4-41	19.2 V	24 V	28.8 V
Switch on current			2 A6)
Operating current at DC 24 V		0.9 A	
Operating current with max. output load at DC 24 V		1.9 A	
Operating current with maximum heating performance at DC 24 V		3.2 A	3.8 A
Power consumption without output load at DC 24 V		22 W	25 W
Power consumption with maximum output load at DC 24 V		46 W	50 W
LMS511/LMS531/LMS581: additional power consumption of heating at DC 24 V		55 W	65 W
Electrical connection LMS511/LMS531/LMS581	4 x round M12 plug-in connectors 1x round M8 plug-in connector		
Electrical connection LMS500	1 x System connector with 2 x screw terminal blocks 1x round M8 plug-in connector		
Technical specifications, screw terminals			
Cross-section of rigid cores (American Wire Gauge – AWG)	0.14 mm^2 (approx. 26 AWG)		1.5 mm^2 (approx. 16 AWG)
Cross-section of flexible cores (American Wire Gauge – AWG)	0.14 mm^2 (approx. 26 AWG)		1.0 mm^2 (approx. 18 AWG)
Insulation stripping length for the cores		5 mm	
Screw tightening torque	0.22 Nm		0.3 Nm
Cable length for device power supply at DC 24 V			
With 1 mm^2 wire cross-section (approx. 18 AWG)			220 m
With 0.5 mm^2 wire cross-section (approx. 22 AWG)			110 m
With 0.25 mm^2 wire cross-section (approx. 24 AWG)			50 m

Tab. 43: Data sheet LMS5xx (cont.)

	Minimum	**Typical**	**Maximum**
Cable length for heating at DC 24 V			
With 1 mm^2 wire cross-section (approx. 18 AWG)			45 m
With 0.5 mm^2 wire cross-section (approx. 22 AWG)			20 m
With 0.25 mm^2 wire cross-section (approx. 24 AWG)			10 m
Cable length for device power supply at DC 12 V			
With 1 mm^2 wire cross-section (approx. 18 AWG)			20 m
With 0.5 mm^2 wire cross-section (approx. 22 AWG)			10 m
With 0.25 mm^2 wire cross-section (approx. 24 AWG)			5 m
Switching inputs			
Number	LMS500 Lite: 2 LMS500 PRO: 4 LMS511 Lite: 2 LMS511 PRO: 4 LMS511 Heavy Duty: 4 LMS531 Lite: 2 LMS531 PRO: 4 LMS581 PRO: 4		
Input voltage	11 V		30 V
Input resistance on HIGH		2 kΩ	
Voltage for HIGH	11 V	24 V	30 V
Voltage for LOW		0 V	5 V
Input capacity		15 nF	
Static input current	6 mA		15 mA
Encoder inputs (LMS5xx PRO/Heavy Duty only)			
Number	2 (IN3 and IN4)		
Input resistance on HIGH		2 kΩ	
Voltage for HIGH	11 V	24 V	30 V
Voltage for LOW	–3 V	0 V	5 V
Input capacity		1 nF	
Static input current	6 mA		15 mA
Duty cycle (Ti/T)		0.5	
Input frequency			100 kHz
Current load per incremental encoder		50 mA	100 mA
Velocity range that can be sampled			
Forward	From +100 mm/s to +20,000 mm/s		
Backward	From –10 mm/s to –20,000 mm/s		

Tab. 43: Data sheet LMS5xx (cont.)

	Minimum	Typical	Maximum
Incremental encoders that can be evaluated			
Type	Two-channel rotary encoder with 90° phase offset		
Enclosure rating	IP 54		
Supply voltage	U_V – 3 V		U_V
Outputs required on the incremental encoders	Push/pull		
Pulse frequency			100 kHz
Number of pulses per cm	50		
Cable length (shielded)			10 m
Digital switching outputs			
Number	LMS5xx Lite: 3 LMS5xx PRO: 6 LMS511 Heavy Duty: 6		
Voltage drop load		2 V	
Maximum switching current			140 mA
Current limiting (after 5 ms at 25 °C)	100 mA		200 mA
Power-up delay	Negligible		
Switch off time		0.8 ms	2 ms
Maximum current output 1 + 2 (7)			250 mA
Maximum current output 3 … 6			100 mA
Auxiliary interface			
Communication protocol	USB 2.0		
Data transmission rate (reduced)			500 kBd
Serial host interface			
Communication protocol	RS-232 (proprietary)/RS-422		
Data transmission rate (selectable)	9.6 kBd	57.6 kBd	500 kBd
Cable length at 38.4 kBd and wire cross-section 0.25 mm^2 (approx. 24 AWG)			15 m
Galvanic de-coupling	Yes		
Wire cross-section of the connection cable			0.25 mm^2 (approx. 24 AWG)
Ethernet	10/100 Mbit/s		
CAN (LMS500 PRO/LMS511 Heavy Duty only)	20 kBit/s, 500 kBit/s, 1 MBit/s		

Tab. 43: Data sheet LMS5xx (cont.)

1) Corresponds to Diamond Grade 3000X™ (approx. 1,250 cd/lx × m^2).
2) Measured under SICK standard environment (LMS2xx equivalent):
SR: temperature = 23 °C, object remission = 10% at 20 m distance
HR: temperature = 23 °C, object remission = 100% at 6 m distance
3) The time after the first reflected pulse from which measurement can be performed with full accuracy is dependent on the target that reflected the first reflected pulse.
4) Environmental conditions: good visibility, temperature range = 0 °C to 50 °C, object remission = 10 to 20.000%, ambient light < 70 klux.
5) Without fixing screws and projection of cable glands with system connector mounted.
6) 6 A for t < 50 µs.
7) Outputs are short-circuit protected (no overload protection).

Appendix 6

Specification sheet – High-speed camera body

The high-speed camera body specification sheet was provided by Deltares. For the most up-to-date version of this document, pleas refer to the manufacturer’s website: http://www.ioindustries.com/

See next page

Flare™

High Resolution Motion Capture

2MP 283fps
4MP 142fps

CoaXPress

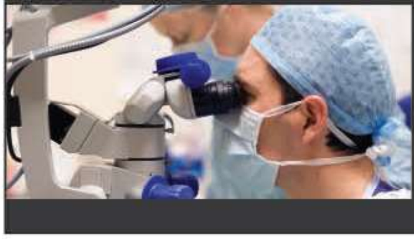

Features

- Monochrome and color models
- CoaxPress output with PoCXP support
- Selectable 8-bit or 10-bit pixel depth
- Advanced global shuttering with CDS
- High Dynamic Range modes
- Multiple ROIs and subsampling
- Low power consumption

Applications

- Inspection and monitoring
- Motion capture
- Research
- Broadcast and cinema

IO INDUSTRIES

Specifications

Camera Specifications

Camera Model	2M280 - CXP	4M140 - CXP
Sensor Size (H x V)	2048 x 1088 pixels	2048 x 2048 pixels
Frame Rate (8-bit, full resolution)	283 fps	142 fps
Optical Size	2/3"	1"
Shutter	Pipelined Global Shutter with CDS	
Pixel Size (µm)	5.5 x 5.5	
Sensor Type	60 dB CMOS	
Image Type	Mono / Color (Bayer)	
Pixel Format	8-bit or 10-bit	
Data Output Format	Dual CoaXPress up to 3.125GHz	
Link Speeds	1.25GHz, 2.5GHz, 3.125GHz	
Link Configurations	Single or Dual	
Synchronization	Via external trigger or free-run	
Exposure Control	Trigger width or timed	

Spectral Response

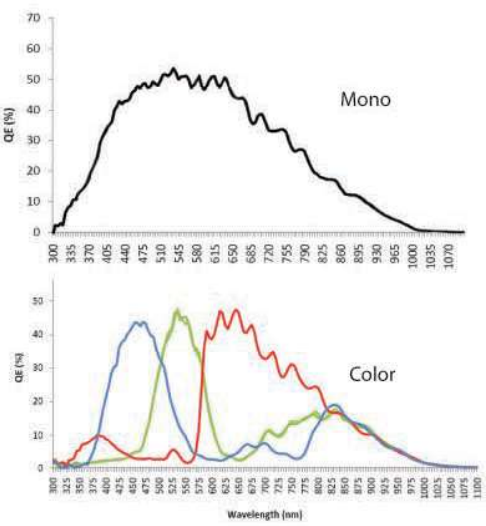

Mechanical / Electrical Specifications

Housing Size	63.5 mm x 63.5 mm x 44.1 mm
Ambient Temperature	Up to 50°C
Lens Mount	C- Mount or T-Mount
Connectors	(2) BNC, (1) 12-pin Hirose
Power Requirements	12 VDC (via Hirose or PoCXP)
Power Consumption (typical)	4.5 W
Weight (typical)	310 g

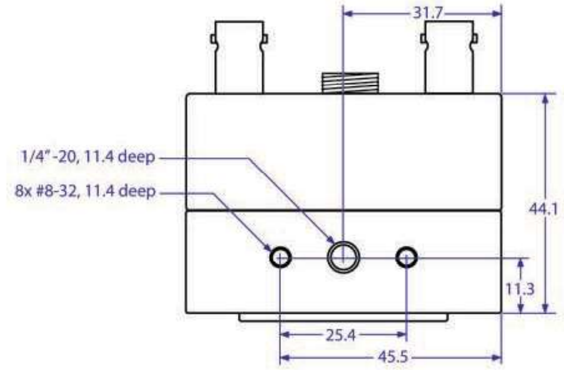

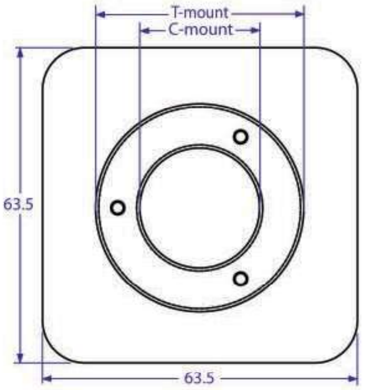

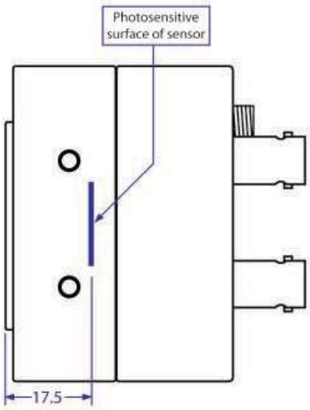

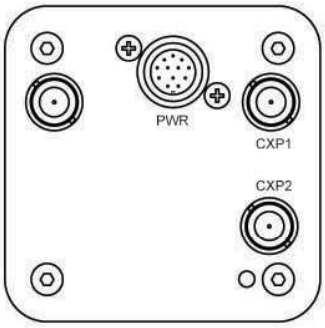

IO INDUSTRIES

1510 Woodcock Street Unit 12, London, ON, Canada N6H 5S1
Tel: +1 519 663 9570 Fax: +1 519 663 9571 info2@ioindustries.com
www.ioindustries.com

Appendix 7

Specification sheet – High-speed camera lens

The high-speed camera lens specification sheet was provided by Deltares. An up-to-date version of this document can be found at the manufacturer's website: https://www.fujifilm.eu/

See next page

For FA/Machine Vision
Fixed Focal

HF12.5SA-1

Applicable camera (model)

1	2/3	1/2	1/3	1/4
	🟥	🟥	🟥	

FIXED Fixed Focal · **5 Mega** For Megapixel Camera · **MANUAL** Manual Iris · **C-mt** C Mount · **METAL** Metal Mount · **F1.4** Wide Aperture Rate

NEW

- High-resolution design, providing support for up to 5 megapixel camera resolution.
- Rear focusing system provides improved performance in macro photography.
- Wide-aperture (F1.4) design achieves clear images under low light intensity.
- Enhanced image recognition accuracy achieved by reduction of distortion and improvement of illumination uniformity.
- Robust enclosure resistant to vibrations and shocks. Equipped with locking knobs for the iris and the focus.

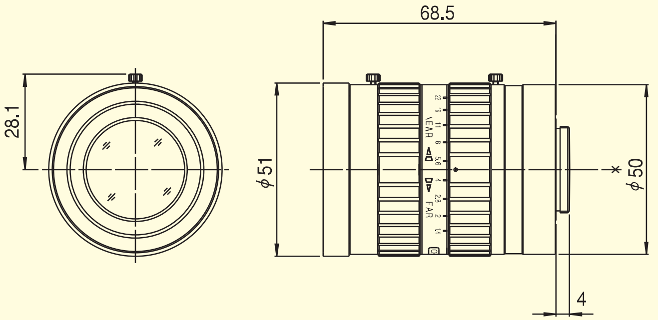

Unit : mm

Focal Length (mm)		12.5
Iris Range		F1.4 ～ F22
Operation	Focus	Manual
	Iris	Manual
Angle Of View (H×V)	2/3"	38°47′ × 29°35′
	1/2"	28°43′ × 21°44′
	1/3"	21°44′ × 16°23′
Focusing Range (From Front Of The Lens) (m)		∞ ～ 0.1
Object Dimensions at M.O.D. (H×V) (mm)	2/3"	83 × 62
	1/2"	60 × 45
	1/3"	45 × 34
Back Focal Distance (in air) (mm)		16.07
Exit Pupil Position (From Image Plane) (mm)		−101
Filter Thread (mm)		M49 × 0.75
Mount		C
Mass (g)		295

Remarks
- With Metal Mount
- With Locking Knob for Iris and Focus

Appendix 8

Specification sheet – Pressure sensors

The pressure sensors specification sheet was obtained from the internal data storage report (Streicher, 2017) distributed between participants in the WALOWA project.

See next page

MINIATURE HIGH PRESSURE PRESSURE TRANSDUCER

HKM-375 (M) SERIES

- Excellent Stability
- All Welded Construction
- Silicon on Silicon Integrated Sensor **VIS**®
- Robust Construction
- High Natural Frequencies
- 3/8-24 UNJF or M10 X 1 Thread
- Intrinsically Safe Applications Available (i.e. IS-HKM-375)

The HKM-375 is a miniature threaded pressure transducer. The hexagonal head and o-ring seal make it easy to mount and simple to apply.

The HKM-375 utilizes a flush metal diaphragm as a force collector. A solid state piezoresistive sensing element is located immediately behind this metal diaphragm which is protected by a metal screen. Force transfer is accomplished via non-compressible silicone oil. This sensing sub assembly is welded to a stainless steel body.

This advanced construction results in a highly stable, reliable and rugged instrument with all the advantages of significant miniaturization, excellent repeatability, low power consumption, etc. The miniaturization process also yields a marked increase in the natural frequencies of the transducers, making them suitable for use even in shock pressure measurements.

Kulite recommends the KSC-2 signal conditioner to maximize the measurement capability of the HKM-375 transducer.

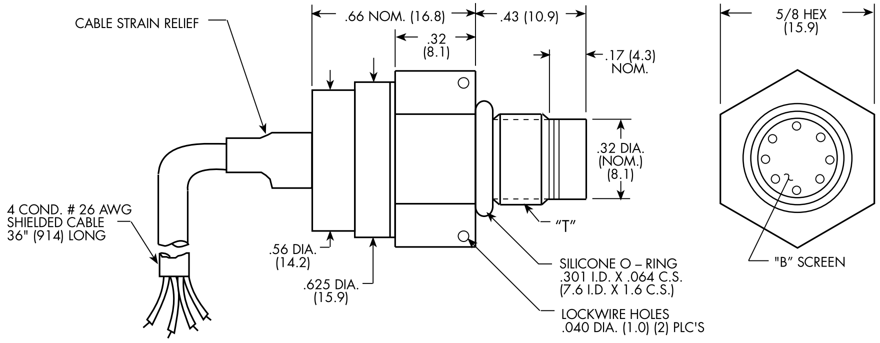

COLOR	DESIGNATION
RED	+ INPUT
BLACK	- INPUT
GREEN	+ OUTPUT
WHITE	- OUTPUT

P/N	"T"
375	3/8-24 UNJF-3A
375M	M 10 x 1

INPUT	Pressure Range	17 250	35 500	70 1000	170 2500	350 5000	700 10000	1400 BAR 20000 PSI
	Operational Mode	Absolute, Sealed Gage						
	Over Pressure	2 Times Rated Pressure to 1000 PSI (70 BAR) 1.5 Times Rated Pressure Above 1000 PSI to a Max. of 30000 PSI (2100 BAR)						
	Burst Pressure	3 Times Rated Pressure to a Max. of 35000 PSI (2400 BAR)						
	Pressure Media	Any Liquid or Gas Compatible With 15-5 PH or 316 Stainlesss Steel (All Media May Not Be Suitable With O-Ring Supplied)						
	Rated Electrical Excitation	10 VDC/AC						
	Maximum Electrical Excitation	12 VDC/AC						
	Input Impedance	1000 Ohms (Min.)						
OUTPUT	Output Impedance	1000 Ohms (Nom.)						
	Full Scale Output (FSO)	100mV (Nom.)						
	Residual Unbalance	± 5 mV (Typ.)						
	Combined Non-Linearity, Hysteresis and Repeatability	± 0.1% FSO BFSL (Typ.), ± 0.5% FSO (Max.)						
	Resolution	Infinitesimal						
	Natural Frequency of Sensor Without Screen (KHz) (Typ.)	Greater Than 400 KHz						
	Acceleration Sensitivity % FS/g Perpendicular	2.2x10^{-4}	1.1x10^{-4}	6.2x10^{-5}	2.6x10^{-5}	1.5x10^{-5}	1.3x10^{-5}	8.0x10^{-6}
	Insulation Resistance	100 Megohm Min. @ 50 VDC						
ENVIRONMENTAL	Operating Temperature Range	-65°F to +250°F (-55°C to +120°C)						
	Compensated Temperature Range	+80°F to +180°F (+25°C to +80°C) Any 100°F Range Within The Operating Range on Request						
	Thermal Zero Shift	± 1% FS/100° F (Typ.)						
	Thermal Sensitivity Shift	± 1% /100° F (Typ.)						
	Linear Vibration	10-2,000 Hz Sine, 100g. (Max.)						
	Mechanical Shock	20g half Sine Wave 11 msec. Duration						
PHYSICAL	Electrical Connection	4 Conductor 26 AWG Shielded Cable 36" Long						
	Weight	17 Grams (Max.) Excluding Cable						
	Pressure Sensing Principle	Fully Active Four Arm Wheatstone Bridge Dielectrically Isolated Silicon on Silicon						
	Mounting Torque	80 Inch-Pounds (Max.) 9 Nm						

Note: Custom pressure ranges, accuracies and mechanical configurations available. Dimensions are in inches. Dimensions in parenthesis are in millimeters. All dimensions nominal. (M)

Continuous development and refinement of our products may result in specification changes without notice.

Kulite miniature pressure transducers are intended for use in test and research and development programs and are not necessarily designed to be used in production applications. For products designed to be used in production programs, please consult the factory.

Appendix 9

Specification sheet – Load cells

The load cells specification sheet was obtained from the internal data storage report (Streicher, 2017) distributed between participants in the WALOWA project.

See next page

Deltares
Enabling Delta Life

Calibration-certificate transducer U9 01.06.298

Date : Wed 11/Jan/2017 10:45:19
Observer : Kop
Calibr. type : load
Rej. Cr. (FS) : +/- 0.5%(lin),+/- 5% (offset)
File-number : 201701111035_K
Kpl / CO Nr : 10000514

Reference transducer

Brand	:	MTS	
Type	:	661.13A-08	
Serial Number	:	3001 B	
Full Scale	:	2	kN
Due to	:	2018-08-08	

Calibrated transducer

Brand	:	HBM	
Type	:	U9	
Serial Number	:	01.06.298	
Full Scale	:	2.000	kN
Due to	:	11/Jan/2018	

Calibration circumstances

Calibrated scale	:	2.000	kN
Excitation	:	N.V.T	V
Cable length	:	5.0	m
Temperature	:	21.5	°C
Ambient air pressure	:	1009.1	mbar

Calculated according to the smallest square method with fixed zero point

Measurement unit	:	kN	
Engineering unit	:	kN	
Sensitivity ref. transd.	:	1.0000	kN / kN
Sensitivity	:	185.918198	mV/kN
Reciproke Sensitivity	:	0.005379	kN/mV
Offset	:	-1122.839966	mV
Maximum abs. error	:	0.007	kN
Maximum rel. error	:	0.363	% FS

Checked by
Date
Approved by
Date

Identification code 300-P-Y1-F1
Version Cal. program 2.0
Start Date 01-02-2010
Page 1 of 2

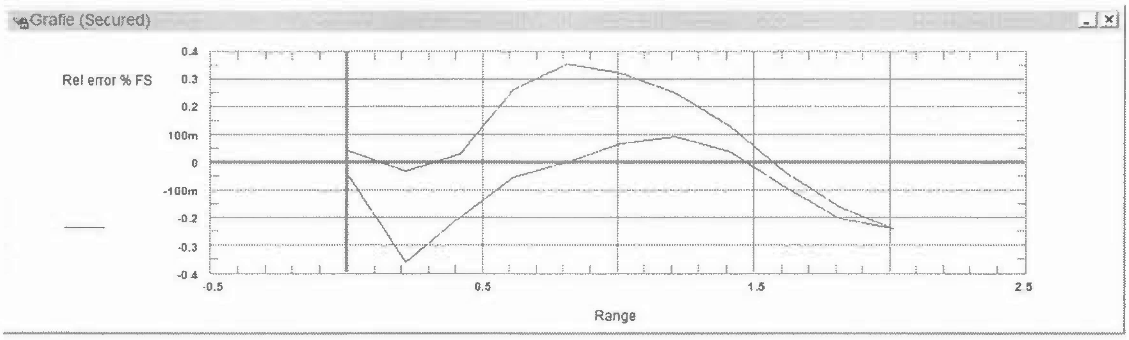

Results of 21 point calibration for a load transducer

Excitation 1.000 V

Reference transducer kN	Reference transducer kN	Calibration value mV	Calculated value kN	Absolute error % FS	Absolute error kN
-0.0005	-0.0005	-1123.1000	-0.0014	-0.0436	-0.0009
0.2131	0.2131	-1084.5800	0.2058	-0.3635	-0.0073
0.4129	0.4129	-1046.8101	0.4089	-0.1995	-0.0040
0.6126	0.6126	-1009.1400	0.6116	-0.0503	-0.0010
0.8120	0.8120	-971.8720	0.8120	0.0023	0.0000
1.0116	1.0116	-934.5170	1.0129	0.0691	0.0014
1.2108	1.2108	-897.3830	1.2127	0.0950	0.0019
1.4107	1.4107	-860.4190	1.4115	0.0389	0.0008
1.6107	1.6107	-823.7220	1.6089	-0.0900	-0.0018
1.8117	1.8117	-786.7590	1.8077	-0.2013	-0.0040
2.0106	2.0106	-749.9240	2.0058	-0.2406	-0.0048
1.8110	1.8110	-786.7440	1.8078	-0.1633	-0.0033
1.6120	1.6120	-823.2760	1.6113	-0.0355	-0.0007
1.4122	1.4122	-859.8080	1.4148	0.1302	0.0026
1.2130	1.2130	-896.3710	1.2181	0.2547	0.0051
1.0133	1.0133	-933.2390	1.0198	0.3233	0.0065
0.8141	0.8141	-970.1610	0.8212	0.3578	0.0072
0.6148	0.6148	-1007.5500	0.6201	0.2649	0.0053
0.4156	0.4156	-1045.4600	0.4162	0.0320	0.0006
0.2156	0.2156	-1082.8800	0.2149	-0.0329	-0.0007
0.0005	0.0005	-1122.5800	0.0014	0.0436	0.0009

Appendix 10

Discrepancy in water elevation measurements

Throughout the completion of this thesis, data related to test WLW_Irr_1_F from several measurement instruments became available as more and more participants in the WALOWA project shared their post-processed results. An apparent discrepancy was observed in the water free surface measurements from the wave gauge positioned at the dike toe (termed *WHM14* in Appendix 3; positioned lengthwise at X = 174.75 m in GCS, or about 0.35 m before the dike toe). This is shown in Figure 56, which was provided by Tomohiro Suzuki. There, a discrepancy in the water surface elevation *η* (‘*eta*’ in Figure 56) is visible, which develops in time (approximately) as follows: start at *t* = 830 s; peak at *t* = 1595 s; end at *t* = 2830 s; *t* = 0 corresponds to start of test WLW_Irr_1_F. Initially, it was unclear whether this is caused by erroneous measurements or an actual phenomenon such as e.g. wave-induced set-up at the dike toe. Furthermore, two of the analysed highest impact events – L3 and L4, are located very close to the above mentioned peak discrepancy. A set-up at the dike toe with a magnitude as suggested by Figure 56 would considerably change the conditions at the dike toe, and therefore the post-overtopping flow parameters.

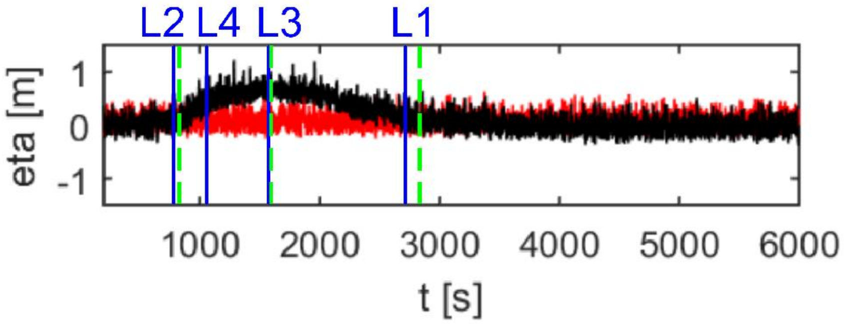

Figure 56: Discrepancy in the measured instantaneous water surface elevation η by the wave gauge at the dike toe. The black signal is the wave gauge measurement, where the discrepancy start, peak and end are indicated by the green lines. The red signal is a comparison with a SWASH numerical model where no such ‘set-up’ is observed. The blue lines indicate the times when impacts L1 to L4 occurred. Source image provided by Tomohiro Suzuki.

It was considered paramount to determine whether this discrepancy was linked to a physical phenomenon or not. To enable this, four segments in time recorded by the laser scanner were chosen, and the averaged water surface elevation at the dike toe obtained (Table 23 and Figure 57). The results in Table 23 indicate that there was no discernible change in the (averaged) water elevation, certainly not within the range suggested by the wave gauge measurements, which is in the order of 70 cm.

Table 23: Obtaining averaged water level elevation measurements, showing the segments of the laser scanner recording used for the comparison and average η values. No discrepancy was observed.

	Timeframe covered					
	Start [s]	**Stop [s]**	**Total [s]**	**Measured h_{toe} during the test [cm]**	**Average h_{toe} for recording segment**	**Average η for recording segment [cm]**
Before discrepancy	468	624	156	28	33.0	5.0
During peak discrepancy	1562	1718	156	28	32.5	4.5
After discrepancy	3280	3437	157	28	34.5	6.5
Long after discrepancy	4687	4843	156	28	32.1	4.1

The discrepancy in *η* can therefore reasonably be attributed to erroneous measurements by the wave gauge instrument. The cause of this is suspected to be linked to temperature changes, as suggested by WALOWA-involved technicians. Although it is suggested that further investigations are conducted, including whether similar discrepancies are observed during other tests, this is outside the scope of the current work.

a. Before discrepancy Timeframe = 468 to 624 s

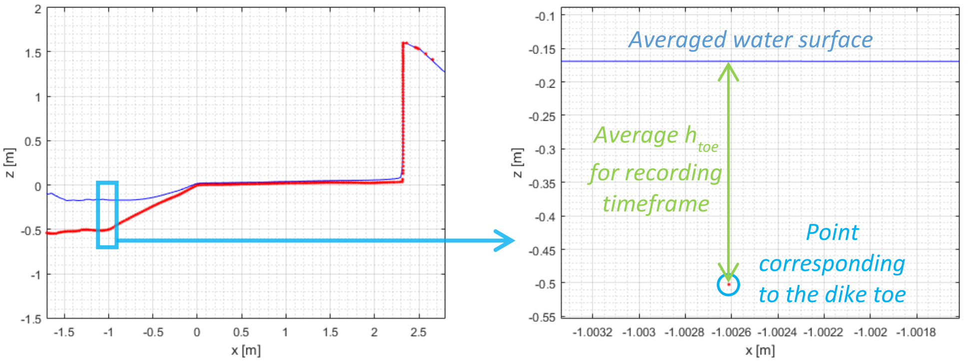

b. During peak discrepancy Timeframe = 1562 to 1718 s

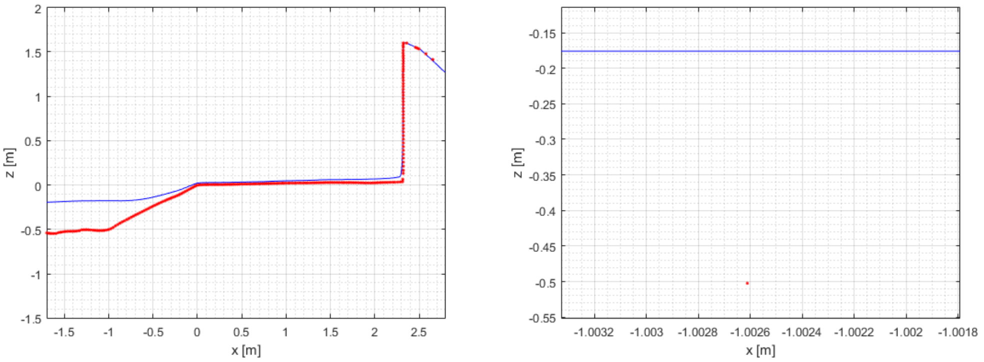

c. After discrepancy Timeframe = 3280 to 3437 s

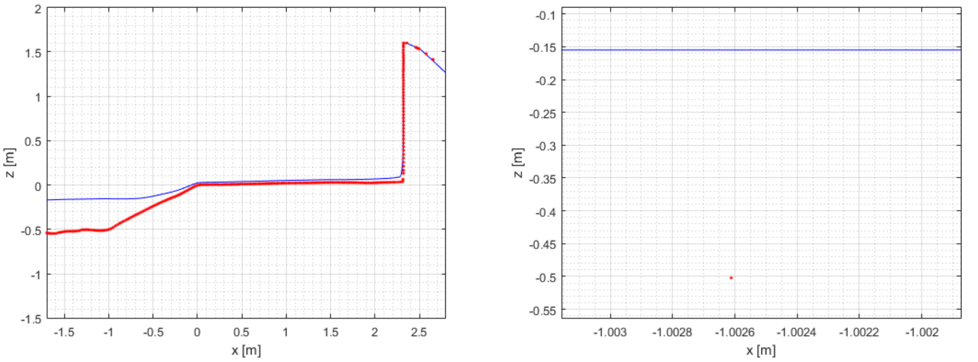

d. Long after discrepancy Timeframe = 4687 to 4843 s

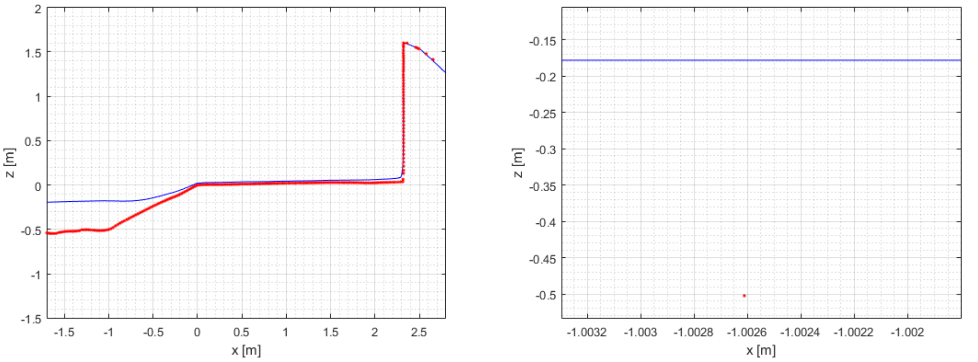

Figure 57: Obtaining averaged water level elevation measurements for segments of the laser scanner recording before (a.), during (b.) and after (c. and d.) the discrepancy in the η values. The red dots represent the model profile and the blue line – the water surface averaged over the specified timeframe. Values are presented in Table 23. No discrepancy in η was found.

Appendix 11

Timesteps of L3 and L4 large scale impacts

The timesteps of pre-impact flow evolution for impacts L3 and L4 are presented in Figure 58 and Figure 59, respectively. Data is from the laser scanner. Timesteps are given relative to the time of impact: *t* = 0 s – moment of impact. Blue line indicates the water surface, red line – the model profile. Black arrows indicate the two distinct wave crests, grey arrows the accelerated bore front of the first overtopping wave. Profile obtained from laser scanner recording. Coordinates in LCS.

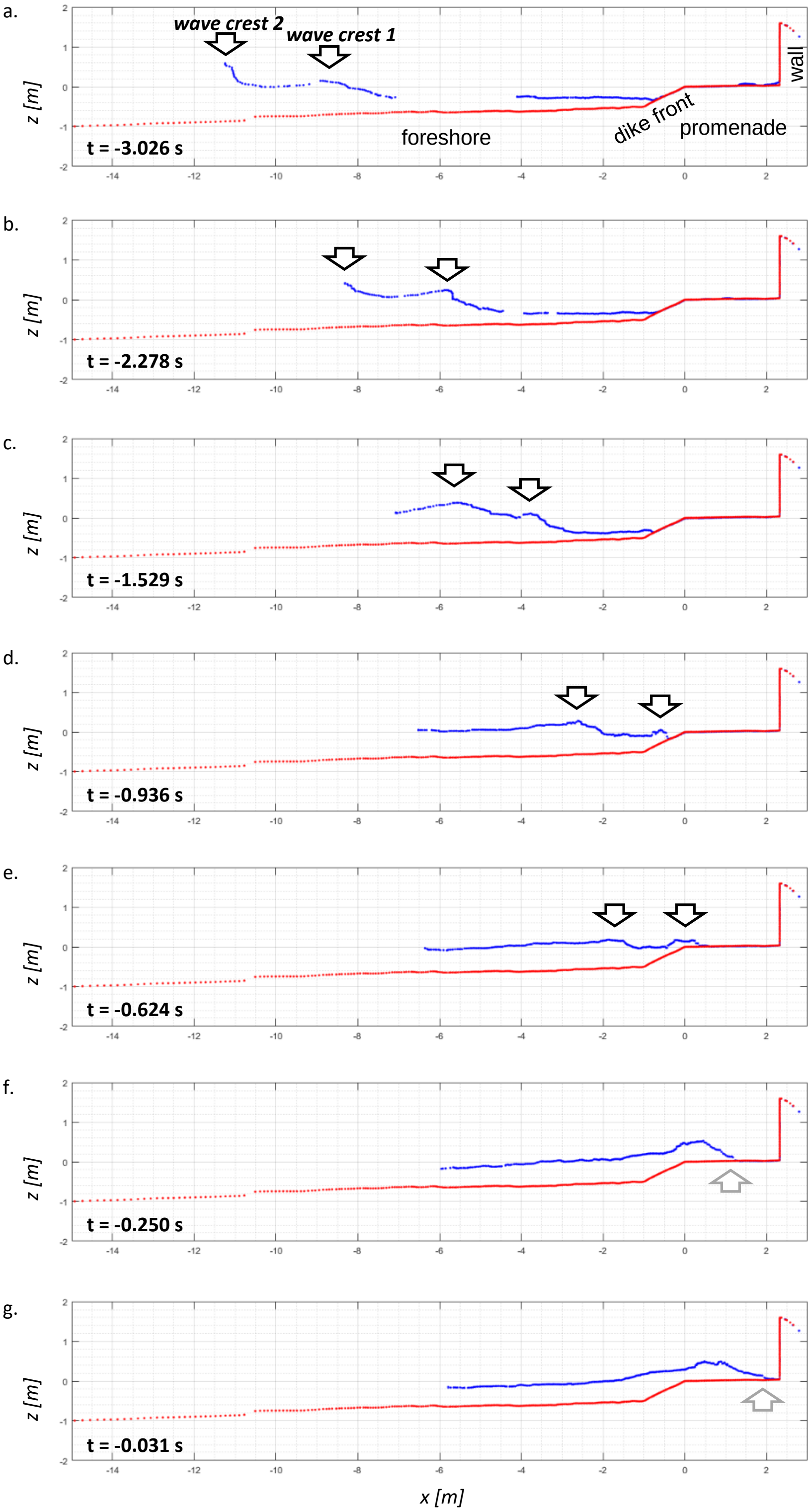

Figure 58: Laser scanner obtained profile of the propagation and overtopping of the two waves that caused the third largest peak impact force at large scale (L3).

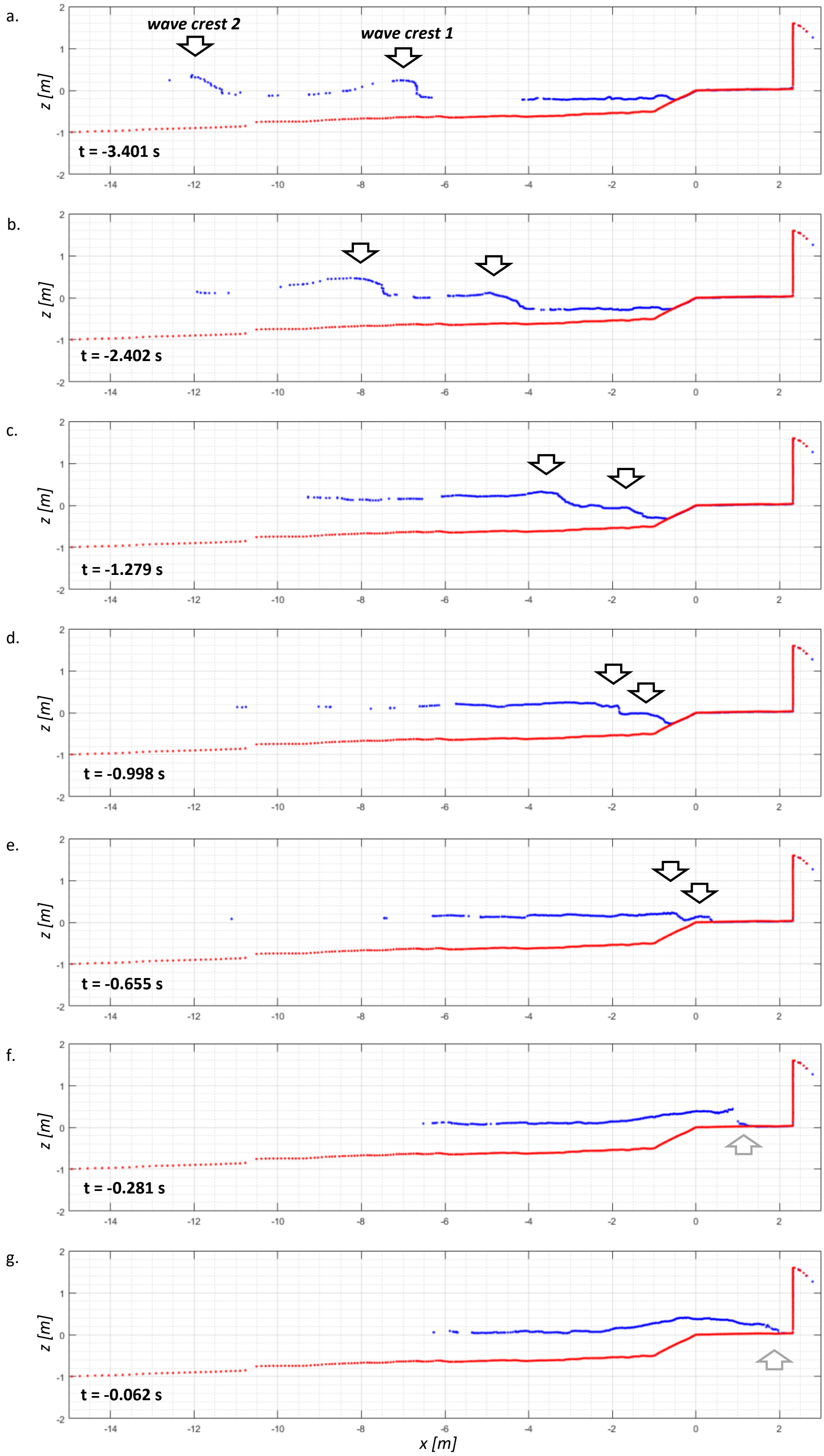

Figure 59: Laser scanner obtained profile of the propagation and overtopping of the two waves that caused the fourth largest peak impact force at large scale (L4).

Notable in the above figures is the similar catch-up phenomenon observed for both events. Even though this occurred at an almost identical point longitudinally – just after the dike crest, the peak force classification for the two events differed (Figure 60). L3 was classified as a *dynamic bore impact*, while L4 as *quasi-static/down-rush bore impact* (Streicher et al., 2016). This is an indication that the type of impact at the wall is governed by an additional factor(s), and not directly linked to the overtopping mechanism itself. Furthermore, this does not appear to be the averaged bore velocity alone, since this was estimated to be very similar between the two events, as shown below.

- $U_{b,avg}$ = 2.85 m/s for L3;
- $U_{b,avg}$ = 2.79 m/s for L4.

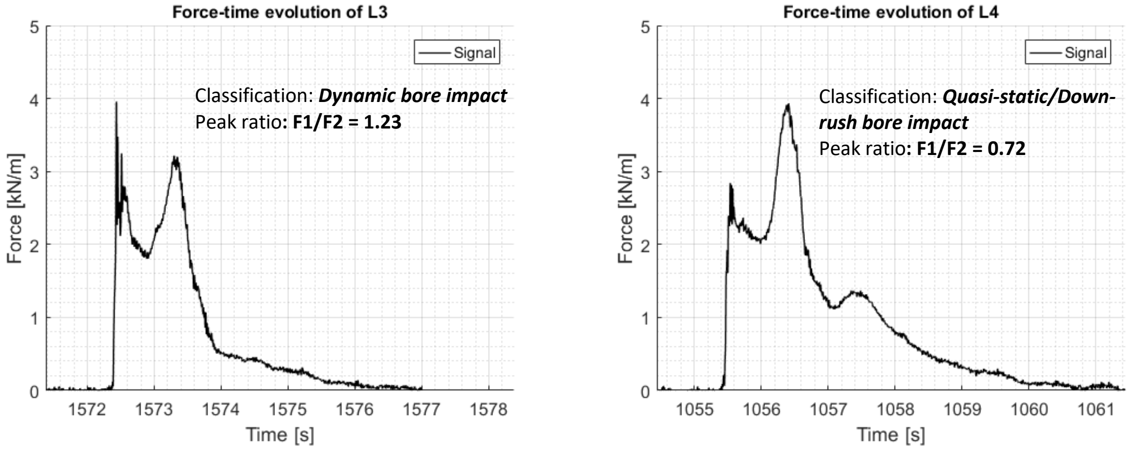

Figure 60: The force-time signal for the impact events L3 (left) and L4 (right). Load cell data for test WLW_Irr_1_F.

Appendix 12

Timesteps of S3 and S4 small scale impacts

The timesteps for the pre-impact flow evolution of impacts L3 and L4 are presented in Figure 61 and Figure 62, respectively.

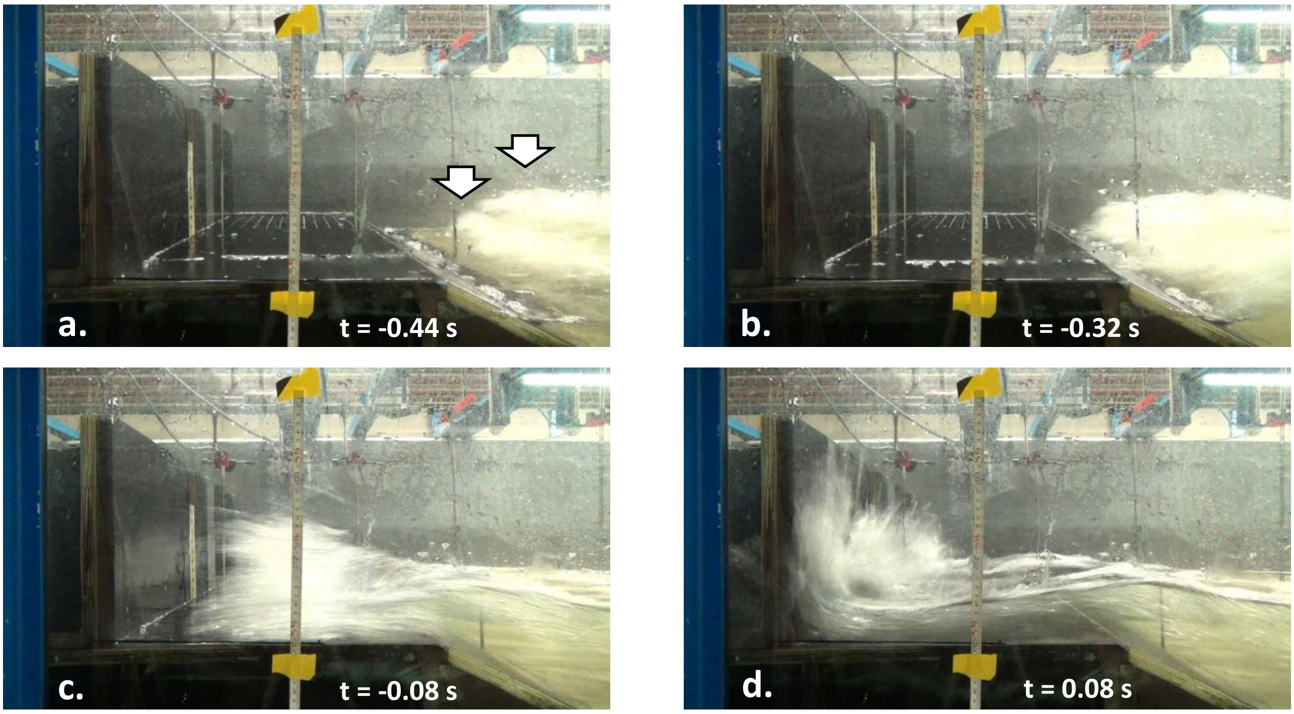

Figure 61: Selected frames from the pre- and post-impact flow for the third largest small scale test impact (S3). Images captured by side-mounted camera. Timecode relative to moment of impact t_0 = 1899.81 s (time corresponding to 1:25 scale). The arrows indicate the two wave crests just before catch-up occurs.

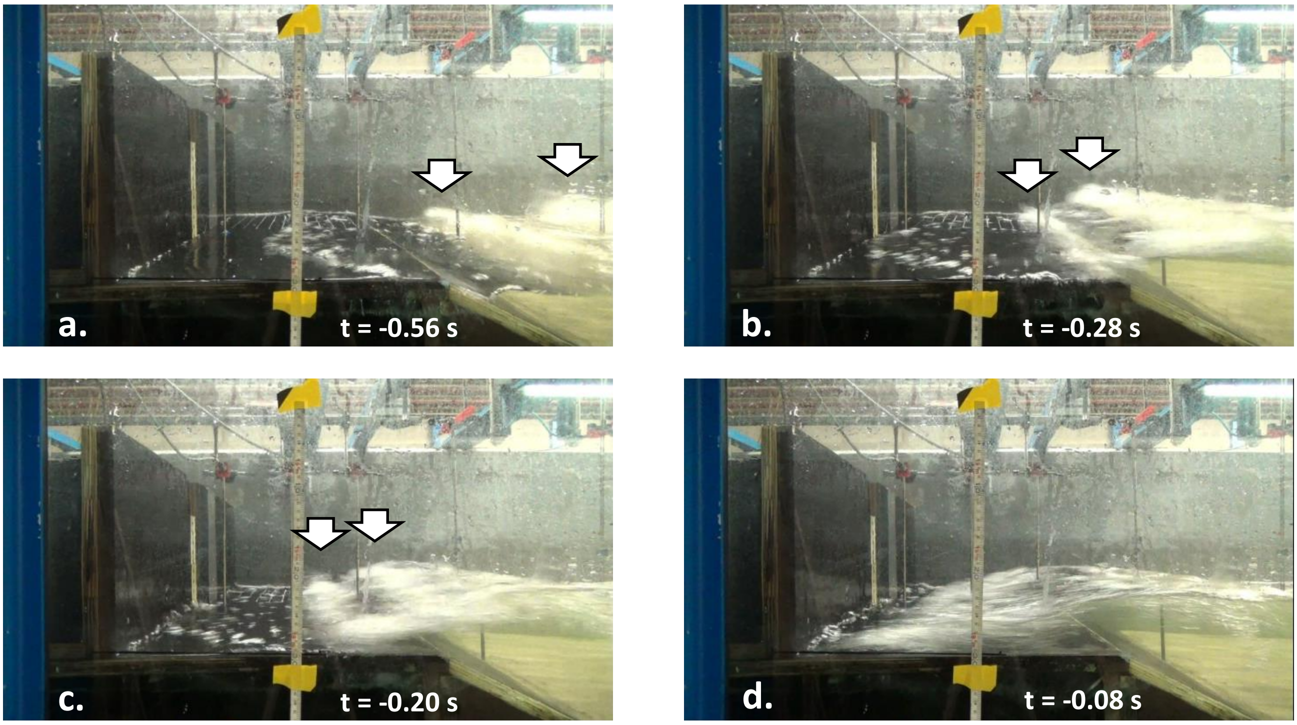

Figure 62: Selected frames from the pre-impact flow evolution for the fourth largest small scale test impact (S4). Images captured by side-mounted camera. Timecode relative to moment of impact t_0 = 2501.34 s (time corresponding to 1:25 scale). The arrows indicate the two wave crests before catch-up occurs.

A wave catch-up can be observed at the foreshore (before reaching the dike front) for L3. The post-overtopping flow exhibits a non-uniform bore front, where initial contact with the wall is facilitated by individual splashes of water. A similar bore front non-uniformity was observed for impact S2, where again the dominant peak in the force-time signal is the *quasi-static impact peak*. For S2, the wave catch-up was also observed before the dike crest. Based on the current observations, it is likely that this can be linked to the comparatively lower first peak in the signal (*dynamic force peak*) – refer to Section 4.2.3.

In comparison, S4 exhibits a uniform bore front propagating towards the wall before the impact occurs. This was also the case for S1, the largest small scale test impact. The force-time signals for both S1 and S4 show a dominant *dynamic impact peak*. The location of catch-up is also similar to the one observer for impact events L1, L3 and L4 at large scale. Moreover, this is related to the ‘efficient overtopping’ phenomenon described in Chapter 4, where a direct impact with the dike front is negated for the second of the two waves. It therefore appears that these two factors (wave catch-up after the dike crest, which in turn results in ‘efficient overtopping’) relate to the relative bore front uniformity (or reduced break-up of the bore front into separate splashes of water) of the post-overtopping pre-impact flow.

Appendix 13

Sensitivity analysis of impact force peaks ratio threshold

Typically, a double-peaked force-time signal evolution is observed for a wave-structure impact (e.g. Chen et al., 2012, 2014). A classification based on the ratio of the magnitude of these peaks was proposed by Streicher et al. (2016). The threshold ratio for the transition between *dynamic* and *quasi-static/down-rush bore impact* was set by Streicher et al. (2016) to F_1/F_2 = 1.2. It was however unclear whether (and how) this threshold value affects the distribution of the impact classification between the two scaled tests. Therefore, a sensitivity analysis with threshold values between 1.0 and 2.4 was conducted for the 10% largest impacts for the WLW_Irr_1_F test and its corresponding small scale counterpart.

Note that here the 10% limit is related to the total number of discernible impact events at each scale, meaning the highest 53 impacts at large scale and highest 57 impacts at small scale. This decision was made due to the more similar lower magnitude threshold equating to 1.43 kN/m (for the 53rd impact at large scale) and 1.59 kN/m (for the 57th impact at small scale). Nevertheless, use of an alternate definition of the 10% highest impacts, one related to a high pass threshold of 0.13 kN/m (see Section 4.1.), which reduces the highest 10% small scale impacts count to 44, was also conducted. Since no major differences were observed, this analysis is not presented in this work, and it was concluded that the 10% threshold value related to the total number of discernible impacts can be considered representative.

It was observed that regardless of the peak ratio threshold value chosen, the distribution of the classification of impacts between the two tests does not show large variations. Results of the sensitivity analysis are presented in Figure 63 and Table 24. The impact events this analysis was based on are presented in Table 25.

Table 24: Results of the sensitivity analysis for the peak ratio threshold used for the classification of bore impact types.

Large scale test (based on highest 53 impacts)				
Peak ratio threshold	**Impact classification**			
	Dynamic bore impact		**Quasi-static/down-rush bore impact**	
	Number of impacts	**Proportion [%]**	**Number of impacts**	**Proportion [%]**
1.0	19	36	34	64
1.2	16	30	37	70
1.4	6	11	47	89
1.6	3	6	50	94
1.8	3	6	50	94
2.0	3	6	50	94
2.4	1	2	52	98

Small scale test (based on highest 57 impacts)				
Peak ratio threshold	**Impact classification**			
	Dynamic bore impact		**Quasi-static/down-rush bore impact**	
	Number of impacts	**Proportion [%]**	**Number of impacts**	**Proportion [%]**
1.0	20	35	37	65
1.2	15	26	42	74
1.4	10	18	47	82
1.6	6	11	51	89
1.8	2	4	55	96
2.0	1	2	56	98
2.4	0	0	57	100

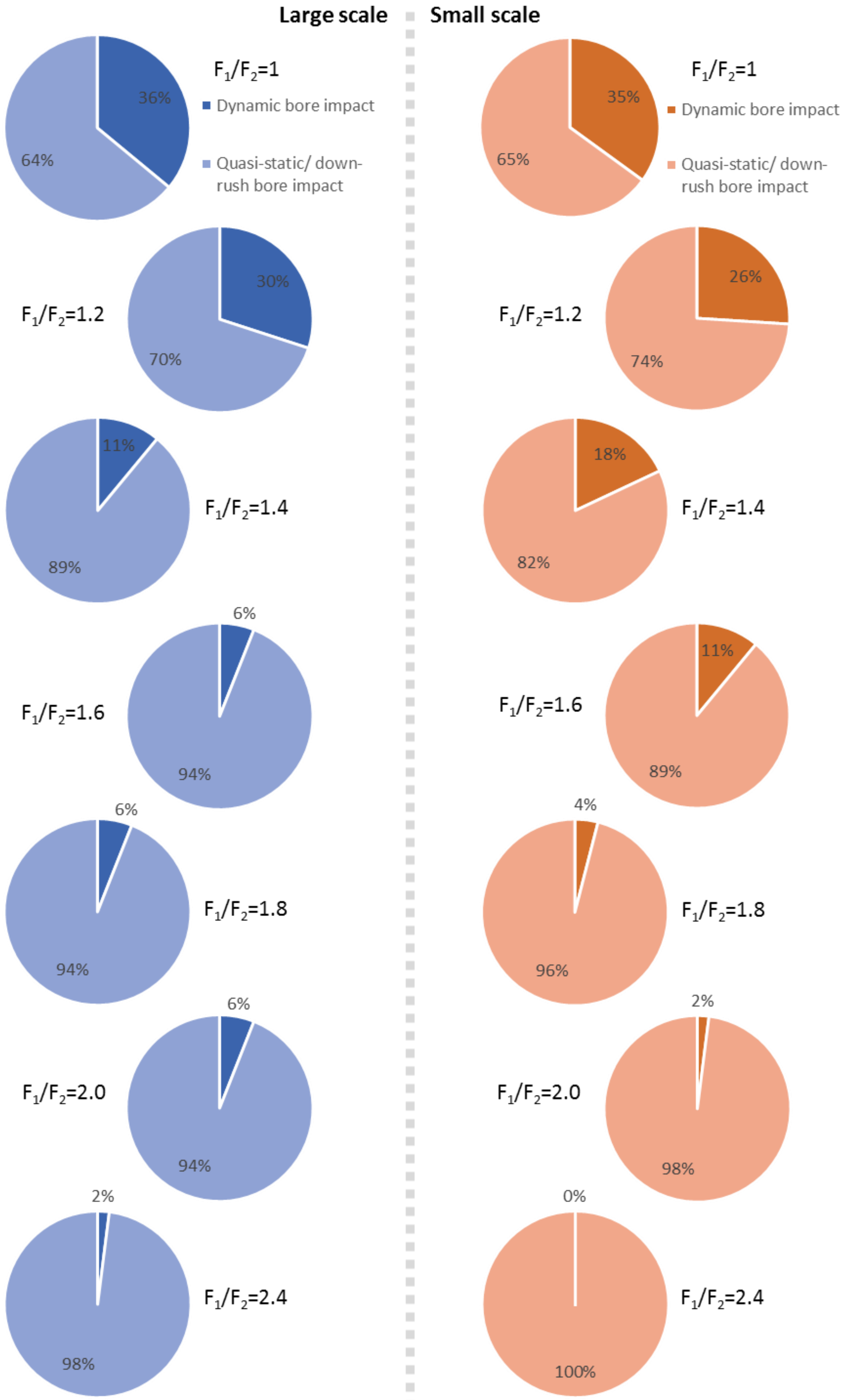

Figure 63: Ratio of dynamic to quasi-static/down-rush bore impacts for the large scale (left) and small scale (right) test for varying threshold impact peak ratios (1.0 to 2.4). Results based on 53 and 57 highest impacts (large and small scale, respectively) corresponding to highest 10% of discernible events.

Table 25: Highest 10% of all discernible impacts at both small and large scale, in descending order of magnitude. Impact force peak values from load cells. Classification here is after Streicher et al. (2016) with peak ratio threshold of 1.2.

Highest 10% of impacts - Large scale test (531 impacts in total)

Impact ranking (Descending)	P_i	First peak (F_1)	Second peak (F_2)	Peak ratio (F_1/F_2)	Classification after Streicher et al. (2016)
1	0.002	4.59	2.26	2.03	dynamic bore impact
2	0.004	3.08	4.46	0.69	quasi-static/ down-rush bore impact
3	0.006	3.96	3.22	1.23	dynamic bore impact
4	0.008	2.84	3.93	0.72	quasi-static/ down-rush bore impact
5	0.009	3.65	2.44	1.50	dynamic bore impact
6	0.011	3.52	3.25	1.08	quasi-static/ down-rush bore impact
7	0.013	3.22	1.50	2.14	dynamic bore impact
8	0.015	3.05	2.28	1.34	dynamic bore impact
9	0.017	2.99	2.25	1.33	dynamic bore impact
10	0.019	2.01	2.91	0.69	quasi-static/ down-rush bore impact
11	0.021	1.70	2.84	0.60	quasi-static/ down-rush bore impact
12	0.023	2.72	2.07	1.31	dynamic bore impact
13	0.024	1.91	2.65	0.72	quasi-static/ down-rush bore impact
14	0.026	2.39	2.57	0.93	quasi-static/ down-rush bore impact
15	0.028	2.51	1.76	1.43	dynamic bore impact
16	0.030	1.70	2.39	0.71	quasi-static/ down-rush bore impact
17	0.032	2.01	2.38	0.84	quasi-static/ down-rush bore impact
18	0.034	2.36	1.55	1.52	dynamic bore impact
19	0.036	1.64	2.34	0.70	quasi-static/ down-rush bore impact
20	0.038	1.91	2.24	0.85	quasi-static/ down-rush bore impact
21	0.039	1.66	2.21	0.75	quasi-static/ down-rush bore impact
22	0.041	2.15	0.79	2.72	dynamic bore impact
23	0.043	1.29	2.13	0.60	quasi-static/ down-rush bore impact
24	0.045	1.78	2.09	0.85	quasi-static/ down-rush bore impact
25	0.047	2.00	2.08	0.96	quasi-static/ down-rush bore impact
26	0.049	1.50	2.07	0.72	quasi-static/ down-rush bore impact
27	0.051	1.65	2.06	0.80	quasi-static/ down-rush bore impact
28	0.053	2.06	1.52	1.35	dynamic bore impact
29	0.055	2.03	1.62	1.26	dynamic bore impact
30	0.056	1.29	2.02	0.64	quasi-static/ down-rush bore impact
31	0.058	2.00	1.86	1.08	quasi-static/ down-rush bore impact
32	0.060	1.05	2.00	0.53	quasi-static/ down-rush bore impact
33	0.062	1.46	1.99	0.73	quasi-static/ down-rush bore impact
34	0.064	1.97	1.46	1.35	dynamic bore impact
35	0.066	1.23	1.95	0.63	quasi-static/ down-rush bore impact
36	0.068	1.51	1.88	0.80	quasi-static/ down-rush bore impact
37	0.070	1.81	1.48	1.22	dynamic bore impact
38	0.071	1.07	1.81	0.59	quasi-static/ down-rush bore impact
39	0.073	1.44	1.76	0.82	quasi-static/ down-rush bore impact

40	0.075	1.57	1.75	0.90	quasi-static/ down-rush bore impact
41	0.077	1.15	1.74	0.66	quasi-static/ down-rush bore impact
42	0.079	1.00	1.71	0.59	quasi-static/ down-rush bore impact
43	0.081	1.70	1.49	1.14	quasi-static/ down-rush bore impact
44	0.083	1.28	1.60	0.80	quasi-static/ down-rush bore impact
45	0.085	1.09	1.59	0.69	quasi-static/ down-rush bore impact
46	0.086	1.58	1.29	1.23	dynamic bore impact
47	0.088	1.25	1.57	0.79	quasi-static/ down-rush bore impact
48	0.090	1.57	1.24	1.27	dynamic bore impact
49	0.092	1.44	1.55	0.93	quasi-static/ down-rush bore impact
50	0.094	1.26	1.54	0.81	quasi-static/ down-rush bore impact
51	0.096	1.10	1.51	0.73	quasi-static/ down-rush bore impact
52	0.098	1.04	1.47	0.71	quasi-static/ down-rush bore impact
53	0.100	1.14	1.43	0.79	quasi-static/ down-rush bore impact

Highest 10% impacts - Small scale test (572 impacts in total)

Impact ranking (Descending)	P_i	First peak (F_1)	Second peak (F_2)	Peak ratio (F_1/F_2)	Classification after Streicher et al. (2016)
1	0.002	4.92	3.89	1.26	dynamic bore impact
2	0.003	2.27	4.74	0.48	quasi-static/ down-rush bore impact
3	0.005	3.39	4.63	0.73	quasi-static/ down-rush bore impact
4	0.007	3.79	3.25	1.16	quasi-static/ down-rush bore impact
5	0.009	2.64	3.53	0.75	quasi-static/ down-rush bore impact
6	0.010	2.46	3.30	0.75	quasi-static/ down-rush bore impact
7	0.012	2.59	3.14	0.82	quasi-static/ down-rush bore impact
8	0.014	1.87	3.06	0.61	quasi-static/ down-rush bore impact
9	0.016	2.89	1.42	2.04	dynamic bore impact
10	0.017	2.82	2.12	1.33	dynamic bore impact
11	0.019	2.77	1.81	1.53	dynamic bore impact
12	0.021	2.68	2.23	1.20	dynamic bore impact
13	0.023	2.64	2.67	0.99	quasi-static/ down-rush bore impact
14	0.024	2.23	2.55	0.88	quasi-static/ down-rush bore impact
15	0.026	1.65	2.48	0.66	quasi-static/ down-rush bore impact
16	0.028	1.37	2.48	0.55	quasi-static/ down-rush bore impact
17	0.030	2.07	2.45	0.84	quasi-static/ down-rush bore impact
18	0.031	2.40	1.68	1.43	dynamic bore impact
19	0.033	2.38	1.37	1.74	dynamic bore impact
20	0.035	2.35	2.10	1.12	quasi-static/ down-rush bore impact
21	0.037	1.43	2.29	0.62	quasi-static/ down-rush bore impact
22	0.038	1.96	2.27	0.86	quasi-static/ down-rush bore impact
23	0.040	2.24	1.14	1.97	dynamic bore impact
24	0.042	1.92	2.22	0.87	quasi-static/ down-rush bore impact
25	0.044	1.57	2.20	0.71	quasi-static/ down-rush bore impact
26	0.045	2.11	2.20	0.96	quasi-static/ down-rush bore impact
27	0.047	1.18	2.17	0.55	quasi-static/ down-rush bore impact

28	0.049	1.30	2.16	0.60	quasi-static/ down-rush bore impact
29	0.051	1.91	2.15	0.89	quasi-static/ down-rush bore impact
30	0.052	1.67	2.15	0.77	quasi-static/ down-rush bore impact
31	0.054	1.67	2.10	0.79	quasi-static/ down-rush bore impact
32	0.056	1.91	2.09	0.91	quasi-static/ down-rush bore impact
33	0.058	2.07	1.76	1.18	quasi-static/ down-rush bore impact
34	0.059	1.74	2.07	0.84	quasi-static/ down-rush bore impact
35	0.061	1.45	2.04	0.71	quasi-static/ down-rush bore impact
36	0.063	1.84	1.92	0.96	quasi-static/ down-rush bore impact
37	0.065	1.90	1.61	1.18	quasi-static/ down-rush bore impact
38	0.066	1.89	1.07	1.77	dynamic bore impact
39	0.068	1.85	1.42	1.30	dynamic bore impact
40	0.070	1.84	1.07	1.72	dynamic bore impact
41	0.072	1.17	1.83	0.64	quasi-static/ down-rush bore impact
42	0.073	1.45	1.83	0.80	quasi-static/ down-rush bore impact
43	0.075	1.34	1.81	0.74	quasi-static/ down-rush bore impact
44	0.077	1.56	1.80	0.87	quasi-static/ down-rush bore impact
45	0.079	1.80	1.79	1.00	quasi-static/ down-rush bore impact
46	0.080	1.76	1.80	0.98	quasi-static/ down-rush bore impact
47	0.082	1.22	1.78	0.68	quasi-static/ down-rush bore impact
48	0.084	1.19	1.77	0.67	quasi-static/ down-rush bore impact
49	0.086	1.40	1.76	0.80	quasi-static/ down-rush bore impact
50	0.087	1.20	1.74	0.69	quasi-static/ down-rush bore impact
51	0.089	1.67	1.03	1.62	dynamic bore impact
52	0.091	1.67	1.07	1.56	dynamic bore impact
53	0.092	1.66	1.30	1.27	dynamic bore impact
54	0.094	0.92	1.65	0.56	quasi-static/ down-rush bore impact
55	0.096	1.41	1.64	0.86	quasi-static/ down-rush bore impact
56	0.098	1.63	1.14	1.43	dynamic bore impact
57	0.099	1.22	1.59	0.77	quasi-static/ down-rush bore impact

Appendix 14

Illumination of the flow for the high-speed camera recording

Achieving good illumination of the flow proved challenging throughout the WALOWA test programme. Figure 64 show frames captured by the high-speed camera for a single impact event. For this test illumination was provided by a top-mounted LED Lightsource. The variation in the exposure of the image occurs when the post-impact flow layer thickness at the wall becomes too high, which means less light can reach the recorded frame. An extreme case of that is visible in Figure 64 – 4.

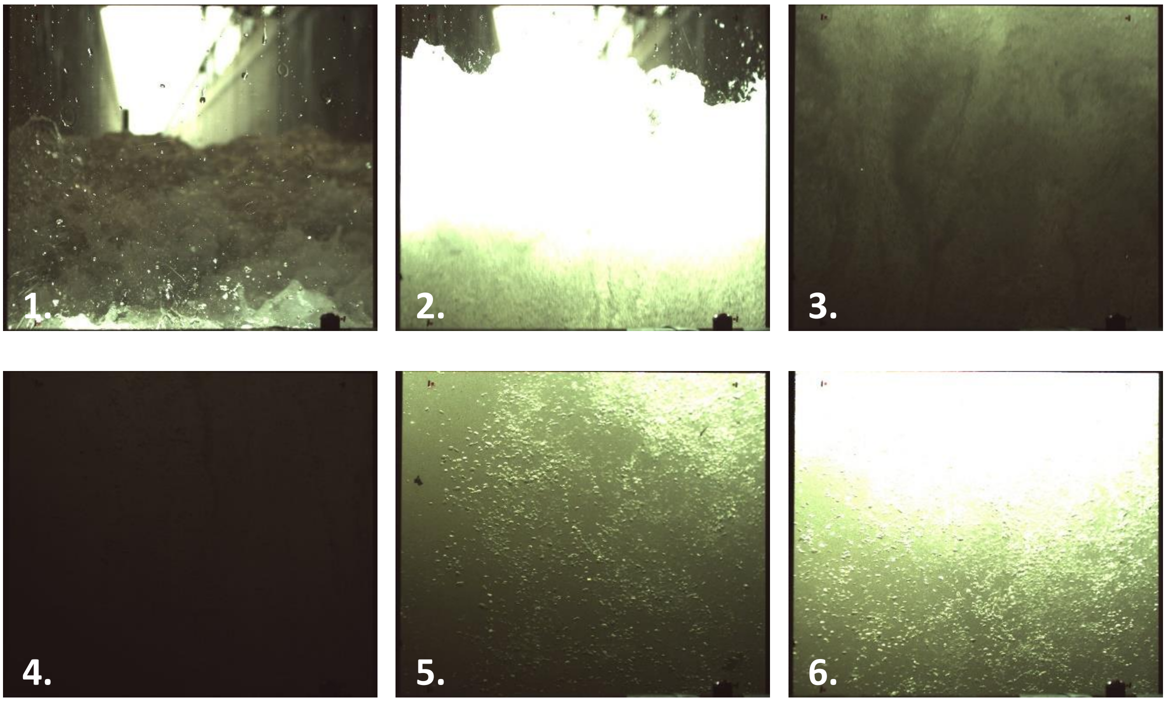

Figure 64: High-speed camera frames for a single impact illuminated from above.

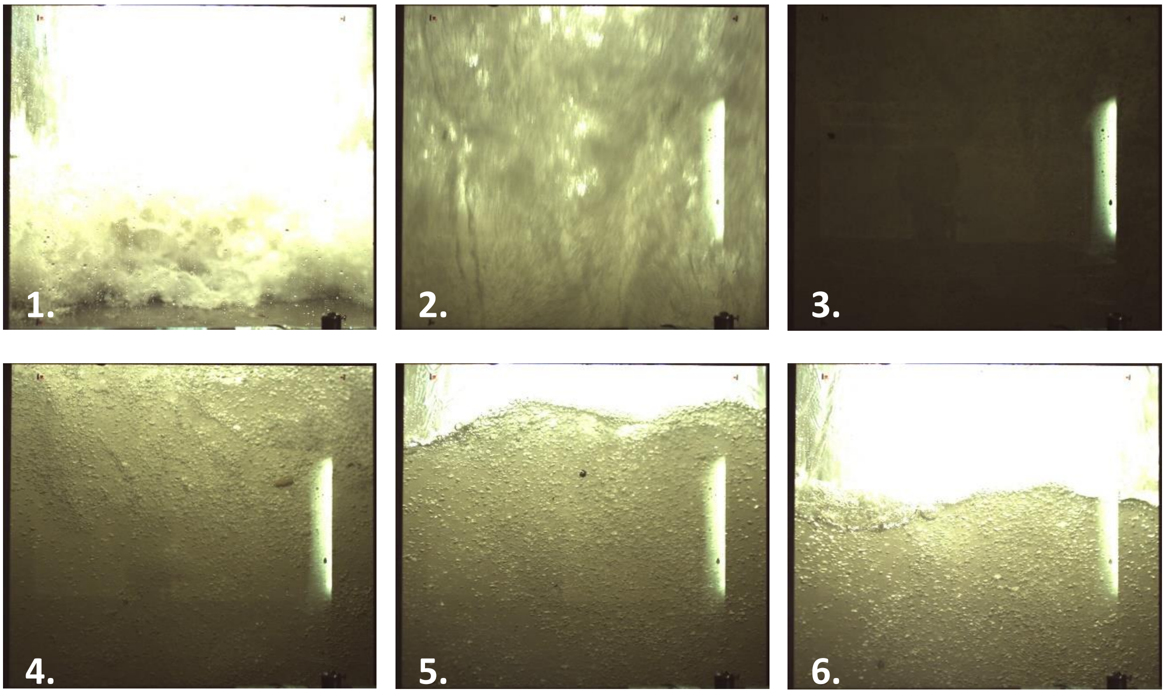

Figure 65: High-speed camera frames for a single impact illuminated from behind the window.

The illumination in Figure 65 is provided from behind by a less powerful LED light source. Note how this also does not solve the drop in exposure (Figure 65 – 3.). However, the exposure remains relatively more constant throughout the impact event. Although not tested, it is anticipated that a light source from below the window (integrated into the promenade-steel wall edge) will provide improved illumination of the flow.